

Cumulants and correlation functions of net-proton, proton, and antiproton multiplicity distributions in Au+Au collisions at energies available at the BNL Relativistic Heavy Ion Collider


M. S. Abdallah,⁵ J. Adam,⁶ L. Adamczyk,² J. R. Adams,³⁹ J. K. Adkins,³⁰ G. Agakishiev,²⁸ I. Aggarwal,⁴¹ M. M. Aggarwal,⁴¹ Z. Ahammed,⁶¹ I. Alekseev,^{3,35} D. M. Anderson,⁵⁵ A. Aparin,²⁸ E. C. Aschenauer,⁶ M. U. Ashraf,¹¹ F. G. Atetalla,²⁹ A. Attri,⁴¹ G. S. Averichev,²⁸ V. Bairathi,⁵³ W. Baker,¹⁰ J. G. Ball Cap,²⁰ K. Barish,¹⁰ A. Behera,⁵² R. Bellwied,²⁰ P. Bhagat,²⁷ A. Bhasin,²⁷ J. Bielcik,¹⁴ J. Bielcikova,³⁸ I. G. Bordyuzhin,³ J. D. Brandenburg,⁶ A. V. Brandin,³⁵ I. Bunzarov,²⁸ J. Butterworth,⁴⁵ X. Z. Cai,⁵⁰ H. Caines,⁶⁴ M. Calderón de la Barca Sánchez,⁸ D. Cebra,⁸ I. Chakaberia,^{31,6} P. Chaloupka,¹⁴ B. K. Chan,⁹ F.-H. Chang,³⁷ Z. Chang,⁶ N. Chankova-Bunzarova,²⁸ A. Chatterjee,¹¹ S. Chattopadhyay,⁶¹ D. Chen,¹⁰ J. Chen,⁴⁹ J. H. Chen,¹⁸ X. Chen,⁴⁸ Z. Chen,⁴⁹ J. Cheng,⁵⁷ M. Chevalier,¹⁰ S. Choudhury,¹⁸ W. Christie,⁶ X. Chu,⁶ H. J. Crawford,⁷ M. Csanád,¹⁶ M. Daugherty,¹ T. G. Dedovich,²⁸ I. M. Deppner,¹⁹ A. A. Derevschikov,⁴³ A. Dhamija,⁴¹ L. Di Carlo,⁶³ L. Didenko,⁶ X. Dong,³¹ J. L. Drachenberg,¹ J. C. Dunlop,⁶ N. Elsey,⁶³ J. Engelage,⁷ G. Eppley,⁴⁵ S. Esumi,⁵⁸ O. Evdokimov,¹² A. Ewigleben,³² O. Eyser,⁶ R. Fatemi,³⁰ F. M. Fawzi,⁵ S. Fazio,⁶ P. Federic,³⁸ J. Fedorisin,²⁸ C. J. Feng,³⁷ Y. Feng,⁴⁴ P. Filip,²⁸ E. Finch,⁵¹ Y. Fisyak,⁶ A. Francisco,⁶⁴ C. Fu,¹¹ L. Fulek,² C. A. Gagliardi,⁵⁵ T. Galatyuk,¹⁵ F. Geurts,⁴⁵ N. Ghimire,⁵⁴ A. Gibson,⁶⁰ K. Gopal,²³ X. Gou,⁴⁹ D. Grosnick,⁶⁰ A. Gupta,²⁷ W. Guryn,⁶ A. I. Hamad,²⁹ A. Hamed,⁵ Y. Han,⁴⁵ S. Harabasz,¹⁵ M. D. Harasty,⁸ J. W. Harris,⁶⁴ H. Harrison,³⁰ S. He,¹¹ W. He,¹⁸ X. H. He,²⁶ Y. He,⁴⁹ S. Heppelmann,⁸ S. Heppelmann,⁴² N. Herrmann,¹⁹ E. Hoffman,²⁰ L. Holub,¹⁴ Y. Hu,¹⁸ H. Huang,³⁷ H. Z. Huang,⁹ S. L. Huang,⁵² T. Huang,³⁷ X. Huang,⁵⁷ Y. Huang,⁵⁷ T. J. Humanic,³⁹ D. Isenhower,¹ W. W. Jacobs,²⁵ C. Jena,²³ A. Jentsch,⁶ Y. Ji,³¹ J. Jia,^{6,52} K. Jiang,⁴⁸ X. Ju,⁴⁸ E. G. Judd,⁷ S. Kabana,⁵³ M. L. Kabir,¹⁰ S. Kagamaster,³² D. Kalinkin,^{25,6} K. Kang,⁵⁷ D. Kapukchyan,¹⁰ K. Kauder,⁶ H. W. Ke,⁶ D. Keane,²⁹ A. Kechechyan,²⁸ Y. V. Khyzhniak,³⁵ D. P. Kikoła,⁶² C. Kim,¹⁰ B. Kimelman,⁸ D. Kincses,¹⁶ I. Kisel,¹⁷ A. Kiselev,⁶ A. G. Knosp,³² L. Kochenda,³⁵ L. K. Kosarzewski,¹⁴ L. Kramerik,¹⁴ P. Kravtsov,³⁵ L. Kumar,⁴¹ S. Kumar,²⁶ R. Kunnawalkam Elayavalli,⁶⁴ J. H. Kwasizur,²⁵ R. Lacey,⁵² S. Lan,¹¹ J. M. Landgraf,⁶ J. Lauret,⁶ A. Lebedev,⁶ R. Lednický,²⁸ J. H. Lee,⁶ Y. H. Leung,³¹ C. Li,⁴⁹ C. Li,⁴⁸ W. Li,⁴⁵ X. Li,⁴⁸ Y. Li,⁵⁷ X. Liang,¹⁰ Y. Liang,²⁹ R. Licenik,³⁸ T. Lin,⁵⁵ Y. Lin,¹¹ M. A. Lisa,³⁹ F. Liu,¹¹ H. Liu,²⁵ P. Liu,⁵² T. Liu,⁶⁴ X. Liu,³⁹ Y. Liu,⁵⁵ Z. Liu,⁴⁸ T. Ljubicic,⁶ W. J. Llope,⁶³ R. S. Longacre,⁶ E. Loyd,¹⁰ N. S. Lukow,⁵⁴ X. Luo,¹¹ L. Ma,¹⁸ R. Ma,⁶ Y. G. Ma,¹⁸ N. Magdy,¹² R. Majka,^{64,*} D. Mallick,³⁶ S. Margetis,²⁹ C. Markert,⁵⁶ H. S. Matis,³¹ J. A. Mazer,⁴⁶ N. G. Minaev,⁴³ S. Mioduszewski,⁵⁵ B. Mohanty,³⁶ M. M. Mondal,⁵² I. Mooney,⁶³ D. A. Morozov,⁴³ A. Mukherjee,¹⁶ M. Nagy,¹⁶ J. D. Nam,⁵⁴ Md. Nasim,²² K. Nayak,¹¹ D. Neff,⁹ J. M. Nelson,⁷ D. B. Nemes,⁶⁴ M. Nie,⁴⁹ G. Nigmatkulov,³⁵ T. Niida,⁵⁸ R. Nishitani,⁵⁸ L. V. Nogach,⁴³ T. Nonaka,⁵⁸ A. S. Nunes,⁶ G. Odyniec,³¹ A. Ogawa,⁶ S. Oh,³¹ V. A. Okorokov,³⁵ B. S. Page,⁶ R. Pak,⁶ A. Pandav,³⁶ A. K. Pandey,⁵⁸ Y. Panebratsev,²⁸ P. Parfenov,³⁵ B. Pawlik,⁴⁰ D. Pawlowska,⁶² H. Pei,¹¹ C. Perkins,⁷ L. Pinsky,²⁰ R. L. Pintér,¹⁶ J. Pluta,⁶² B. R. Pokhrel,⁵⁴ G. Poniatkin,³⁸ J. Porter,³¹ M. Posik,⁵⁴ V. Prozorova,¹⁴ N. K. Pruthi,⁴¹ M. Przybycien,² J. Putschke,⁶³ H. Qiu,²⁶ A. Quintero,⁵⁴ C. Racz,¹⁰ S. K. Radhakrishnan,²⁹ N. Raha,⁶³ R. L. Ray,⁵⁶ R. Reed,³² H. G. Ritter,³¹ M. Robotkova,³⁸ O. V. Rogachevskiy,²⁸ J. L. Romero,⁸ L. Ruan,⁶ J. Rusnak,³⁸ N. R. Sahoo,⁴⁹ H. Sako,⁵⁸ S. Salur,⁴⁶ J. Sandweiss,^{64,*} S. Sato,⁵⁸ W. B. Schmidke,⁶ N. Schmitz,³³ B. R. Schweid,⁵² F. Seck,¹⁵ J. Seger,¹³ M. Sergeeva,⁹ R. Seto,¹⁰ P. Seyboth,³³ N. Shah,²⁴ E. Shahaiev,²⁸ P. V. Shanmuganathan,⁶ M. Shao,⁴⁸ T. Shao,⁵⁰ A. I. Sheikh,²⁹ D. Shen,⁵⁰ S. S. Shi,¹¹ Y. Shi,⁴⁹ Q. Y. Shou,¹⁸ E. P. Sichtermann,³¹ R. Sikora,² M. Simko,³⁸ J. Singh,⁴¹ S. Singha,²⁶ M. J. Skoby,⁴⁴ N. Smirnov,⁶⁴ Y. Söhngen,¹⁹ W. Solyst,²⁵ P. Sorensen,⁶ H. M. Spinka,^{4,*} B. Srivastava,⁴⁴ T. D. S. Stanislaus,⁶⁰ M. Stefaniak,⁶² D. J. Stewart,⁶⁴ M. Strikhanov,³⁵ B. Stringfellow,⁴⁴ A. A. P. Suaide,⁴⁷ M. Sumner,³⁸ B. Summa,⁴² X. M. Sun,¹¹ X. Sun,¹² Y. Sun,⁴⁸ Y. Sun,²¹ B. Surrow,⁵⁴ D. N. Svirida,³ Z. W. Sweger,⁸ P. Szymanski,⁶² A. H. Tang,⁶ Z. Tang,⁴⁸ A. Taranenko,³⁵ T. Tarnowsky,³⁴ J. H. Thomas,³¹ A. R. Timmins,²⁰ D. Tlusty,¹³ T. Todoroki,⁵⁸ M. Tokarev,²⁸ C. A. Tomkiel,³² S. Trentalange,⁹ R. E. Tribble,⁵⁵ P. Tribedy,⁶ S. K. Tripathy,¹⁶ T. Truhlar,¹⁴ B. A. Trzeciak,¹⁴ O. D. Tsai,⁹ Z. Tu,⁶ T. Ullrich,⁶ D. G. Underwood,⁴ I. Upsal,^{49,6} G. Van Buren,⁶ J. Vanek,³⁸ A. N. Vasiliev,⁴³ I. Vassiliev,¹⁷ V. Verkest,⁶³ F. Videbæk,⁶ S. Vokal,²⁸ S. A. Voloshin,⁶³ F. Wang,⁴⁴ G. Wang,⁹ J. S. Wang,²¹ P. Wang,⁴⁸ Y. Wang,¹¹ Y. Wang,⁵⁷ Z. Wang,⁴⁹ J. C. Webb,⁶ P. C. Weidenkaff,¹⁹ L. Wen,⁹ G. D. Westfall,³⁴ H. Wieman,³¹ S. W. Wissink,²⁵ R. Witt,⁵⁹ J. Wu,²⁶ Y. Wu,¹⁰ B. Xi,⁵⁰ Z. G. Xiao,⁵⁷ G. Xie,³¹ W. Xie,⁴⁴ H. Xu,²¹ N. Xu,³¹ Q. H. Xu,⁴⁹ Y. Xu,⁴⁹ Z. Xu,⁶ Z. Xu,⁹ C. Yang,⁴⁹ Q. Yang,⁴⁹ S. Yang,⁴⁵ Y. Yang,³⁷ Z. Yang,¹¹ Z. Ye,⁴⁵ Z. Ye,¹² L. Yi,⁴⁹ K. Yip,⁶ Y. Yu,⁴⁹ H. Zbroszczyk,⁶² W. Zha,⁴⁸ C. Zhang,⁵² D. Zhang,¹¹ S. Zhang,¹² S. Zhang,¹⁸ X. P. Zhang,⁵⁷ Y. Zhang,²⁶ Y. Zhang,⁴⁸ Y. Zhang,¹¹ Z. J. Zhang,³⁷ Z. Zhang,⁶ Z. Zhang,¹² J. Zhao,⁴⁴ C. Zhou,¹⁸ X. Zhu,⁵⁷ Z. Zhu,⁴⁹ M. Zurek,³¹ and M. Zyzak¹⁷

(STAR Collaboration)

¹Abilene Christian University, Abilene, Texas 79699²AGH University of Science and Technology, FPACS, Cracow 30-059, Poland³Alikhanov Institute for Theoretical and Experimental Physics NRC “Kurchatov Institute”, Moscow 117218, Russia⁴Argonne National Laboratory, Argonne, Illinois 60439⁵American University of Cairo, New Cairo 11835, New Cairo, Egypt

*Deceased.

- ⁶Brookhaven National Laboratory, Upton, New York 11973
⁷University of California, Berkeley, California 94720
⁸University of California, Davis, California 95616
⁹University of California, Los Angeles, California 90095
¹⁰University of California, Riverside, California 92521
¹¹Central China Normal University, Wuhan, Hubei 430079
¹²University of Illinois at Chicago, Chicago, Illinois 60607
¹³Creighton University, Omaha, Nebraska 68178
¹⁴Czech Technical University in Prague, FNSPE, Prague 115 19, Czech Republic
¹⁵Technische Universität Darmstadt, Darmstadt 64289, Germany
¹⁶ELTE Eötvös Loránd University, Budapest, H-1117, Hungary
¹⁷Frankfurt Institute for Advanced Studies FIAS, Frankfurt 60438, Germany
¹⁸Fudan University, Shanghai, 200433
¹⁹University of Heidelberg, Heidelberg 69120, Germany
²⁰University of Houston, Houston, Texas 77204
²¹Huzhou University, Huzhou, Zhejiang 313000
²²Indian Institute of Science Education and Research (IISER), Berhampur 760010, India
²³Indian Institute of Science Education and Research (IISER) Tirupati, Tirupati 517507, India
²⁴Indian Institute Technology, Patna, Bihar 801106, India
²⁵Indiana University, Bloomington, Indiana 47408
²⁶Institute of Modern Physics, Chinese Academy of Sciences, Lanzhou, Gansu 730000
²⁷University of Jammu, Jammu 180001, India
²⁸Joint Institute for Nuclear Research, Dubna 141 980, Russia
²⁹Kent State University, Kent, Ohio 44242
³⁰University of Kentucky, Lexington, Kentucky 40506-0055
³¹Lawrence Berkeley National Laboratory, Berkeley, California 94720
³²Lehigh University, Bethlehem, Pennsylvania 18015
³³Max-Planck-Institut für Physik, Munich 80805, Germany
³⁴Michigan State University, East Lansing, Michigan 48824
³⁵National Research Nuclear University MEPhI, Moscow 115409, Russia
³⁶National Institute of Science Education and Research, HBNI, Jatni 752050, India
³⁷National Cheng Kung University, Tainan 70101
³⁸Nuclear Physics Institute of the CAS, Rez 250 68, Czech Republic
³⁹Ohio State University, Columbus, Ohio 43210
⁴⁰Institute of Nuclear Physics PAN, Cracow 31-342, Poland
⁴¹Panjab University, Chandigarh 160014, India
⁴²Pennsylvania State University, University Park, Pennsylvania 16802
⁴³NRC “Kurchatov Institute”, Institute of High Energy Physics, Protvino 142281, Russia
⁴⁴Purdue University, West Lafayette, Indiana 47907
⁴⁵Rice University, Houston, Texas 77251
⁴⁶Rutgers University, Piscataway, New Jersey 08854
⁴⁷Universidade de São Paulo, São Paulo 05314-970, Brazil
⁴⁸University of Science and Technology of China, Hefei, Anhui 230026
⁴⁹Shandong University, Qingdao, Shandong 266237
⁵⁰Shanghai Institute of Applied Physics, Chinese Academy of Sciences, Shanghai 201800
⁵¹Southern Connecticut State University, New Haven, Connecticut 06515
⁵²State University of New York, Stony Brook, New York 11794
⁵³Instituto de Alta Investigación, Universidad de Tarapacá, Arica 1000000, Chile
⁵⁴Temple University, Philadelphia, Pennsylvania 19122
⁵⁵Texas A&M University, College Station, Texas 77843
⁵⁶University of Texas, Austin, Texas 78712
⁵⁷Tsinghua University, Beijing 100084
⁵⁸University of Tsukuba, Tsukuba, Ibaraki 305-8571, Japan
⁵⁹United States Naval Academy, Annapolis, Maryland 21402
⁶⁰Valparaiso University, Valparaiso, Indiana 46383
⁶¹Variable Energy Cyclotron Centre, Kolkata 700064, India
⁶²Warsaw University of Technology, Warsaw 00-661, Poland
⁶³Wayne State University, Detroit, Michigan 48201
⁶⁴Yale University, New Haven, Connecticut 06520

 (Received 31 January 2021; accepted 12 July 2021; published 5 August 2021)

We report a systematic measurement of cumulants, C_n , for net-proton, proton, and antiproton multiplicity distributions, and correlation functions, κ_n , for proton and antiproton multiplicity distributions up to the fourth order in Au+Au collisions at $\sqrt{s_{NN}} = 7.7, 11.5, 14.5, 19.6, 27, 39, 54.4, 62.4,$ and 200 GeV. The C_n and κ_n are presented as a function of collision energy, centrality and kinematic acceptance in rapidity, y , and transverse momentum, p_T . The data were taken during the first phase of the Beam Energy Scan (BES) program (2010–2017) at the BNL Relativistic Heavy Ion Collider (RHIC) facility. The measurements are carried out at midrapidity ($|y| < 0.5$) and transverse momentum $0.4 < p_T < 2.0$ GeV/ c , using the STAR detector at RHIC. We observe a nonmonotonic energy dependence ($\sqrt{s_{NN}} = 7.7$ –62.4 GeV) of the net-proton C_4/C_2 with the significance of 3.1σ for the 0–5% central Au+Au collisions. This is consistent with the expectations of critical fluctuations in a QCD-inspired model. Thermal and transport model calculations show a monotonic variation with $\sqrt{s_{NN}}$. For the multiparticle correlation functions, we observe significant negative values for a two-particle correlation function, κ_2 , of protons and antiprotons, which are mainly due to the effects of baryon number conservation. Furthermore, it is found that the four-particle correlation function, κ_4 , of protons plays a role in determining the energy dependence of proton C_4/C_1 below 19.6 GeV, which cannot be understood by the effect of baryon number conservation.

DOI: [10.1103/PhysRevC.104.024902](https://doi.org/10.1103/PhysRevC.104.024902)

I. INTRODUCTION

The main goal of the Beam Energy Scan (BES) program at the BNL Relativistic Heavy Ion Collider (RHIC) is to study the QCD phase structure [1,2]. This is expected to lead to the mapping of the phase diagram for strong interactions in the space of temperature (T) versus baryon chemical potential (μ_B). Both theoretically and experimentally, several advancements have been made towards this goal. Lattice QCD calculations have established that at high temperatures there occurs a crossover transition from hadronic matter to a deconfined state of quarks and gluons at $\mu_B = 0$ MeV [3]. Experimental data from RHIC and the Large Hadron Collider (LHC) have provided evidence of this matter with quark and gluon degrees of freedom called the quark-gluon plasma (QGP) [4–7]. The QGP has been found to hadronize into a gas of hadrons, which undergoes chemical freeze-out (inelastic collisions cease) [8] at a temperature close to the lattice QCD-estimated quark-hadron transition temperature at $\mu_B = 0$ MeV [9,10]. A suite of interesting results from the BES program indicate a change of equation of state of QCD matter, with collision energy from partonic-interaction-dominated matter at higher collision energies to a hadronic-interaction regime at lower energies. These include the observations of breakdown in the number of constituent-quark scaling of the elliptic flow at lower $\sqrt{s_{NN}}$ [11], nonmonotonic variation of the slope of the directed flow for protons and net protons at midrapidity as a function of $\sqrt{s_{NN}}$ [12], nuclear modification factor changing values from smaller than unity to larger than unity at high p_T as we go to lower $\sqrt{s_{NN}}$ [13], and finite to vanishing values of the three-particle correlations with respect to the event plane [14] as we go to lower $\sqrt{s_{NN}}$.

The QCD phase structure at finite temperature and baryon chemical potential has been extensively studied by various QCD-based model calculations, such as the Dyson-Schwinger equation (DSE) method [15–19], functional renormalization group (FRG) [20], Nambu-Jona-Lasinio (NJL) [21], Polyakov Nambu-Jona-Lasinio (PNJL) [22–24], and other effective

models [25,26]. One of the most important studies of the QCD phase structure relates to the first-order phase boundary and the expected existence of the critical point (CP) [27–32]. This is the end point of a first-order phase boundary between quark-gluon and hadronic phases [33,34]. Experimental confirmation of the CP would be a landmark of exploring the QCD phase structure. Previous studies of higher-order cumulants of net-proton multiplicity distributions suggest that the possible CP region is unlikely to be below $\mu_B = 200$ MeV [35], which is consistent with the theoretical findings [19,20,29,31,36]. The versatility of the RHIC machine has permitted the colliding energies of ions to be varied below the injection energy of $\sqrt{s_{NN}} = 19.6$ GeV [37], and thereby the RHIC BES program provides the possibility to scan the QCD phase diagram up to $\mu_B = 420$ MeV with the collider mode, and $\mu_B = 720$ MeV with the fixed-target mode [2,38]. This, in turn, opens the possibility to find the experimental signatures of a first-order phase transition and the CP [39,40].

Higher-order cumulants of the distributions of conserved charge, such as net-baryon (B), net-charge (Q), and net-strangeness (S) numbers, are sensitive to the QCD phase transition and CP [41–51]. The signatures of conserved-charge fluctuations near CP have been studied by various model calculations [46,47,52–65]. However, these model calculations are based on the assumption of thermal equilibrium with a static and infinite medium. In heavy-ion collisions, finite-size and time effects will put constraints on the significance of the signals [66,67]. A theoretical calculation suggests the nonequilibrium correlation length $\xi \approx 2$ –3 fm for heavy-ion collisions [68]. Dynamical modeling of heavy-ion collisions with the physics of a critical point and nonequilibrium effects is in progress [69–73]. The signatures of a phase transition or a CP are detectable if they survive the evolution of the system [74]. Due to a stronger dependence on the correlation length (ξ) [46–48], it is proposed to study the higher moments, skewness [$S = \langle(\delta N)^3\rangle/\sigma^3$] and kurtosis [$\kappa = \langle(\delta N)^4\rangle/\sigma^4 - 3$] with $\delta N = N - \langle N \rangle$, or cumulants C_n

(defined in Sec. II E) of distributions of conserved quantities. Both the magnitude and the sign of the moments or C_n [47,75], which quantify the shape of the multiplicity distributions, are important for understanding the phase transition and CP effects. The aim is to search for signatures of the CP over a broad range of μ_B in the QCD phase diagram [35].

Furthermore, the products of the moments or ratios of C_n can be related to susceptibilities associated with the conserved numbers. The product ($\kappa\sigma^2$) or, equivalently, the ratio (C_4/C_2) of the net-baryon number distribution is related to the ratio of fourth-order (χ_4^B) to second-order (χ_2^B) baryon number susceptibilities [44,50,76–78]. The ratio χ_4^B/χ_2^B is expected to deviate from unity near the CP. It has different values for the hadronic and partonic phases [78]. Similarly, the products $S\sigma$ (C_3/C_2) and $\sigma^2/\langle N \rangle$ (C_2/C_1) are related to χ_3^B/χ_2^B and χ_2^B/χ_1^B , respectively. Experimentally, it is not possible to measure the net-baryon distributions; however, theoretical calculations have shown that net-proton multiplicity ($N_p - N_{\bar{p}} = \Delta N_p$) fluctuations reflect the singularity of the charge and baryon number susceptibility, as expected at the CP [43]. References [79,80] discuss the effect of using net protons as the approximation for the net-baryon distributions and the acceptance dependence for the moments of the protons and antiprotons.

In an early publication from the STAR experiment on the higher moments of net-proton distributions, the selected kinematics of the (anti)proton are $|y| < 0.5$ and $0.4 < p_T < 0.8$ GeV/ c , where only the Time Projection Chamber (TPC) [81,82] was used for (anti)proton identification. Interesting hints of a nonmonotonic variation of $\kappa\sigma^2$ (or C_4/C_2) was observed [83]. In this paper, we report measurements of the energy dependence of C_n up to fourth order of the net-proton multiplicity distributions from Au+Au collisions with a larger acceptance of $0.4 < p_T < 2.0$ GeV/ c [84]. This is achieved by adding the information from STAR's Time-of-Flight (TOF) detector [85]. We present results from Au+Au collisions at nine different collision energies: $\sqrt{s_{NN}} = 7.7, 11.5, 14.5, 19.6, 27, 39, 54.4, 62.4,$ and 200 GeV.

The paper is organized as follows. In the next section, we discuss the data sets used, event selection criteria, centrality selection procedure, proton identification method, measurement of raw cumulants of the net-proton distributions, corrections for the effects of centrality bin width (CBW) and efficiency, and estimation of statistical and systematic uncertainties on the measurements. In Sec. III, we present the results of cumulants and their ratios for net protons, protons, and antiprotons in Au+Au collisions as a function of collision energy ($\sqrt{s_{NN}}$), centrality, transverse momentum (p_T) acceptance, and rapidity acceptance (Δy). In addition, we present the extracted various order integrated correlation functions of protons and antiprotons from the measured cumulants. In this section, we also discuss the results from the HRG model and transport model calculations. In Sec. IV, we present the summary. Detailed discussions on the efficiency correction, and the estimation of the statistical uncertainties are presented in Appendices A and B, respectively.

TABLE I. Total number of events for Au+Au collisions analysed for various collision energies ($\sqrt{s_{NN}}$) obtained after all of the event selection criteria are applied. The Z-vertex (V_z) range, the chemical freeze-out temperature (T_{ch}), and baryon chemical potential (μ_B) for 0–5% Au+Au collisions [8] are also given.

$\sqrt{s_{NN}}$ (GeV)	No. of events ($\times 10^6$)	$ V_z $ (cm)	T_{ch} (MeV)	μ_B (MeV)
200	238	30	164.3	28
62.4	47	30	160.3	70
54.4	550	30	160.0	83
39	86	30	156.4	103
27	30	30	155.0	144
19.6	15	30	153.9	188
14.5	20	30	151.6	264
11.5	6.6	30	149.4	287
7.7	3	40	144.3	398

II. EXPERIMENTAL DATA ANALYSIS

A. Data set and event selection

The data presented in the paper were obtained using the Time Projection Chamber (TPC) [81] and the Time-of-Flight detectors (TOF) [85] of the Solenoidal Tracker at RHIC (STAR) [81]. The event-by-event proton (N_p) and antiproton ($N_{\bar{p}}$) multiplicities are measured for Au+Au minimum-bias events at $\sqrt{s_{NN}} = 7.7, 11.5, 14.5, 19.6, 27, 39, 54.4, 62.4,$ and 200 GeV for collisions occurring within a certain Z-position (V_z) range of the collision vertex (given in Table I) from the TPC center along the beam line. These data sets were taken with a minimum-bias trigger, which was defined using a coincidence of hits in the zero degree calorimeters (ZDCs) [86], vertex position detectors (VPDs) [87], and/or beam-beam counters (BBCs) [88]. The range of $|V_z|$ is chosen to optimize the event statistics and uniformity of the response of the detectors used in the analysis.

In order to reject background events which involve interactions with the beam pipe, the transverse radius of the event vertex is required to be within 2 cm (1 cm for 14.5 GeV) of the center of STAR [8]. We use two methods to determine the V_z : one from a fast scintillator-based vertex position detector, and the other from the most probable point of common origin of the tracks, which are reconstructed from the hits measured in the TPC. To remove pile-up events at energies above 27 GeV, we require the V_z difference between the two methods to be within 3 cm. Further, a detailed study of the TPC tracks as a function of the TOF matched tracks with valid TOF information is carried out and outlier events are rejected. To ensure the quality of the data, a run-by-run study of several variables—such as the total number of uncorrected charged particles measured in the TPC, average transverse momentum ($\langle p_T \rangle$), mean pseudorapidity (η), and azimuthal angle (ϕ) in an event—is carried out. Outlier runs beyond $\pm 3\sigma$, where σ corresponds to the standard deviation of run-by-run distributions of a variable, are not included in the current analysis. In addition, the distance of closest approach (DCA) of the charged-particle track from the primary vertex, and especially the signed transverse DCA (DCA_{xy}), are studied to remove

TABLE II. Proton and antiproton track selection criteria at all energies. The N_{Fit} and N_{HitPoss} represent the number of hits used in track fitting and the maximum number of possible hits in the TPC.

$ y $	p_T (GeV/c)	DCA (cm)	N_{Fit}	$N_{\text{Fit}}/$ N_{HitPoss}	No. of dE/dx points
< 0.5	0.4–2.0	< 1	> 20	> 0.52	> 5

bad events (The signed transverse DCA refers to the DCA with respect to the primary vertex in the transverse plane. Its sign is the sign of the vector product of the DCA vector and the track momentum). These classes of bad events are primarily related to unstable beam conditions during the data taking and inaccurate space-charge calibration of the TPC.

Table I gives the total number of minimum-bias events analyzed for each $\sqrt{s_{NN}}$ and the corresponding chemical freeze-out temperature (T_{ch}) and baryon chemical potential (μ_B) values for central 0–5% Au+Au collisions. The beam energy values in the BES program are chosen so that the difference in μ_B values is not larger than 100 MeV between adjacent collision energies.

B. Track selection, particle identification, and acceptance

The proton and antiproton track selection criteria for all the $\sqrt{s_{NN}}$ are presented in Table II. In order to suppress contamination by tracks from secondary vertices, a requirement of less than 1 cm is placed on DCA between each track and the event vertex. Tracks are required to have at least 20 points used in track fitting out of a maximum of 45 possible hits in the TPC. To prevent multiple counting of split tracks, more than 52% of the maximum-possible fit points are required. A condition is also placed on the number of points (> 5) used to extract the energy loss (dE/dx) values, which is used to identify the (anti)protons from the charged particles detected in the TPC. The results presented here are within kinematics $|y| < 0.5$ and $0.4 < p_T < 2.0$ GeV/c.

Particle identification (PID) is carried out using the TPC and TOF by measuring the dE/dx and time of flight, respectively. Figure 1 (left top panel) shows a typical plot of the square of the mass (m^2) associated with a track measured in the TPC as a function of rigidity (defined as momentum/ z , where z is the dimensionless ratio of particle charge to the electron charge magnitude) for Au+Au collisions at $\sqrt{s_{NN}} =$

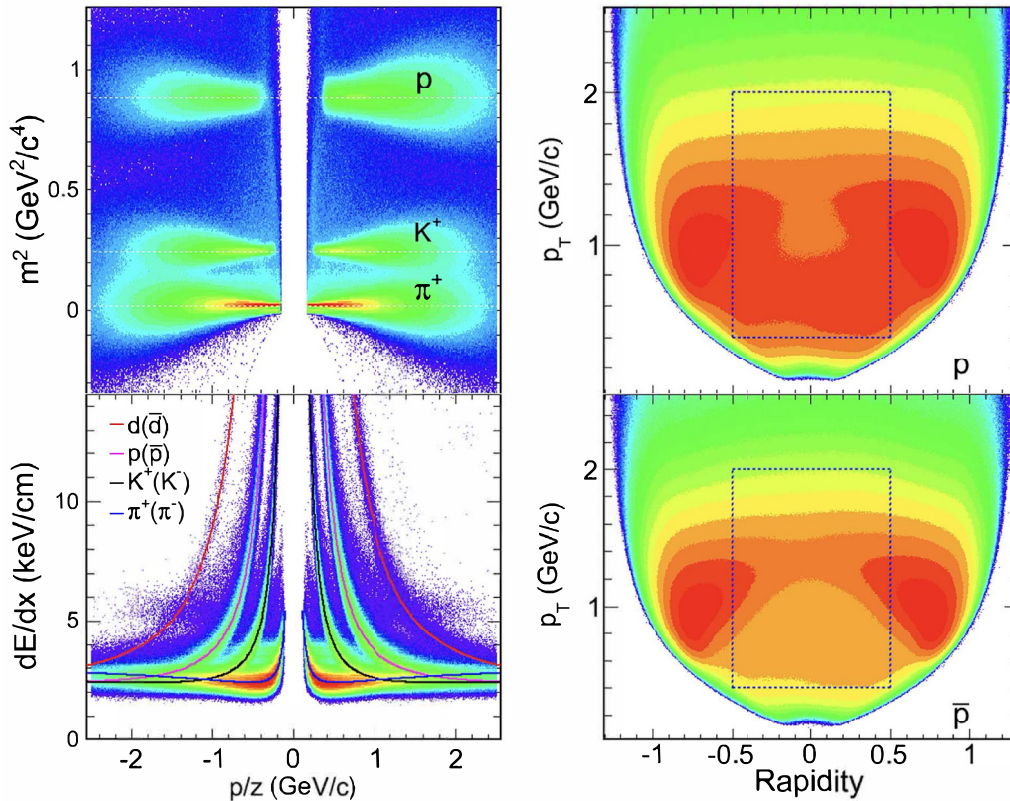


FIG. 1. Top left panel: The mass squared (m^2) versus rigidity for charged tracks in Au+Au collisions at $\sqrt{s_{NN}} = 39$ GeV. The rigidity is defined as momentum/ z , where z is the dimensionless ratio of particle charge to the electron charge magnitude. Bottom left panel: The specific ionization energy loss (dE/dx) as a function of rigidity measured in the TPC for the same data set. Also shown as solid lines are the theoretical expectations for each particle species. Right panels: Rapidity (y) versus transverse momentum (p_T). The color reflects the relative yields of protons (top) and antiprotons (bottom) using the TPC PID for Au+Au collisions at $\sqrt{s_{NN}} = 39$ GeV. The dashed boxes represent the acceptance used in the current analysis. Two blobs at large rapidities are contaminated by particles other than (anti)protons. This contamination is rejected in later steps of the analysis.

39 GeV. The m^2 is given by

$$m^2 = p^2 \left(\frac{c^2 t^2}{L^2} - 1 \right), \quad (1)$$

where p , t , L , and c are the momentum, time-of-flight of the particle, path length, and speed of light, respectively. Protons and antiprotons can be identified by selecting charged tracks for which $0.6 < m^2 < 1.2 \text{ GeV}^2/c^4$.

Figure 1 (left bottom panel) shows the dE/dx of measured charged particles plotted as a function of the rigidity. The measured values of dE/dx are compared to the expected theoretical values [90] (shown as solid lines in Fig. 1) to select the proton and antiproton tracks. A quantity called $N_{\sigma,p}$ for charged tracks in the TPC is defined as

$$N_{\sigma,p} = (1/\sigma_R) \ln \left(\frac{\langle dE/dx \rangle}{\langle dE/dx \rangle_p^{\text{th}}} \right), \quad (2)$$

where $\langle dE/dx \rangle$ is the truncated mean value of the track energy loss measured in the TPC, $\langle dE/dx \rangle_p^{\text{th}}$ is the corresponding theoretical value for a proton (or antiproton) in the STAR TPC [90], and σ_R is the dE/dx resolution which is momentum-dependent and of the order of 7.5% for the momentum range of this analysis. Assuming that the $N_{\sigma,p}$ distribution in a given momentum range is Gaussian, it should peak at zero for proton tracks and the values represent the deviation from the theoretical values for proton tracks in terms of standard deviations (σ_R). Momentum-dependent selection criteria are used for TPC tracks to select protons or antiprotons. For $0.4 < p_T < 0.8 \text{ GeV}/c$ and momentum (p) less than $1 \text{ GeV}/c$, $|N_{\sigma,p}| < 2.0$ is chosen and for $0.8 < p_T < 2.0 \text{ GeV}/c$ and momentum (p) less than $3 \text{ GeV}/c$, in addition to $|N_{\sigma,p}| < 2.0$, the track is required to have $0.6 < m^2 < 1.2 \text{ GeV}^2/c^4$ from TOF. The purity is estimated by referring to the $N_{\sigma,p}$ distributions from the TPC in various p_T ranges (within 0.4 to $0.8 \text{ GeV}/c$) to estimate the contamination from other hadrons within the PID selection criteria. For the higher p_T range, the m^2 distributions from the TOF are studied after applying the $N_{\sigma,p}$ criteria and the contamination from other hadrons within the PID selection criteria is estimated. The purities of the proton and antiproton samples are better than 97% for all the p_T ranges and $\sqrt{s_{NN}}$ studied.

Figure 1 (right panels) shows p_T versus y for protons and antiprotons selected by the TPC with $|N_{\sigma,p}| < 2.0$ in Au+Au collisions at $\sqrt{s_{NN}} = 39 \text{ GeV}$. The acceptance is uniform in y - p_T and is the same for other $\sqrt{s_{NN}}$ studied here. This is a major advantage of collider-based experiments over fixed-target experiments. The boxes show the acceptance criteria used in this analysis. The addition of the TOF extends the PID capabilities to higher p_T , thereby allowing for the detection of $\sim 80\%$ of the total protons per unit rapidity (or antiprotons per unit rapidity) produced in the collisions at midrapidity. This is a significant improvement compared to the previous analysis reported in Ref. [83]. The uniform and large acceptance at midrapidity in y , p_T , and ϕ allows STAR to measure and compare the cumulants in Au+Au collisions at $\sqrt{s_{NN}} = 7.7$ to 200 GeV .

C. Centrality selection

Centrality selection plays a crucial role in the fluctuation analysis. There are two effects related to the centrality selection which need to be addressed. These are (a) the self-correlation [91,92] and (b) centrality resolution/fluctuation effects [91–95].

One of the main self-correlation effects arises when particles used for the fluctuation analysis are also used for the centrality definition. This can be significantly reduced by removing the particles used in the fluctuation analysis from the centrality definition. Hence, we exclude protons and antiprotons from charged particles for the centrality selection.

The centrality resolution effect arises due to the fact that the number of participant nucleons and particle multiplicities fluctuate even if the impact parameter is fixed. Through a model simulation it has been shown that the larger the η acceptance used for centrality selection, the closer are the values of the cumulants to the actual values [91]. This is because the centrality resolution is improved by increasing the number of particles for the centrality definition with wider acceptance. Therefore, to suppress the effect of centrality resolution, one should use the maximum available acceptance of charged particles for centrality selection. In addition, it may be mentioned that the choice of centrality definition also affects the way volume fluctuations (discussed later) contribute to the measurements.

These are the driving considerations for the centrality selection for net-proton studies presented in this paper, and they are discussed below. The basic strategy is to maximize the acceptance window for the centrality determination as allowed by the detectors, and to not use protons and antiprotons for the centrality selection. In addition, the centrality definition method given below is determined after several optimization studies using data and models. These studies were carried out by varying the acceptances in η and charged particle types in order to understand the effect of the choice of centrality determination method on the analysis [92]. The effect of self-correlation potentially arising due to the decay of heavier hadrons into protons and antiprotons and other charged particles has been verified to be negligible from a study using standard heavy-ion collision event generators, HIJING [96] and UrQMD [92,97].

In order to suppress the self-correlation, centrality resolution and volume fluctuation effects with the available STAR detectors, a new centrality measure is defined, and is different from other analyses reported by STAR [8]. The centrality is determined from the uncorrected charged particle multiplicity within pseudorapidity $|\eta| < 1$ (N_{ch}) after excluding the protons and antiprotons. Strict particle identification criteria are used to remove the proton and antiproton contributions. Charged tracks with $N_{\sigma,p} < -3$ are used and for those tracks which have TOF information an additional criterion, $m^2 < 0.4 \text{ GeV}^2/c^4$, is applied. The resultant distribution of charged particles is corrected for luminosity and V_z dependence at each $\sqrt{s_{NN}}$. The corrected charged particle distribution is then fit to a Monte Carlo Glauber model [37,89] to define the centrality classes in the experiment (the percentage cross section and the associated cuts on the charged-particle multiplicity). In the

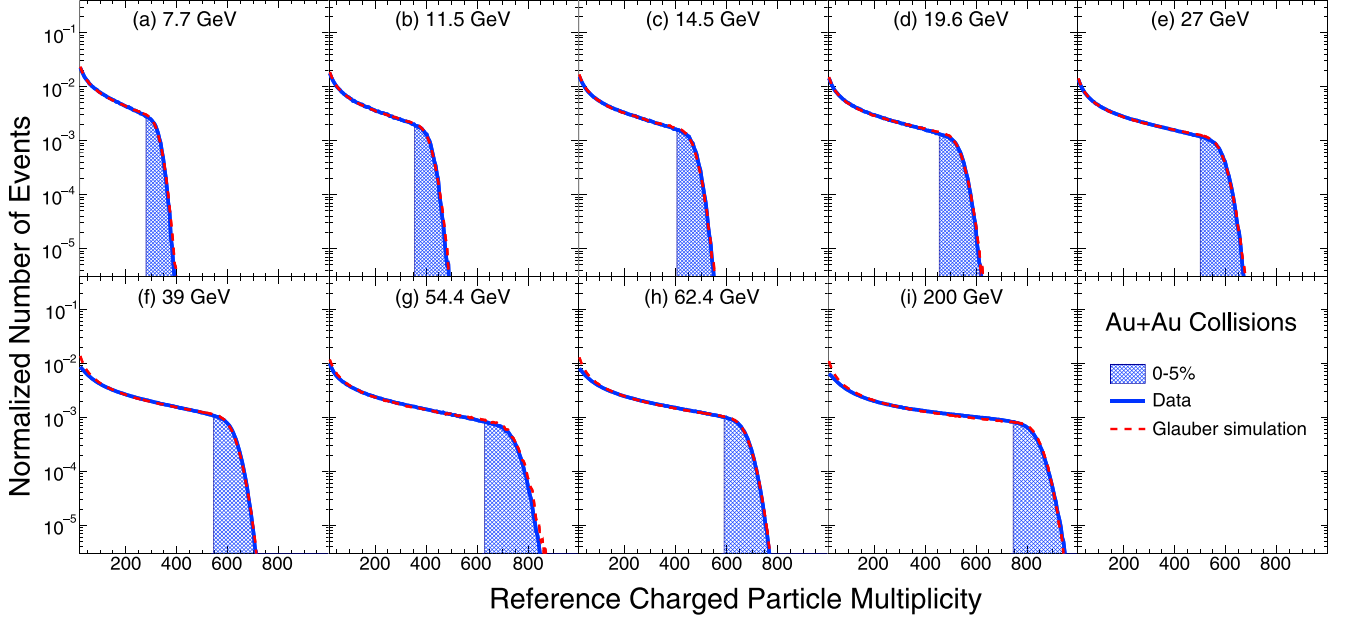


FIG. 2. The uncorrected reference charged particle multiplicity (N_{ch}) distributions within pseudorapidity $|\eta| < 1$ by excluding protons and antiprotons in Au+Au collisions at $\sqrt{s_{NN}} = 7.7\text{--}200$ GeV. These distributions are used for centrality determination. The shaded region at each $\sqrt{s_{NN}}$ corresponds to 0–5% central collisions. The dashed line corresponds to Monte Carlo Glauber model simulations [89].

fitting process, a multiplicity-dependent efficiency has been applied [37].

Figure 2 shows the reference charged particle multiplicity distributions after excluding protons and antiprotons used for centrality determination for all of the $\sqrt{s_{NN}}$ studied here. The lower boundaries of each centrality class based on N_{ch} are given in Table III. Table IV gives the average number of participant nucleons ($\langle N_{\text{part}} \rangle$) for various collision centralities for $\sqrt{s_{NN}} = 7.7\text{--}200$ GeV obtained from a Monte Carlo Glauber model simulation.

D. Uncorrected net-proton multiplicity distributions

Figure 3 shows the event-by-event net-proton multiplicity (ΔN_p) distributions from Au+Au collisions at $\sqrt{s_{NN}} =$

TABLE III. The uncorrected number of charged particles other than protons and antiprotons (N_{ch}) within the pseudorapidity $|\eta| < 1.0$ used for the centrality selection for various collision centralities expressed in % centrality in Au+Au collisions at $\sqrt{s_{NN}} = 7.7\text{--}200$ GeV.

Centrality (%)	N_{ch} values at different $\sqrt{s_{NN}}$ (GeV)								
	200	62.4	54.4	39	27	19.6	14.5	11.5	7.7
0–5	725	571	621	522	490	448	393	343	270
5–10	618	482	516	439	412	376	330	287	225
10–20	440	338	354	308	289	263	231	199	155
20–30	301	230	237	209	196	178	157	134	105
30–40	196	149	151	136	127	116	103	87	68
40–50	120	91	90	83	78	71	63	53	41
50–60	67	51	50	47	44	40	36	30	23
60–70	34	26	24	24	22	20	19	15	11
70–80	16	12	10	11	10	9	13	7	5

7.7–200 GeV for 0–5%, 30–40%, and 70–80% collision centralities. The ΔN_p distribution is obtained by counting the number of protons and antiprotons within the $y\text{-}p_T$ acceptance on an event-by-event basis for a given collision centrality and $\sqrt{s_{NN}}$. The distributions presented in Fig. 3 are not corrected for the efficiency and acceptance effects. In general, the shape of the ΔN_p distributions is broader, more symmetric and closer to Gaussian for central collisions than that for peripheral collisions. The shape of the distributions also changes with $\sqrt{s_{NN}}$. Cumulants (C_n) up to the fourth order are obtained from these distributions for each collision centrality and $\sqrt{s_{NN}}$.

E. Definition of cumulants and integrated correlation functions

In this subsection, we give the definition of the cumulants used in this paper. Let N represent any entry in the data sample, its deviation from its mean value ($\langle N \rangle$, referred to as the first moment) is then given by $\delta N = N - \langle N \rangle$. Any r th-order central moment is defined as

$$\mu_r = \langle (\delta N)^r \rangle. \quad (3)$$

The cumulants of a given data sample could be written in terms of moments as follows:

$$\begin{aligned}
 C_1 &= \langle N \rangle, \\
 C_2 &= \langle (\delta N)^2 \rangle = \mu_2, \\
 C_3 &= \langle (\delta N)^3 \rangle = \mu_3, \\
 C_4 &= \langle (\delta N)^4 \rangle - 3\langle (\delta N)^2 \rangle^2 \\
 &= \mu_4 - 3\mu_2^2, \\
 C_n(n > 3) &= \mu_n - \sum_{m=2}^{n-2} \binom{n-1}{m-1} C_m \mu_{n-m}.
 \end{aligned} \quad (4)$$

TABLE IV. The average number of participant nucleons ($\langle N_{\text{part}} \rangle$) for various collision centralities in Au+Au collisions at $\sqrt{s_{NN}} = 7.7\text{--}200$ GeV from a Monte Carlo Glauber model. The numbers in parentheses are systematic uncertainties.

Centrality (%)	$\langle N_{\text{part}} \rangle$ values at different $\sqrt{s_{NN}}$ (GeV)								
	200	62.4	54.4	39	27	19.6	14.5	11.5	7.7
0–5	351 (2)	347 (3)	346 (2)	342(2)	343 (2)	338 (2)	340(2)	338 (2)	337 (2)
5–10	299 (4)	294 (4)	292 (6)	294 (6)	299 (6)	289 (6)	289 (6)	291 (6)	290 (6)
10–20	234 (5)	230 (5)	228 (8)	230 (9)	234 (9)	225 (9)	225 (8)	226 (8)	226 (8)
20–30	168 (5)	164 (5)	161 (10)	162 (10)	166 (11)	158 (10)	159 (9)	160 (9)	160 (10)
30–40	117 (5)	114 (5)	111 (11)	111 (11)	114 (11)	108 (11)	109 (11)	110 (11)	110 (11)
40–50	78 (5)	76 (5)	73 (10)	74 (10)	75 (10)	71 (10)	72 (10)	73 (10)	72 (10)
50–60	49 (5)	48 (5)	45 (9)	46 (9)	47 (9)	44 (9)	45 (9)	45 (9)	45 (9)
60–70	29 (4)	28 (4)	26 (7)	26 (7)	27 (8)	26 (7)	26 (7)	26 (7)	26 (7)
70–80	16 (3)	15 (2)	13 (5)	14 (5)	14 (6)	14 (5)	14 (6)	14 (6)	14 (4)

The relations between cumulants and various moments are given as

$$M = C_1, \quad \sigma^2 = C_2, \quad S = \frac{C_3}{(C_2)^{3/2}}, \quad \kappa = \frac{C_4}{(C_2)^2}, \quad (5)$$

where M , σ^2 , S , and κ are mean, variance, skewness and kurtosis, respectively. The products $\kappa\sigma^2$ and $S\sigma$ can be expressed in terms of the ratio of cumulants as

$$\sigma^2/M = \frac{C_2}{C_1}, \quad S\sigma = \frac{C_3}{C_2}, \quad \kappa\sigma^2 = \frac{C_4}{C_2}. \quad (6)$$

With the above definition, we can calculate various order cumulants (moments) and cumulant ratios (moment products) from the measured event-by-event net-proton, proton, and antiproton distributions for each centrality at a given $\sqrt{s_{NN}}$. For two independent variables X and Y , the cumulants of the probability distributions of their sum ($X + Y$) are just the

addition of cumulants of the individual distributions for X and Y , i.e., $C_{n,X+Y} = C_{n,X} + C_{n,Y}$ for the n th-order cumulant. For a distribution of difference between X and Y , the cumulants are $C_{n,X-Y} = C_{n,X} + (-1)^n C_{n,Y}$, where the even-order cumulants are the addition of the individual cumulants, while the odd-order cumulants are obtained by taking their difference. If the protons and antiprotons are distributed as independent Poissonian distributions, the various order cumulants of net-proton, proton, and antiproton distributions can be expressed as

$$C_{n,p} = C_{1,p}, \quad C_{n,\bar{p}} = C_{1,\bar{p}}, \\ C_{n,p-\bar{p}} = C_{1,p} + (-1)^n C_{1,\bar{p}},$$

where the net-proton multiplicity distributions obey the Skellam distribution and the Poisson baseline/expectation values

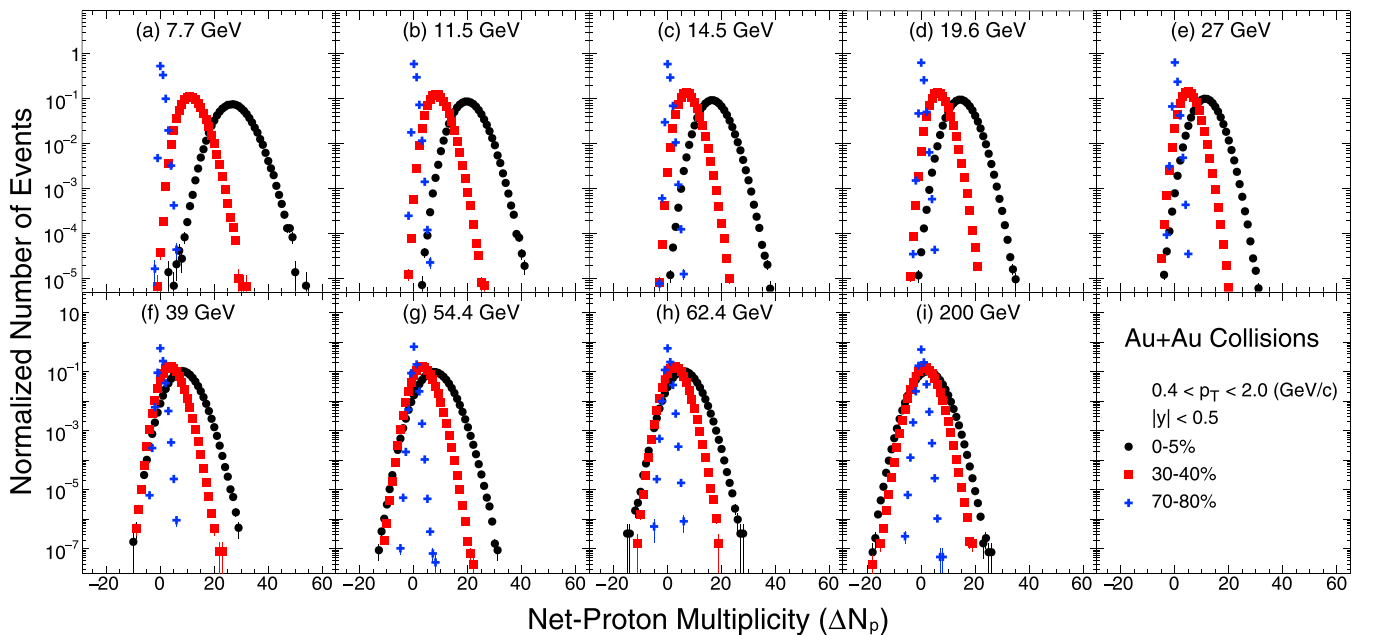


FIG. 3. Net-proton multiplicity (ΔN_p) distributions in Au+Au collisions at various $\sqrt{s_{NN}}$ for 0–5%, 30–40%, and 70–80% collision centralities at midrapidity. The statistical errors are small and within the symbol size. The distributions are not corrected for either the finite-centrality-width effect or for the reconstruction efficiencies of protons and antiprotons.

of the net-proton, proton, and antiproton cumulant ratios are

$$\begin{aligned} (\sigma^2/M)_{p,\bar{p}} &= (S\sigma)_{p,\bar{p}} = (\kappa\sigma^2)_{p,\bar{p}} = 1, \\ (\sigma^2/M)_{p-\bar{p}} &= \frac{1}{(S\sigma)_{p-\bar{p}}} = \frac{C_{1,p} + C_{1,\bar{p}}}{C_{1,p} - C_{1,\bar{p}}}, \\ (\kappa\sigma^2)_{p-\bar{p}} &= 1, \end{aligned}$$

where $C_{1,p}$ and $C_{1,\bar{p}}$ are the mean values of proton and antiproton, respectively.

On the other hand, it is expected that close to the CP the three- and four-particle correlations are dominant relative to two-particle correlations [46]. The various orders integrated correlation functions of proton and antiproton (κ_n , also known as factorial cumulants) are related to the corresponding proton and antiproton cumulants (C_n) through the following relations [98–100]:

$$\begin{aligned} \kappa_1 &= C_1 = \langle N \rangle, \\ \kappa_2 &= -C_1 + C_2, \\ \kappa_3 &= 2C_1 - 3C_2 + C_3, \\ \kappa_4 &= -6C_1 + 11C_2 - 6C_3 + C_4, \\ C_2 &= \kappa_2 + \kappa_1, \\ C_3 &= \kappa_3 + 3\kappa_2 + \kappa_1, \\ C_4 &= \kappa_4 + 6\kappa_3 + 7\kappa_2 + \kappa_1, \end{aligned} \quad (7)$$

where C_1 and κ_1 represent the mean values for protons or antiprotons. For proton and antiproton cumulant ratios C_2/C_1 , C_3/C_2 , and C_4/C_2 , they can be expressed in terms of corresponding normalized correlation functions κ_n/κ_1 ($n > 1$) as

$$\frac{C_2}{C_1} = \frac{\kappa_2}{\kappa_1} + 1, \quad (8)$$

$$\frac{C_3}{C_2} = \frac{\kappa_3/\kappa_1 - 2}{\kappa_2/\kappa_1 + 1} + 3, \quad (9)$$

$$\frac{C_4}{C_2} = \frac{\kappa_4/\kappa_1 + 6\kappa_3/\kappa_1 - 6}{\kappa_2/\kappa_1 + 1} + 7. \quad (10)$$

The higher-order integrated correlation functions κ_n ($n > 1$) are equal to zero when the distributions are Poisson. Thus, κ_n can be used to quantify the deviations from the Poisson distributions in terms of n -particle correlations. For simplicity, from here on, we refer to the κ_n as correlation functions instead of integrated correlation functions.

In the following subsections, we discuss corrections that are related to collision centrality bin width (Sec. II F) and detection efficiency (Sec. II G). This is followed by the estimation of statistical and systematic uncertainties in Secs. II H and II I, respectively.

F. Centrality bin width correction

Data presented in this paper are classified into the following centrality bins: 0–5%, 5–10%, 10–20%, 20–30%, 30–40%, 40–50%, 50–60%, 60–70%, and 70–80%. The finite size of centrality bins implies that the average number of protons and antiprotons varies even within a centrality class. This variation has to be accounted for while calculating the cumulants in a broad centrality class. In addition, it is known that calculating cumulants in such broad centrality bins leads

to a strong enhancement of cumulants and cumulant ratios due to initial volume fluctuations [91,101].

A centrality bin width correction (CBWC) is the procedure used to take care of the measurements in a wide centrality bin and is based on weighting the cumulants measured at each multiplicity bin by the number of events in the bin [91,92,101]. This procedure is mathematically expressed in the equation below:

$$C_n = \frac{\sum_r n_r C_n^r}{\sum_r n_r} = \sum_r \omega_r C_n^r, \quad (11)$$

where the n_r is the number of events at the r th multiplicity bin for the centrality determination, the C_n^r represents the n th-order cumulant of particle number distributions at r th multiplicity. The corresponding weight for the r th multiplicity bin is $\omega_r = n_r / \sum_r n_r$.

As an example, Fig. 4 shows the C_n up to the fourth order as a function of $\langle N_{\text{part}} \rangle$ for three different collision energies: $\sqrt{s_{NN}} = 7.7, 19.6,$ and 62.4 GeV. For each C_n case, four different results are shown. One of them is the CBWC result for nine collision centrality bins, which correspond to 0–5%, 5–10%, 10–20%, 20–30%, ..., 70–80%. For comparison, cumulants are also calculated for the other three cases, which are 10%, 5%, and 2.5% centrality bin width without CBWC. The higher-order cumulant results with 10% centrality bins are found to have significant deviations compared to those with 5% and 2.5% centrality bins without CBWC. This finding means that it is important to correct for the CBW effect, as one normally expects that, irrespective of the centrality bin width, the cumulant values should exhibit the same dependence on $\langle N_{\text{part}} \rangle$. It is found that the results get closer to CBWC results with narrower centrality bins and the results with 2.5% centrality bins almost overlap with CBWC results, which indicates that the CBWC can effectively suppress the effect of the volume fluctuations on cumulants (up to the fourth order) within a finite centrality bin width.

For comparison, a different approach, the volume fluctuation correction (VFC) method [102,103], which assumes independent production of protons, has been also applied at $\sqrt{s_{NN}} = 7.7, 19.6,$ and 62.4 GeV for 0–5% Au+Au central collisions. The correction factors are determined by the Glauber model [103]. Figure 5 shows the comparison between the results based on CBWC and VFC methods. As can be seen from the plot, for the 0–5% central collisions, the results of CBWC and VFC are found to be consistent within statistical uncertainties. However, UrQMD model studies reported in Ref. [94], indicate that the VFC method (as discussed in Ref. [102]) does not work, as the independent particle production model assumed in the VFC is expected to be broken. Therefore, we follow the data-driven method, CBWC, in this paper.

G. Efficiency correction

Figure 6 shows the efficiency-uncorrected C_n for proton, antiproton, and net-proton multiplicity distributions in Au+Au collisions at $\sqrt{s_{NN}} = 7.7$ –200 GeV as a function of $\langle N_{\text{part}} \rangle$. This section discusses the method of efficiency correction. One such method is called the binomial-model-based method [80,100,104–106] and another

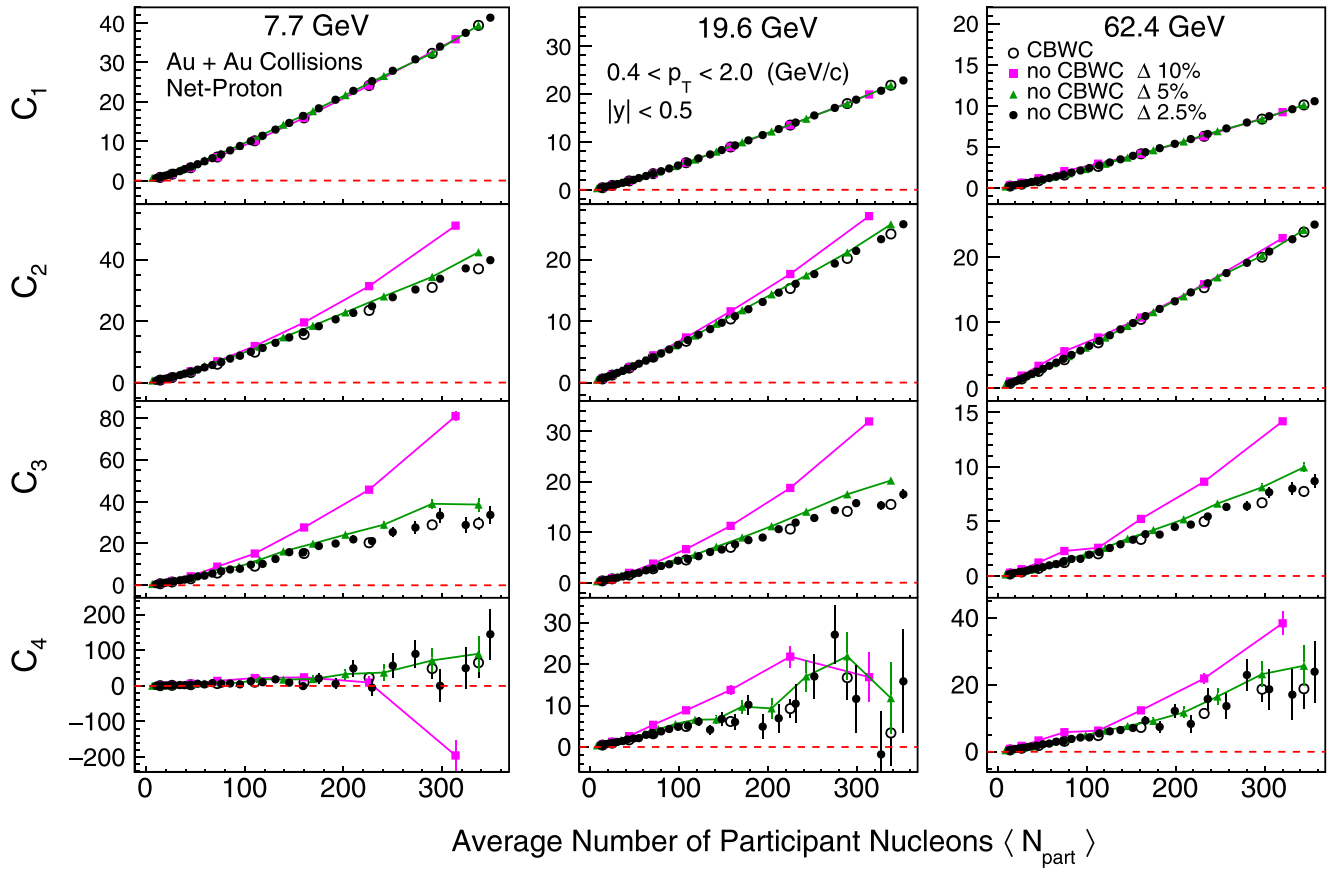


FIG. 4. C_n of net-proton distributions in Au+Au collisions at $\sqrt{s_{NN}} = 7.7, 19.6,$ and 62.4 GeV as a function of $\langle N_{\text{part}} \rangle$. The results are shown for 10%, 5%, and 2.5% centrality bins without CBWC and for nine centrality bins (0–5%, 5–10%, 10–20%, ..., 70–80%) with CBWC. The bars are the statistical uncertainties.

is the unfolding method [107,108]. The cumulants presented in the subsequent sections are corrected for efficiency and acceptance effects related to proton and antiproton reconstruction, unless specified otherwise.

1. Binomial model method

The binomial-based method involves two steps. First we obtain the efficiency of proton and antiproton reconstruction in the STAR detector and then correct the cumulants for efficiency and acceptance effects using analytic expressions. The former uses the embedding process and the latter invokes binomial model assumptions for the detector response function for the efficiencies. One can find more details in Appendix A.

The detector acceptance and the efficiency of reconstructing proton and antiproton tracks are determined together by embedding Monte Carlo (MC) tracks, simulated using the GEANT [109] model of the STAR detector response, into real events at the raw data level. One important requirement is the matching of the distributions of reconstructed embedded tracks and real data tracks for quantities reflecting track quality and those used for track selection [8]. The ratio of the distribution of reconstructed to embedded Monte Carlo tracks as a function of p_T gives the efficiency \times acceptance correction factor [$\varepsilon_{\text{TPC}}(p_T)$] for the rapidity interval studied. We refer to this factor as simply efficiency.

The current analysis makes use of both the TPC and the TOF detectors. While the TPC identifies low p_T ($0.4 < p_T < 0.8$ GeV/c) protons and antiprotons with high purity, the TOF gives better particle identification than the TPC in the higher p_T range ($0.8 < p_T < 2.0$ GeV/c). However, not all TPC tracks have valid TOF information due to the limited TOF acceptance and the mismatching of the TPC tracks to TOF hits. This extra efficiency is called the TOF-matching efficiency [$\varepsilon_{\text{TOF}}(p_T)$]. The TOF-matching efficiency is particle-species dependent and can be obtained using a data-driven technique, which is defined as the ratio of the number of (anti)proton tracks detected in the TOF to the total number of (anti)proton tracks in the TPC within the same acceptance [8]. Thus, the final average (anti)proton efficiency within a certain p_T range can be calculated as

$$\langle \varepsilon \rangle = \frac{\int_{p_{T1}}^{p_{T2}} \varepsilon(p_T) f(p_T) dp_T}{\int_{p_{T1}}^{p_{T2}} f(p_T) dp_T}, \quad (12)$$

where the p_T -dependent efficiency, $\varepsilon(p_T)$, is defined as $\varepsilon(p_T) = \varepsilon_{\text{TPC}}(p_T)$ for $0.4 < p_T < 0.8$ GeV/c and $\varepsilon(p_T) = \varepsilon_{\text{TPC}}(p_T) \times \varepsilon_{\text{TOF}}(p_T)$ for $0.8 < p_T < 2.0$ GeV/c. The function $f(p_T)$ is the efficiency-corrected p_T spectrum for (anti)protons [8].

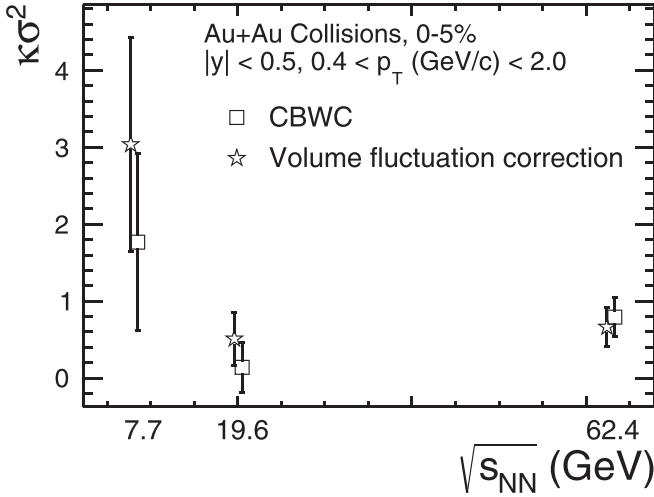


FIG. 5. $\kappa\sigma^2$ as a function of collision energy for Au+Au collisions for 0–5% centrality. The data have been corrected for volume fluctuation effects using CBWC, a data driven approach, and a model-dependent volume fluctuation correction method. The bars are the statistical uncertainties.

Figure 7 shows the average efficiency ($\langle \varepsilon \rangle$) for protons and antiprotons at midrapidity ($|y| < 0.5$) as a function of collision centrality ($\langle N_{\text{part}} \rangle$). For $0.4 < p_T < 0.8$ GeV/c the efficiency is only from the TPC and for $0.8 < p_T < 2.0$ GeV/c it is the product of efficiencies from the TPC and TOF. In Fig. 7, only statistical uncertainties are presented and a $\pm 5\%$ systematic uncertainty associated with determining the efficiency is considered in the analysis.

2. Unfolding method

In this section we discuss the effect of efficiency correction on the C_n measurement if the assumption of binomial detector efficiency response breaks down due to some of the reasons given in Refs. [110,111]. The technique is based on unfolding of the detector response [107,108]. The response function is obtained by MC simulations carried out in the STAR detector environment [109]. MC tracks are simulated through GEANT and embedded in the real data, and track reconstruction is performed as is done in the real experiment. Many effects can lead to nonbinomial detector response in heavy-ion experiments. One of those effects could be track merging due to the extreme environment of high particle multiplicity densities in the detector. Hence, we have performed the embedding simulations using the real data for 0–5% Au+Au collisions at $\sqrt{s_{NN}} = 200$ GeV. The numbers of embedded tracks of N_p and $N_{\bar{p}}$ are varied within $5 \leq N_{p(\bar{p})} \leq 40$. Since we are measuring the net-proton multiplicity distributions, protons and antiprotons are embedded simultaneously. We have shown in Ref. [112] that, for the event statistics in the current analysis, the efficiencies for kaon reconstruction follow binomial distributions.

Figure 8 shows the reconstructed protons from the embedding data (black circles) of Au+Au collisions at $\sqrt{s_{NN}} = 200$ GeV and 0–2.5% collision centrality. Each panel represents a different number of embedded (anti)protons. These distri-

butions are fitted by a binomial distribution (red solid line) at a fixed efficiency ε . The ratios of the fitted function to the embedding data are shown in the lower panels. The fitted χ^2/ndf ranges from 5.2 to 17.8 and the tails of the distributions are not well described by the binomial distribution for several combinations of embedded N_p and $N_{\bar{p}}$ tracks. We find that the embedding data is better described by a beta-binomial distribution given by

$$\beta(n; N, a, b) = \int_0^1 dp B(\varepsilon, a, b) B(n; N, \varepsilon), \quad (13)$$

and with the beta distribution given as

$$\beta(\varepsilon; a, b) = \varepsilon^a (1 - \varepsilon)^b / B(a, b), \quad (14)$$

where $B(a, b)$ is the beta function. The beta-binomial distribution is given by an urn model. Let us consider N_w white balls and N_b black balls in the urn. One draws a ball from the urn. If it is white (black), return two white (black) balls to the urn. This procedure is repeated with N times, then the resulting distribution of n white balls is given by the beta-binomial distributions as $\beta(n; N, N_w, N_b)$. This is actually equivalent to $\beta(n; N, \alpha, \varepsilon)$, where $N_w = \alpha N$ with $\varepsilon = N_w / (N_w + N_b)$. A smaller α gives a broader distribution than the binomial, while the distribution becomes close to the binomial distribution with a larger value of α .

The beta-binomial distributions are numerically generated with various values of α . These are compared to the embedding data to determine the best fit parameter value of α . The green lines in Fig. 8 show the beta-binomial distribution for the value of α that gives the minimum χ^2/ndf . It is found that $\chi^2/\text{ndf} \approx 1$ for most $(N_p, N_{\bar{p}})$ combinations. With this additional parameter α , it is found that the detector response is better described in the tails by a beta-binomial distribution compared to a binomial distribution.

From the embedding simulations as discussed above, the ε and α are parametrized as a function of N_p and $N_{\bar{p}}$. Using the parametrization, a four-dimensional response matrix between generated and reconstructed protons and antiprotons is generated with 1 billion events. The limited statistics in the embedding simulations lead to uncertainties on the α values. Therefore, two more response matrices are generated using $\alpha - \sigma$ and $\alpha + \sigma$, where σ is the statistical uncertainty on the α values determined by the embedding simulation. Furthermore, the standard response matrices are also generated with the binomial distribution as a reference using a multiplicity-dependent efficiency. These response matrices are used to correct for the detector effects as a confirmation of this approach by comparing to the binomial correction method described in the previous section. The consistency of the unfolding method has been checked through a detailed simulation and an analytic study.

Figure 9 shows the unfolded net-proton distributions for 200 GeV Au+Au collisions at 0–2.5% centrality. Results from four assumptions on the detector response are shown, one is the binomial detector response and the other three assume the beta-binomial distributions with different non-binomial α values. The ratios of the beta-binomial unfolded distributions to the binomial unfolded distributions are shown

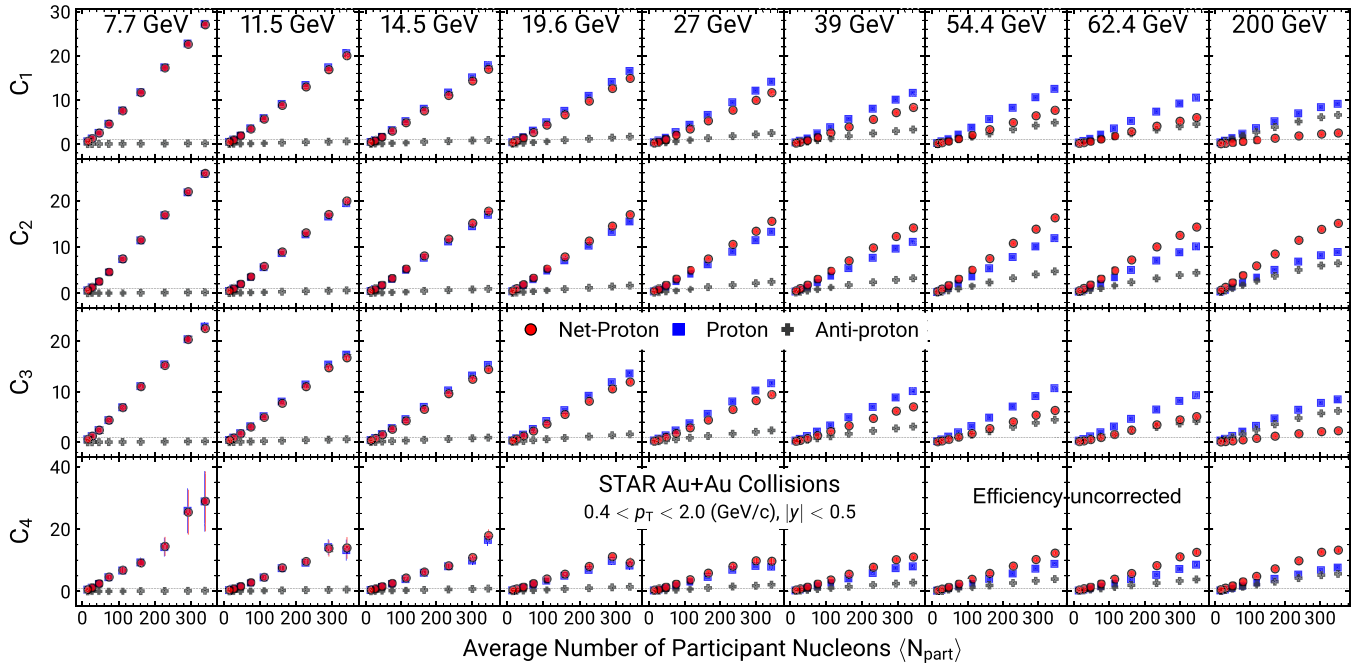


FIG. 6. Efficiency-uncorrected C_n of net-proton, proton, and antiproton multiplicity distributions in Au+Au collisions at $\sqrt{s_{NN}} = 7.7$ –200 GeV as a function of $\langle N_{\text{part}} \rangle$. The results are CBW corrected. The bars are the statistical uncertainties.

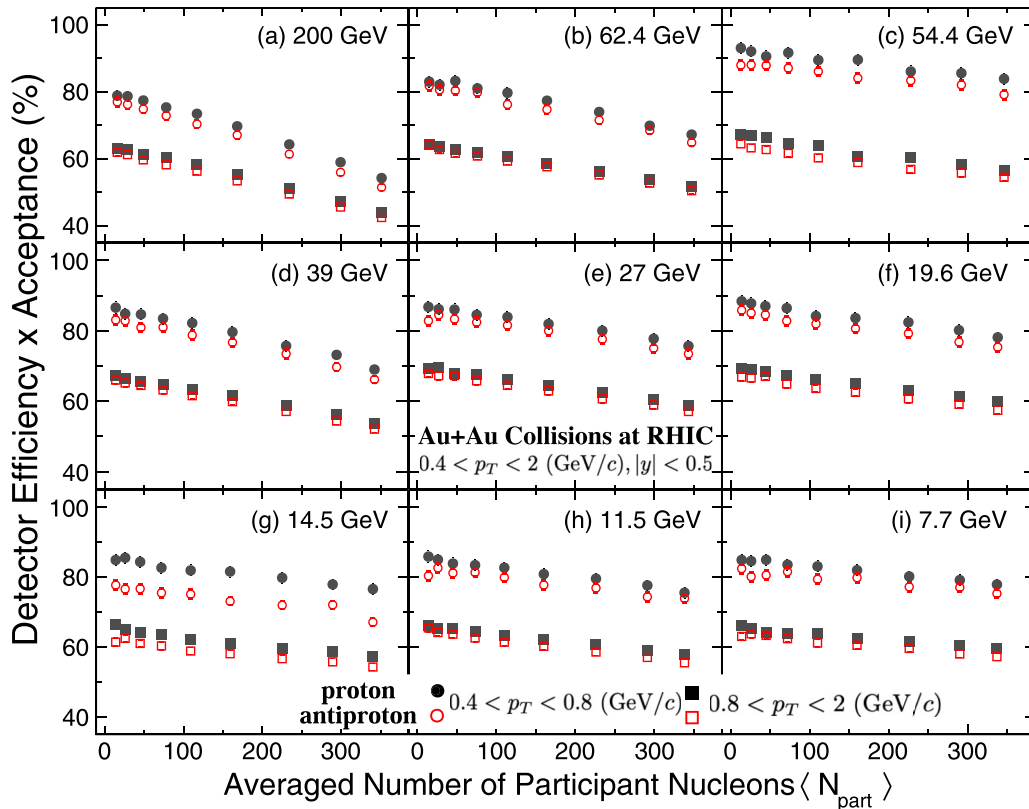


FIG. 7. Efficiencies of proton and antiproton as a function of $\langle N_{\text{part}} \rangle$ in Au+Au collisions for various $\sqrt{s_{NN}}$. For the lower p_T range ($0.4 < p_T < 0.8$ GeV/c), only the TPC is used. For the higher p_T range ($0.8 < p_T < 2.0$ GeV/c), both the TPC and TOF are used.

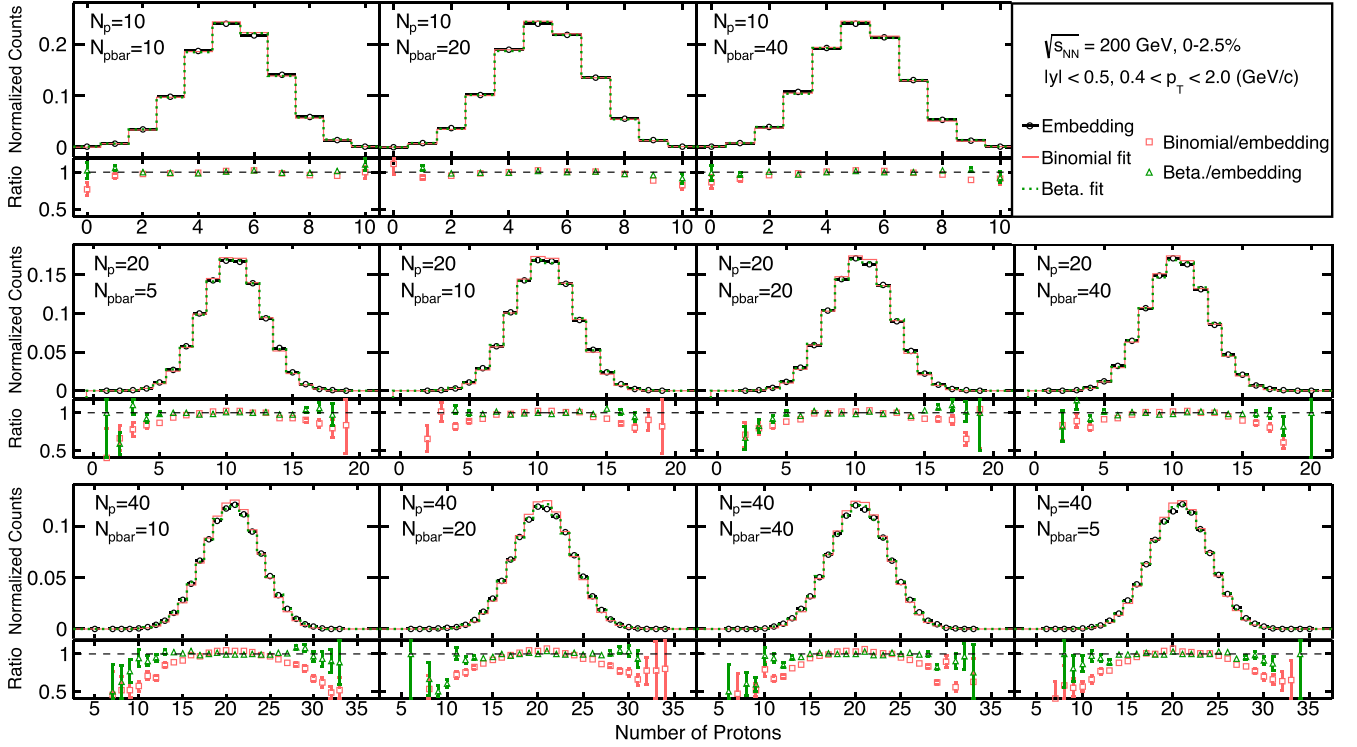


FIG. 8. Distributions of reconstructed protons (black circles) from embedding simulations in 200 GeV top 2.5%-central Au+Au collisions. Red lines are fits to the binomial distribution, and green dotted lines represent the fit with the beta-binomial distributions using the α that gives the minimum χ^2/ndf . Each panel presents results for a different combination of the number of embedded protons and antiprotons as labeled in the legend. The ratio of the fits to the embedding data is shown for each panel at the bottom.

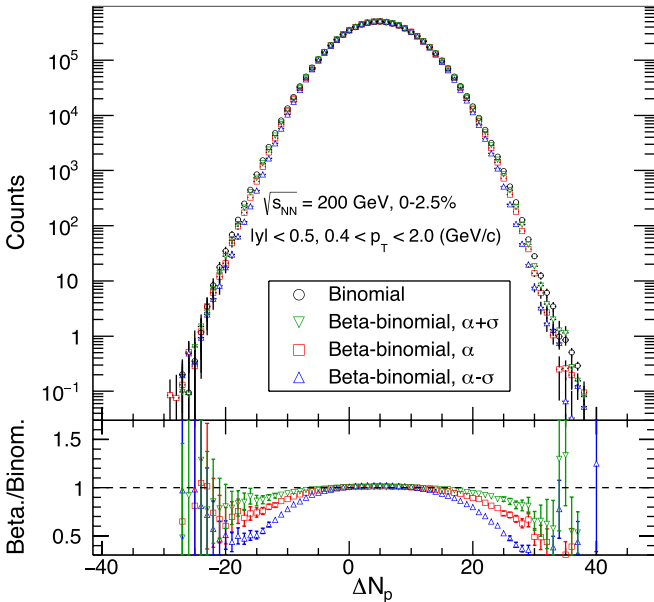


FIG. 9. Unfolded net-proton multiplicity distributions for $\sqrt{s_{NN}} = 200$ GeV Au+Au collisions where the binomial distribution (black circle), beta-binomial distributions with $\alpha + \sigma$ (green triangle), α (red square), and $\alpha - \sigma$ (blue triangle) are utilized in response matrices. Ratios of the beta-binomial unfolded distributions to that from binomial response matrices are shown in the bottom panel.

in the bottom panel. The unfolded distributions with beta-binomial response matrices are found to be narrower with a decreasing value of α . Calculations are done for 0–2.5% and 2.5–5.0% centralities separately and averaged to determine the C_n values for the 0–5% centrality. The C_n values and their ratios from data obtained using the binomial model of efficiency correction and those using the binomial detector response matrix in the unfolding method are consistent. Table V summarizes the cumulant ratios and their

TABLE V. Net-proton cumulant ratios and their statistical errors for 0–5% central Au+Au collisions at $\sqrt{s_{NN}} = 200$ GeV, (second column) from the conventional efficiency correction with the binomial detector response, and (third column) from unfolding with the beta-binomial detector response. Systematic errors are also shown for the beta-binomial case. The last column shows the difference between two results normalized by total uncertainty, which is equal to the statistical and systematic uncertainties summed in quadrature.

Cumulant ratio	Binomial	Beta	Significance
	\pm statistical error	\pm statistical error \pm systematical error	
C_2/C_1	$1.3 \pm \text{neg.}$	$1.20 \pm \text{neg.} \pm 0.03$	3.1
C_3/C_2	0.13 ± 0.01	$0.13 \pm 0.01 \pm \text{neg.}$	4.8×10^{-2}
C_4/C_2	1.10 ± 0.21	$0.97 \pm 0.21 \pm 0.08$	4.2×10^{-1}
C_5/C_1	0.10 ± 0.48	$-0.14 \pm 0.44 \pm 0.11$	3.8×10^{-1}
C_6/C_2	-0.45 ± 0.24	$-0.14 \pm 0.20 \pm 0.07$	1.0

errors. Results are also obtained from the unfolding method using the beta-binomial response function with nonbinomial parameters in the range $\alpha \pm \sigma$. This range in values of α is used to generate the systematic uncertainties associated with the unfolding method. The deviations of those nonbinomial efficiency-corrected results with respect to the conventional efficiency correction with binomial detector response is found to be 3.1σ for C_2/C_1 and less than 1.0σ for C_4/C_2 and for C_3/C_2 . The σ value is the statistical and systematic uncertainties added in quadrature.

These studies have been done for Au+Au collisions for the highest collision energy of $\sqrt{s_{NN}} = 200$ GeV and top-most 5% centrality. This set of data provides the largest charged-particle-density environment for the detectors, where we expect the maximum non-binomial detector effects. Even in this situation, the differences in the two methods of efficiency correction are at a level of less than one σ . Thus, we conclude that the nonbinomial detector effects on higher-order cumulant ratios presented in this work are within the uncertainties quoted for all of the BES-I energies.

H. Statistical uncertainty

The higher-order cumulants are sensitive to the shape of the distribution, and estimating their statistical uncertainty is crucial due to the limited available statistics. It has been shown that, among the various methods of obtaining statistical uncertainty on cumulants, the delta theorem method [113] and the bootstrap method [91,104,114–116] are the most reliable ones. Below we briefly discuss the two methods and show that the uncertainty values obtained up to the fourth-order cumulant from both methods are consistent.

The delta theorem method gives a concise form of standard error propagation method. This method of statistical uncertainty estimation uses the central limit theorem (CLT). The variance of the statistic ϕ can be calculated as

$$V(\phi) = \sum_{i,j=1}^m \left(\frac{\partial \phi}{\partial X_i} \right) \left(\frac{\partial \phi}{\partial X_j} \right) \text{Cov}(X_i, X_j), \quad (15)$$

where the $\text{Cov}(X_i, X_j)$ is the covariance between random variables X_i and X_j . Thus, we need to know the covariance between X_i and X_j to calculate the statistical errors.

If particle multiplicities follow a Gaussian distribution with width σ , the statistical uncertainty of the cumulants and cumulant ratios at different orders can be estimated as

$$\text{error}(C_m) \propto \frac{\sigma^m}{\sqrt{N} \varepsilon^\alpha}, \quad \text{error}(C_n/C_2) \propto \frac{\sigma^{n-2}}{\sqrt{N} \varepsilon^\beta}, \quad (16)$$

where m and n are integer numbers with $m \geq 1$ and $n \geq 2$, and α and β are real numbers with $\alpha > 0$ and $\beta > 0$. The N and ε denote the number of events and the particle-reconstruction efficiency, respectively. Thus, one can find that the statistical uncertainty strongly depends on the width (σ) of the distributions. For similar event statistics, due to the increasing width of the net-proton distributions from peripheral to central collisions, the statistical uncertainties are larger in central collisions than those from peripheral collisions. Furthermore, the reconstruction efficiency increases the statistical uncer-

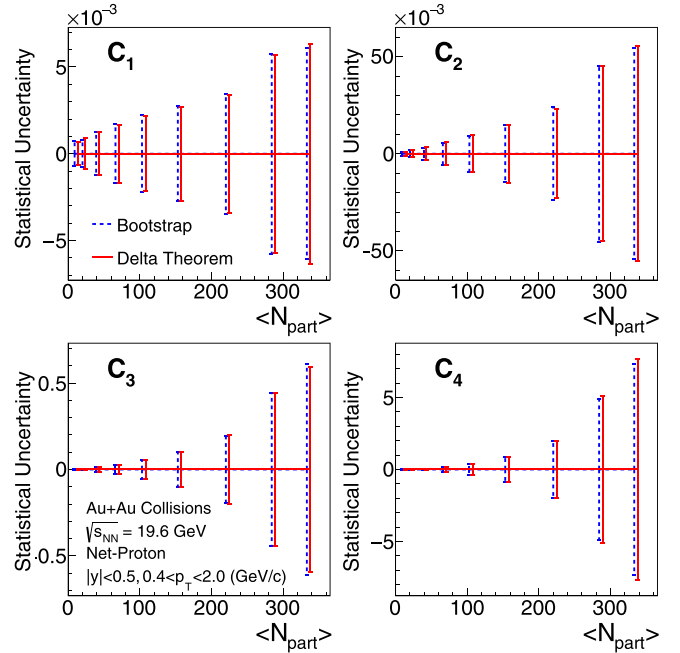


FIG. 10. Comparison of the statistical uncertainties on C_n of net-proton distributions in Au+Au collisions at $\sqrt{s_{NN}} = 19.6$ GeV from the delta theorem and bootstrap methods. The results are presented as a function of $\langle N_{\text{part}} \rangle$.

tainties on the cumulants compared to their corresponding uncorrected case. A more detailed discussion can be found in Appendix B.

The bootstrap method finds the statistical uncertainties on the cumulants in a Monte Carlo way by forming bootstrap samples. It makes use of a random selection of elements with replacement from the original sample to construct bootstrap samples over which the sampling variance of a given order cumulant is calculated [115,116]. Let X be a random sample representing the experimental dataset. Let μ_r be the estimator of a statistic (such as mean or variance etc.), on which we intend to find the statistical error. Given a parent sample of size n , construct B number of independent bootstrap samples $X_1^*, X_2^*, X_3^*, \dots, X_B^*$, each consisting of n data points randomly drawn with replacement from the parent sample. Then evaluate the estimator in each bootstrap sample

$$\mu_r^* = \mu_r(X_b^*), \quad b = 1, 2, 3, \dots, B. \quad (17)$$

Then obtain the sampling variance of the estimator as

$$\text{Var}(\mu_r) = \frac{1}{B-1} \sum_{b=1}^B (\mu_r^* - \bar{\mu}_r)^2, \quad (18)$$

where $\bar{\mu}_r = \frac{1}{B} \sum_{b=1}^B (\mu_r^*)$. The value of B is optimized and, in general, the larger the value of B the better the estimate of the error.

Figure 10 shows the statistical uncertainties on various orders of C_n obtained using the delta theorem and bootstrap methods for Au+Au collisions at $\sqrt{s_{NN}} = 19.6$ GeV. The results are shown as a function of $\langle N_{\text{part}} \rangle$ for each C_n . The value of B is 200. Good agreement of the statistical uncertainties is

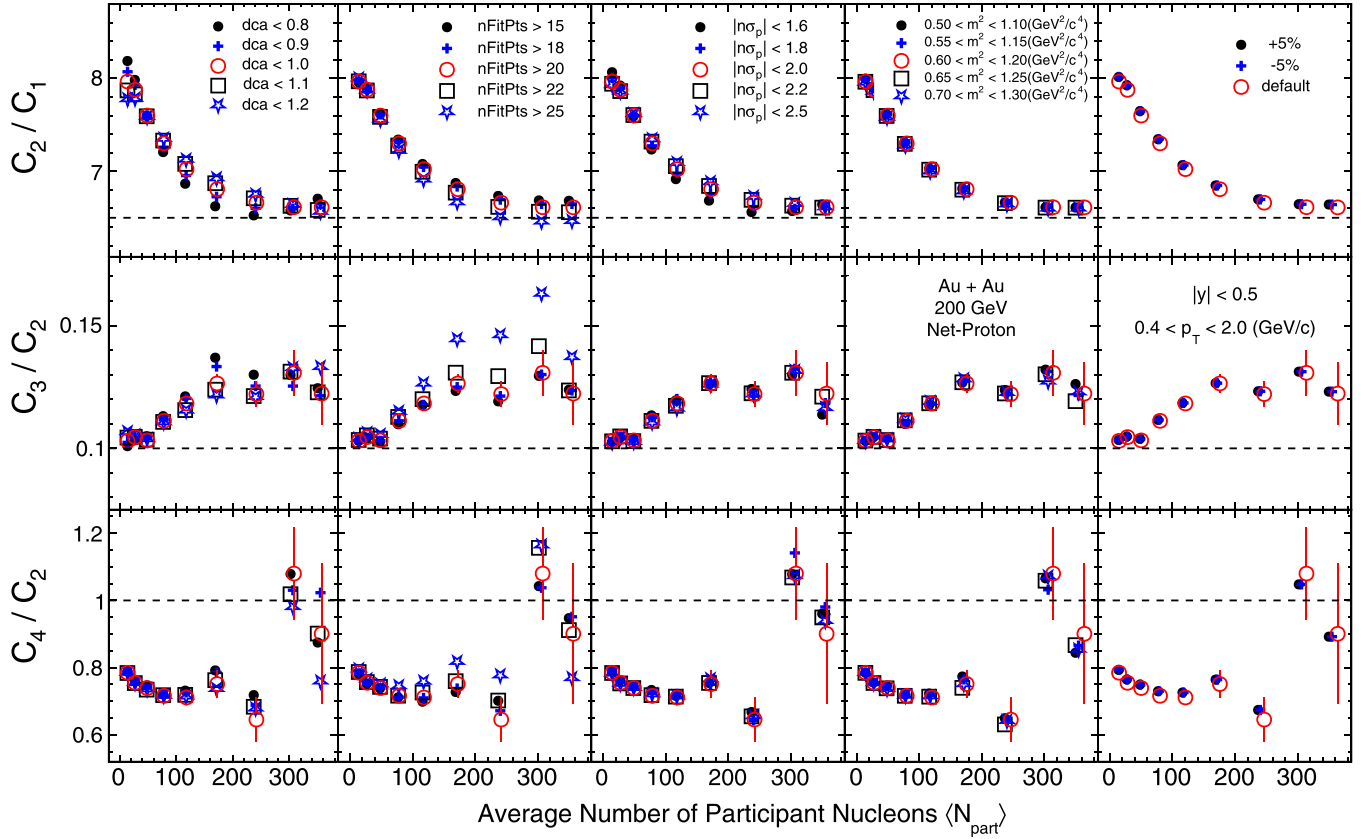


FIG. 11. Ratios of cumulants (C_n) as a function of $\langle N_{\text{part}} \rangle$, for net-proton distributions in Au+Au collisions at $\sqrt{s_{NN}} = 200$ GeV obtained by varying the analysis criteria in terms of track selection criteria, particle identification criteria, and efficiency. Since variations with respect to default selection criteria are used to obtain the systematic uncertainties on the measurements, the errors are shown only for the default case.

seen from both methods. The delta theorem method is used for obtaining the statistical uncertainties on the results discussed below.

I. Systematic uncertainty

Systematic uncertainties are estimated by varying the following requirements for p (\bar{p}) tracks: DCA, track quality (as reflected by the number of fit points used in track reconstruction), dE/dx , and m^2 for p (\bar{p}) identification [83]. A $\pm 5\%$ systematic uncertainty associated with determining the efficiency is also considered [8]. All of the different sources of systematic uncertainty are added in quadrature to obtain the final systematic uncertainties on the C_n and its ratios. Figure 11 shows the variations of the cumulants ratios with the changes in the above selection criteria for the net-proton distributions in Au+Au collisions at $\sqrt{s_{NN}} = 200$ GeV.

Table VI gives the systematic uncertainties on the C_n of the net-proton distribution for 0–5% central Au+Au collisions at $\sqrt{s_{NN}} = 7.7$ –200 GeV. The statistical and systematic uncertainties are presented separately in the figures.

III. RESULTS

In this section we present the efficiency-corrected cumulants and cumulant ratios of net-proton, proton, and antiproton multiplicity distributions in Au+Au collisions at $\sqrt{s_{NN}} =$

7.7, 11.5, 14.5, 19.6, 27, 39, 54.4, 62.4, and 200 GeV. The cumulants are related to the ratios of baryon number susceptibilities (χ_B) computed in QCD-motivated models as $\sigma^2/M = \chi_2^B/\chi_1^B$, $S\sigma = \chi_3^B/\chi_2^B$, and $\kappa\sigma^2 = \chi_4^B/\chi_2^B$ [44,50,76–78]. Normalized correlation functions (κ_n/κ_1 , $n > 1$) for the proton and antiproton extracted from the measured C_n are also presented. The statistical uncertainties on κ_n are obtained from the uncertainties on C_n using the standard error propagation method. These results will be also compared to corresponding results from a hadron resonance gas (HRG) [117] and hadronic-transport-based UrQMD model calculations [118,119].

In the following subsections, the dependence of the cumulants and correlation functions on collision energy, centrality, rapidity, and transverse momentum are presented. The corresponding physics implications are discussed.

A. Centrality dependence

In this subsection, we show the $\langle N_{\text{part}} \rangle$ (representing collision centrality) dependence of the cumulants, cumulant ratios, and normalized correlation functions in Au+Au collisions at $\sqrt{s_{NN}} = 7.7$ –200 GeV. To understand the evolution of the centrality dependence of the cumulants and cumulant ratios, we invoke the central limit theorem and consider the distribution at any given centrality i to be a superposition of several independent source distributions [35]. Assuming the average

TABLE VI. Total systematic uncertainty as well as the absolute uncertainties from individual sources, such as DCA and NHITSFIT, for net-proton C_n in 0–5% central Au+Au collisions at $\sqrt{s_{NN}} = 7.7$ –200 GeV. The total systematic uncertainties are obtained by adding the uncertainties from individual sources in quadrature.

$\sqrt{s_{NN}}$ (GeV)	Cumulant	Total	DCA	NHITSFIT	$N_{\sigma,p}$	m^2	Efficiency
7.7	C_1	2.42	0.85	0.78	0.99	0.028	1.88
	C_2	2.03	0.72	0.60	0.82	0.032	1.61
	C_3	1.65	0.60	0.97	0.54	0.31	1.02
	C_4	16.20	5.56	12.54	6.40	2.68	5.11
11.5	C_1	2.82	1.76	1.03	1.13	0.033	1.59
	C_2	2.34	1.44	0.73	0.99	0.020	1.37
	C_3	1.36	0.64	0.20	0.85	0.035	0.82
	C_4	7.37	2.28	4.10	4.94	2.60	1.06
14.5	C_1	1.72	0.77	0.54	0.76	0.03	1.22
	C_2	1.60	0.69	0.49	0.74	0.021	1.13
	C_3	1.16	0.52	0.44	0.51	0.047	0.78
	C_4	8.06	2.89	3.10	5.41	0.71	4.15
19.6	C_1	1.46	0.60	0.62	0.56	0.045	1.03
	C_2	1.46	0.62	0.62	0.57	0.041	1.02
	C_3	0.68	0.36	0.26	0.23	0.13	0.44
	C_4	3.65	0.86	1.99	2.58	0.59	0.89
27	C_1	1.20	0.51	0.53	0.47	0.025	0.83
	C_2	1.44	0.67	0.63	0.57	0.027	0.96
	C_3	0.62	0.33	0.27	0.23	0.035	0.39
	C_4	3.10	1.58	1.36	1.80	0.38	1.36
39	C_1	0.94	0.39	0.45	0.35	0.026	0.64
	C_2	1.48	0.67	0.67	0.59	0.033	0.97
	C_3	0.51	0.29	0.21	0.17	0.04	0.313
	C_4	3.35	1.00	2.76	1.43	0.20	0.65
54.4	C_1	0.81	0.43	0.33	0.20	0.034	0.56
	C_2	1.57	0.88	0.65	0.39	0.064	1.06
	C_3	0.42	0.27	0.15	0.078	0.025	0.27
	C_4	2.95	1.18	1.41	1.93	1.24	0.21
62.4	C_1	1.04	0.45	0.49	0.35	0.044	0.71
	C_2	2.15	1.05	1.087	0.79	0.11	1.31
	C_3	0.58	0.14	0.22	0.30	0.081	0.41
	C_4	3.99	2.40	2.30	1.38	1.21	1.23
200	C_1	0.39	0.19	0.24	0.11	0.01	0.22
	C_2	2.42	1.11	1.53	0.77	0.087	1.31
	C_3	0.39	0.24	0.18	0.19	0.074	0.14
	C_4	4.89	2.69	3.07	1.80	1.41	1.42

number of sources for a given centrality is proportional to the corresponding $\langle N_{\text{part}} \rangle$, the C_n should have a linear dependence on $\langle N_{\text{part}} \rangle$ and the ratios C_2/C_1 , C_3/C_2 and C_4/C_2 should be constant as a function of $\langle N_{\text{part}} \rangle$.

Figure 12 shows the $\langle N_{\text{part}} \rangle$ dependence of C_n for net-proton, proton, and antiproton distributions in Au+Au collisions at $\sqrt{s_{NN}} = 7.7$ –200 GeV. Since the cumulants are extensive quantities, the C_n for net-proton, proton, and antiproton increase with increasing $\langle N_{\text{part}} \rangle$ for all of the $\sqrt{s_{NN}}$ studied. The different mean values of the proton and antiproton distributions at each energy are determined by the interplay between proton-antiproton pair production and baryon stopping effects. At the lower $\sqrt{s_{NN}}$, the effects of baryon stopping at midrapidity are more important than at

higher $\sqrt{s_{NN}}$, and therefore the net-proton C_n has dominant contributions from protons. The small mean values for antiprotons at lower $\sqrt{s_{NN}}$ are due to their low rate of production. At higher $\sqrt{s_{NN}}$, the pair production process dominates the production of protons and antiprotons at midrapidity. The \bar{p}/p ratio for 0–5% central Au+Au collisions at $\sqrt{s_{NN}} = 200$ and 7.7 GeV are 0.769 and 0.007, respectively [8,120]. Large values of C_3 and C_4 also indicate that the net-proton, proton, and antiproton distributions are non-Gaussian. To facilitate plotting, the net-proton and proton C_4 from the 0–5% and 5–10% central Au+Au collisions at $\sqrt{s_{NN}} = 7.7$ GeV are scaled down by a factor of 2.

Figure 13 shows the $\langle N_{\text{part}} \rangle$ dependence of cumulant ratios C_2/C_1 , C_3/C_2 , and C_4/C_2 for net-proton, proton and antiproton distributions measured in Au+Au collisions at $\sqrt{s_{NN}} = 7.7$ –200 GeV. In terms of the moments of the distributions, they correspond to σ^2/M (C_2/C_1), σ (C_3/C_2), and $\kappa\sigma^2$ (C_4/C_2). The volume effects are canceled to the first order in these cumulant ratios. It is found that both of the proton and antiproton cumulant ratios C_2/C_1 and C_3/C_2 show weak variations with $\langle N_{\text{part}} \rangle$. Based on the HRG model with the Boltzmann approximation, the orders of baryon number fluctuations can be analytically expressed as $C_1^B/C_2^B = C_3^B/C_2^B = \tanh(\mu_B/T)$ and $C_4^B/C_2^B = 1$, where μ_B and T are the baryon chemical potential and temperature of the system, respectively. The values of net-proton C_2/C_1 show a monotonic decrease with increasing $\langle N_{\text{part}} \rangle$ while the values of C_3/C_2 show a slight increase with $\langle N_{\text{part}} \rangle$. For a fixed centrality, both net-proton C_2/C_1 and C_3/C_2 show strong energy dependence, which can be understood as $C_3/C_2 \propto \tanh(\mu_B/T)$ and $C_2/C_1 \propto 1/\tanh(\mu_B/T)$. At high $\sqrt{s_{NN}}$, the net-proton $C_3/C_2 \propto \tanh(\mu_B/T) \approx \mu_B/T \rightarrow 0$ and $C_2/C_1 \propto 1/\tanh(\mu_B/T) \approx T/\mu_B > 1$. Since the $\mu_B/T \gg 1$ for the lower energies, the values of net-proton C_2/C_1 and C_3/C_2 approach unity. Due to the connection between higher-order net-proton cumulant ratios and chemical freeze-out μ_B and T , those cumulant ratios have been extensively applied to probe the chemical freeze-out conditions and thermal nature of the medium created in heavy-ion collisions [121–123]. Finally, the net-proton and proton C_4/C_2 ratios have weak $\langle N_{\text{part}} \rangle$ dependence for energies above $\sqrt{s_{NN}} = 39$ GeV. For energies below $\sqrt{s_{NN}} = 39$ GeV, the net-proton and proton C_4/C_2 generally show a decreasing trend with increasing $\langle N_{\text{part}} \rangle$, except that, within current uncertainties, weak centrality dependences of C_4/C_2 are observed in Au+Au collisions at $\sqrt{s_{NN}} = 7.7$ and 11.5 GeV.

Figure 14 shows the variation of normalized correlation functions κ_n/κ_1 ($n > 1$) with $\langle N_{\text{part}} \rangle$ for protons and antiprotons in Au+Au collisions at $\sqrt{s_{NN}} = 7.7$ –200 GeV. As shown in Eqs. (8)–(10), the proton and antiproton cumulant ratios C_2/C_1 , C_3/C_2 , and C_4/C_2 can be expressed in terms of corresponding normalized correlation function κ_n/κ_1 . Therefore, the results shown in Fig. 14 provide important information on how different orders of multiparticle correlation functions of protons and antiprotons contribute to the cumulant ratios. The values of κ_1 are equal to mean C_1 values for protons and antiprotons, and linearly increase with $\langle N_{\text{part}} \rangle$ as shown in Fig. 12. The normalized two-particle correlation functions,

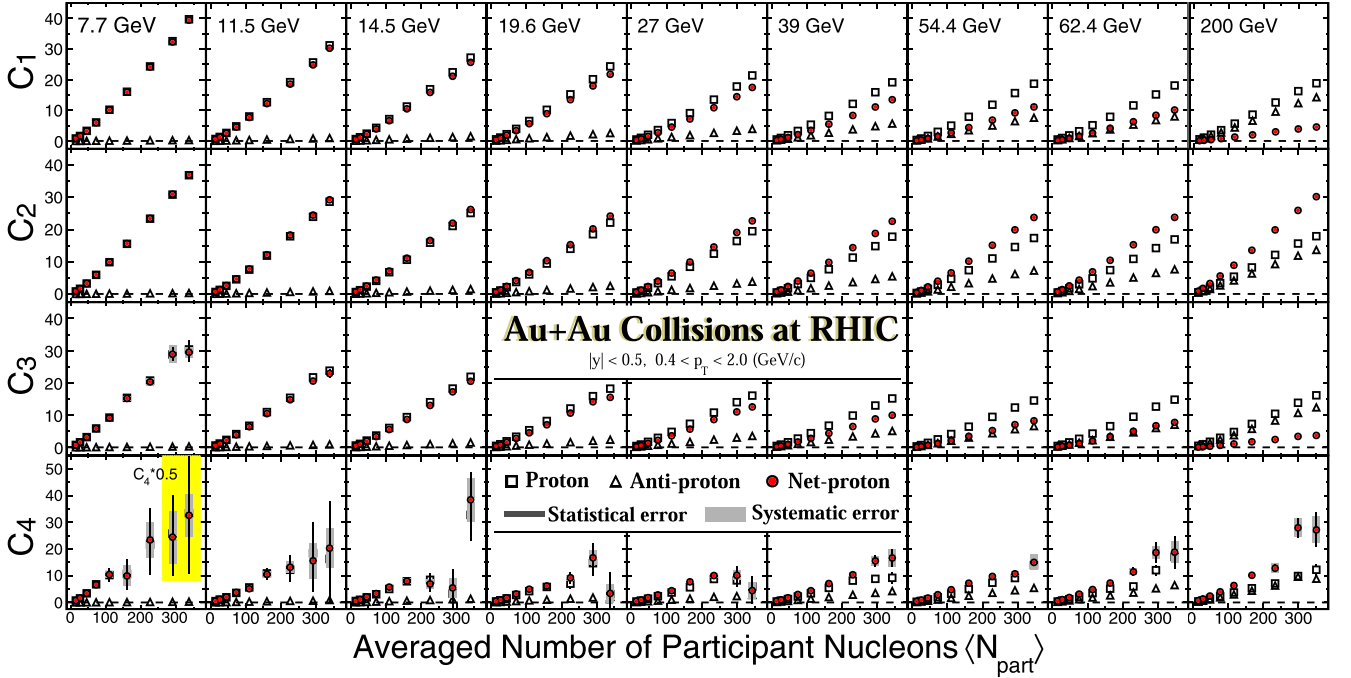


FIG. 12. Collision centrality dependence of proton (open squares), antiproton (open triangles), and net-proton (filled circles) cumulants from (7.7–200 GeV) Au+Au collisions at RHIC. The data are from $|y| < 0.5$ and $0.4 < p_T < 2.0$ GeV/c. Statistical and systematic uncertainties are shown as the narrow black and wide grey bands, respectively. Note that the net-proton and proton C_4 from 0–5% and 5–10% central Au+Au collisions at 7.7 GeV have been scaled down by a factor of 2, indicated in the yellow box.

κ_2/κ_1 , for protons and antiprotons are found to be negative for all $\langle N_{\text{part}} \rangle$. The values of proton and antiproton κ_2/κ_1 become comparable at $\sqrt{s_{NN}} = 200$ GeV but exhibit larger discrepancies at lower energies. This can be understood as the interplay between baryon stopping and pair production of protons and antiprotons as a function of $\sqrt{s_{NN}}$. Within current uncertainties, no statistically significant deviation from zero is observed in proton normalized correlation functions κ_3/κ_1 and κ_4/κ_1 as a function of collision centrality. As will be dis-

cussed later, however, one does observe nonmonotonic energy dependence of proton C_4/C_1 in the 0–5% central collisions; see Fig. 25. This is because, as defined in Eq. (7), the fourth-order cumulant C_4 contains contributions from second-, third-, and fourth-order correlation functions (factorial cumulants). In any case, high statistics data from the second phase of the RHIC beam energy scan program (BES-II) are needed to understand the origin of the observed dependences on both collision energy and centrality.

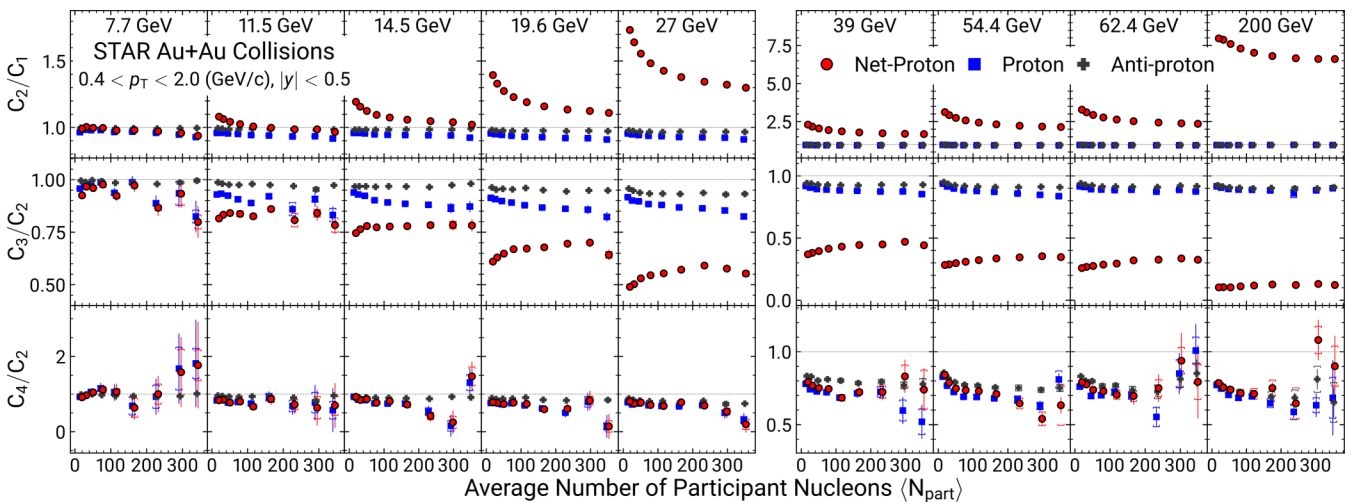


FIG. 13. Collision centrality dependence of the cumulant ratios of proton, antiproton and net-proton multiplicity distributions for Au+Au collisions at $\sqrt{s_{NN}} = 7.7, 11.5, 14.5, 19.6, 27, 39, 54.4, 62.4,$ and 200 GeV. The bars and caps represent the statistical and systematic uncertainties, respectively.

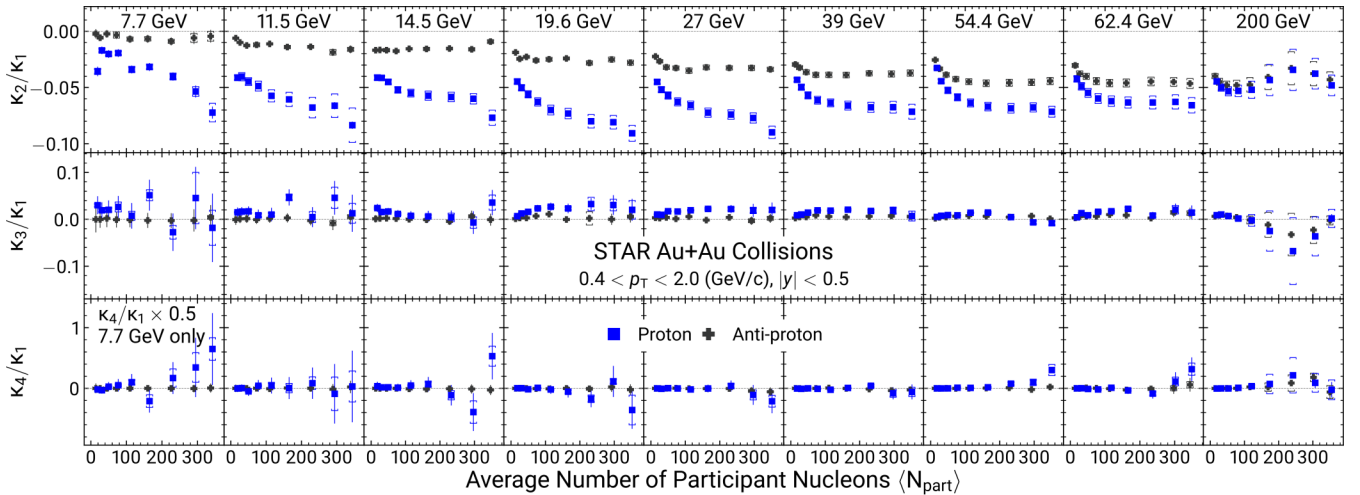


FIG. 14. Collision centrality dependence of normalized correlation functions κ_n/κ_1 ($n = 2, 3, 4$) for proton and antiproton multiplicity distributions in Au+Au collisions at $\sqrt{s_{NN}} = 7.7, 11.5, 14.5, 19.6, 27, 39, 54.4, 62.4,$ and 200 GeV. The bars and caps represent the statistical and systematic uncertainties, respectively. For clarity, the X-axis values for protons are shifted and the values of proton and antiproton κ_4/κ_1 at $\sqrt{s_{NN}} = 7.7$ GeV are scaled down by a factor of 2.

B. Acceptance dependence

In this subsection, we focus on discussing the acceptance dependence of the proton, antiproton, and net-proton cumulants (C_n) and cumulant ratios in 0–5% central Au+Au collisions at $\sqrt{s_{NN}} = 7.7$ –200 GeV. It was pointed out in Refs. [98,99,124,125] that, when the rapidity acceptance (Δy) is much smaller than the typical correlation length (ξ) of the system ($\Delta y \ll \xi$), the cumulants (C_n) and correlation functions (κ_n) should scale with some power n of the accepted mean particle multiplicities as $C_n, \kappa_n \propto (\Delta N)^n \propto (\Delta y)^n$. Meanwhile, in the regime where the rapidity acceptance becomes much larger than ξ ($\Delta y \gg \xi$), the C_n and κ_n scale linearly with mean multiplicities or Δy . Thus, the rapidity acceptance dependence of the higher-order cumulants and correlation functions of proton, antiproton, and net-proton distributions are important observables to search for a signature of the QCD critical point in heavy-ion collisions. On the other hand, that acceptance dependence of C_n and κ_n could be affected by the effects of nonequilibrium [69,71,126], smearing due to diffusion and hadronic re-scattering [126–129] in the dynamical expansion of the created fireball.

1. Rapidity dependence

Figure 15 shows the rapidity ($-y_{\max} < y < y_{\max}$, $\Delta y = 2y_{\max}$) dependence of the C_n for proton, antiproton, and net-proton distributions in 0–5% central Au+Au collisions at $\sqrt{s_{NN}} = 7.7$ –200 GeV. The measurements are made in the p_T range of 0.4 to 2.0 GeV/c. The rapidity acceptance is cumulatively increased and the C_n values for protons, antiprotons, and net protons increase with increasing rapidity acceptance. For $\sqrt{s_{NN}} < 27$ GeV, the proton and net-proton C_n have similar values, an inevitable consequence of the small production rate of antiproton at lower energies.

Figure 16 shows the variation of normalized correlation functions κ_n/κ_1 with rapidity acceptance for proton and antiproton in 0–5% central Au+Au collisions at $\sqrt{s_{NN}} =$

7.7–200 GeV. The κ_2/κ_1 values for protons and antiprotons are negative and monotonically increase in magnitude when enlarging the rapidity acceptance up to $y_{\max} = 0.5$ ($\Delta y = 1$). For the antiproton, the values of κ_2/κ_1 show stronger deviations from zero at higher $\sqrt{s_{NN}}$. As discussed around Fig. 14, the negative values of the two-particle correlation functions (κ_2) of protons and antiprotons are consistent with the expectation of the effect of baryon number conservation. Within current uncertainties, the rapidity acceptance dependences for the κ_3/κ_1 and κ_4/κ_1 of protons and antiprotons in Au+Au collisions at different $\sqrt{s_{NN}}$ are not significant. The significances of the proton κ_4/κ_1 with $|y| < 0.5$ deviating from zero are $1.04\sigma, 0.05\sigma, 1.27\sigma, 0.90\sigma, 0.95\sigma, 0.40\sigma, 2.91\sigma, 1.43\sigma, 0.11\sigma$ for 0–5% central Au+Au collisions at $\sqrt{s_{NN}} = 7.7, 11.5, 14.5, 19.6, 27, 39, 54.4, 62.4,$ and 200 GeV, respectively, where the σ is defined as the sum in quadrature of the statistical and systematic uncertainties.

Figure 17 shows the rapidity acceptance dependence of the cumulant ratios $C_2/C_1, C_3/C_2,$ and C_4/C_2 for protons, antiprotons, and net protons in 0–5% central Au+Au collisions at $\sqrt{s_{NN}} = 7.7$ –200 GeV. Based on Eqs. (8) to (10), the rapidity acceptance dependence of the cumulant ratios of proton and antiproton can be understood by the interplay between different orders of normalized correlation functions (κ_n/κ_1). The negative values of two-particle correlation functions (κ_2) for protons and antiprotons leads to a deviation of the corresponding C_2/C_1 and C_3/C_2 below unity. Due to low production rate of antiproton at low energies, the values of C_2/C_1 and C_3/C_2 for the net-proton distributions approach the corresponding values for protons when the beam energy decreases. The rapidity acceptance dependence of $C_2/C_1, C_3/C_2$ and C_4/C_2 values for protons and antiprotons are comparable at $\sqrt{s_{NN}} = 200$ GeV. However, among these ratios, protons and antiprotons start to deviate at lower beam energies. This is mainly due to baryon stopping and the larger fraction of transported protons compared with proton-antiproton pair production at midrapidity. The C_4/C_2 values for proton, antiproton, and

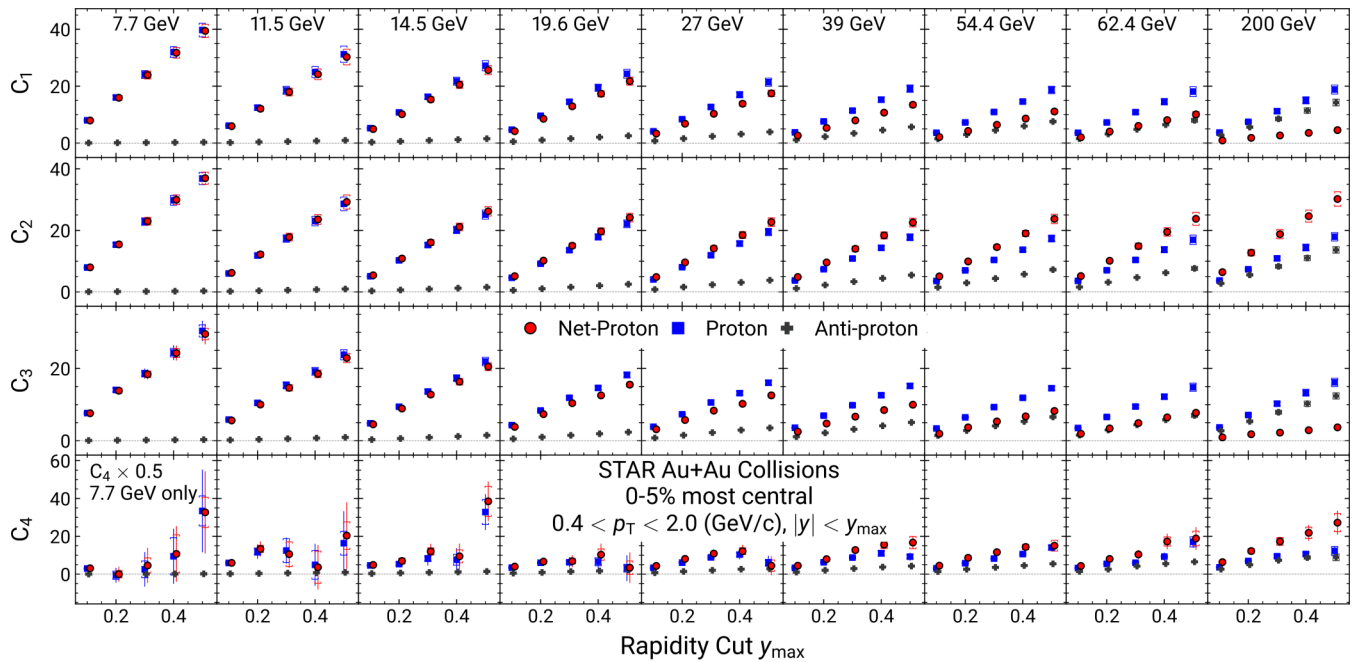


FIG. 15. Rapidity acceptance dependence of cumulants of proton, antiproton, and net-proton multiplicity distributions in 0–5% central Au+Au collisions at $\sqrt{s_{NN}} = 7.7, 11.5, 14.5, 19.6, 27, 39, 54.4, 62.4,$ and 200 GeV. The bars and caps represent statistical and systematic uncertainties, respectively. For clarity, the X-axis values for protons are shifted and the values of proton, antiproton, and net-proton C_4 at $\sqrt{s_{NN}} = 7.7$ GeV are scaled down by a factor of 2.

net-proton distributions are consistent within uncertainties for $\sqrt{s_{NN}} = 39, 54.4, 62.4,$ and 200 GeV. Significant deviations from unity are observed for proton and net-proton C_4/C_2 at $\sqrt{s_{NN}} = 19.6$ and 27 GeV, and the deviation decreases with decreasing Δy acceptance, where the effects of baryon num-

ber conservation plays an important role. For energies below 19.6 GeV, the rapidity acceptance dependence of C_4/C_2 for protons, antiprotons, and net protons is not significant within uncertainties.

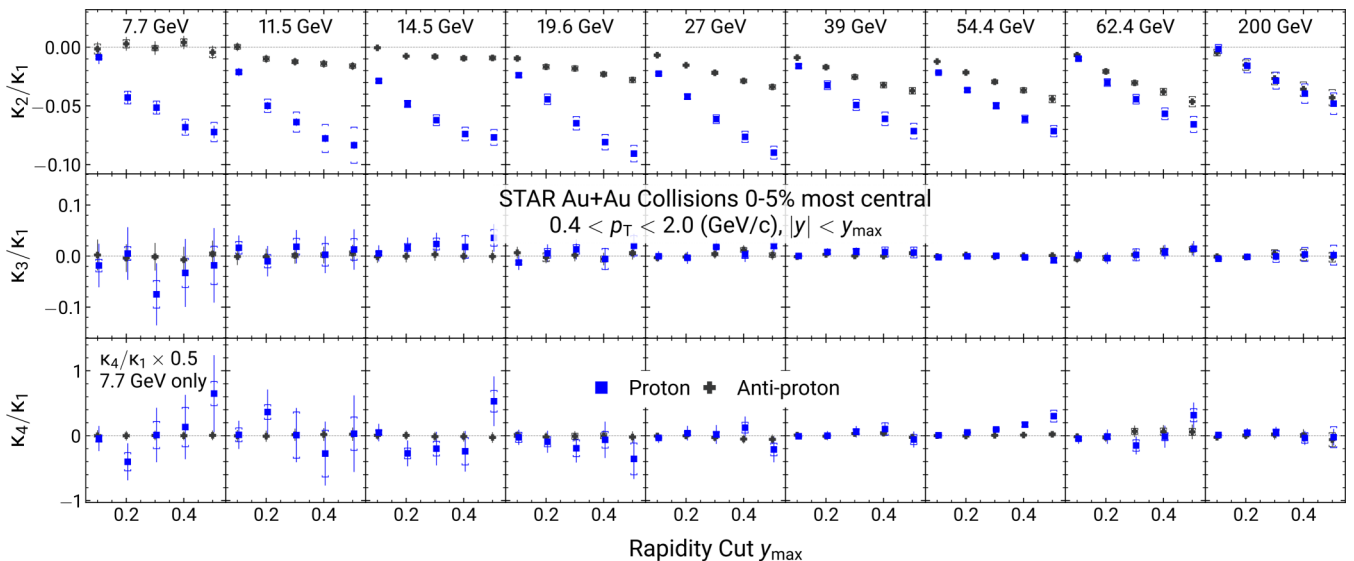


FIG. 16. Rapidity acceptance dependence of normalized correlation functions up to fourth order ($\kappa_n/\kappa_1, n = 2, 3, 4$) for proton and antiproton multiplicity distributions in 0–5% central Au+Au collisions at $\sqrt{s_{NN}} = 7.7, 11.5, 14.5, 19.6, 27, 39, 54.4, 62.4,$ and 200 GeV. The X-axis rapidity cut y_{\max} is applied as $|y| < y_{\max}$. The bars and caps represent statistical and systematic uncertainties, respectively. For clarity, the X-axis values for protons are shifted and the values of proton and antiproton κ_4/κ_1 at $\sqrt{s_{NN}} = 7.7$ GeV are scaled down by a factor of 2.

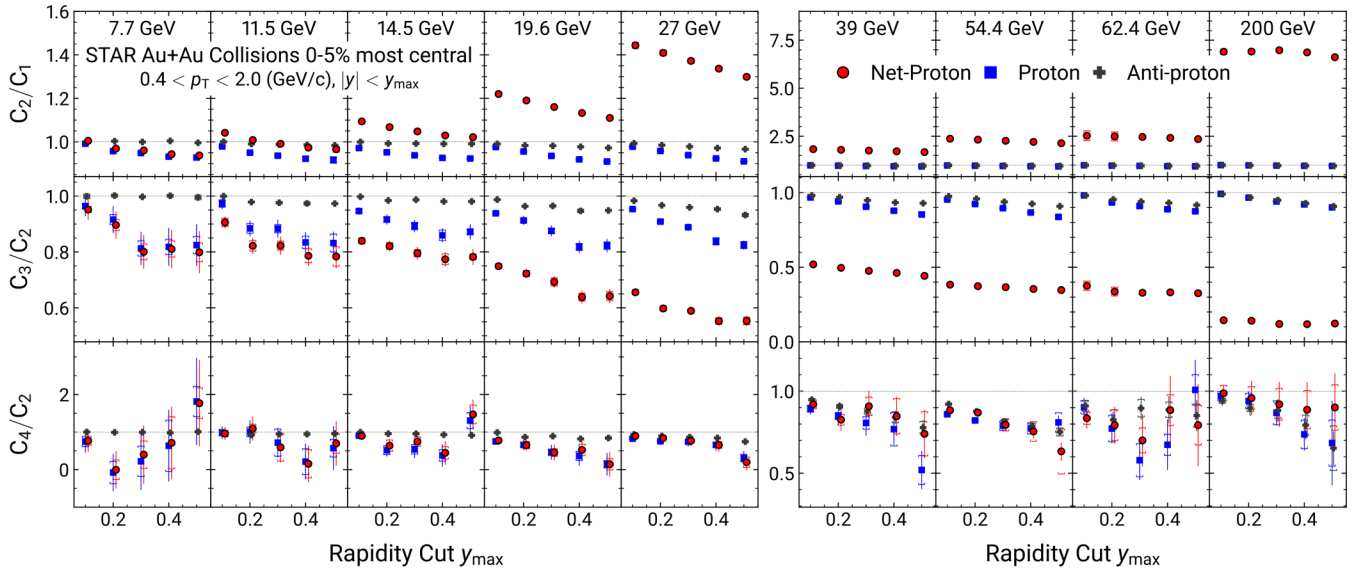


FIG. 17. Rapidity-acceptance dependence of cumulant ratios of proton, antiproton and net-proton multiplicity distributions in 0–5% central Au+Au collisions at $\sqrt{s_{NN}} = 7.7, 11.5, 14.5, 19.6, 27, 39, 54.4, 62.4,$ and 200 GeV. The bars and caps represent statistical and systematic uncertainties, respectively. For clarity, the X-axis values for net protons and protons are shifted.

2. Transverse momentum dependence

Figure 18 shows the p_T acceptance dependence for the C_n of proton, antiproton, and net-proton distributions at midrapidity ($|y| < 0.5$) for 0–5% central Au+Au collisions at $\sqrt{s_{NN}} = 7.7$ – 200 GeV. We fix the lower p_T cut at 0.4 GeV/c, and then the p_T acceptance is increased by varying the upper limit in steps between 1 and 2 GeV/c. The average efficiency values

used in the efficiency correction for various p_T acceptances are calculated based on Eq. (12). By extending the upper p_T coverage from 1 to 2 GeV/c, the mean numbers of protons increased about 50% and 80% at $\sqrt{s_{NN}} = 7.7$ and 200 GeV, respectively. It is found that the C_n values for protons, antiprotons, and net protons increase with increasing p_T acceptance, except for a weak p_T acceptance dependence for C_4 observed at energies below 39 GeV.

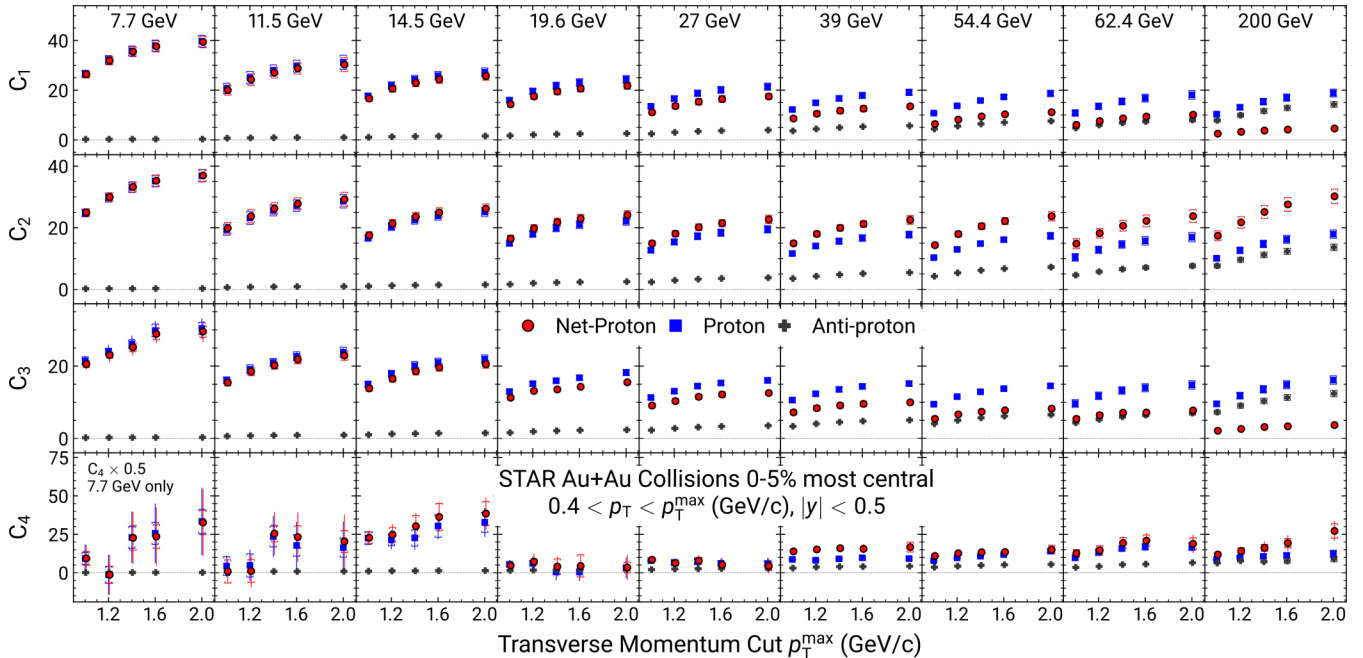


FIG. 18. p_T -acceptance dependence of cumulants of proton, antiproton, and net-proton multiplicity distributions for 0–5% central Au+Au collisions at $\sqrt{s_{NN}} = 7.7, 11.5, 14.5, 19.6, 27, 39, 54.4, 62.4,$ and 200 GeV. The bars and caps represent statistical and systematic uncertainties, respectively. For clarity, the X-axis values for net protons are shifted and the values of proton, antiproton, and net-proton C_4 at $\sqrt{s_{NN}} = 7.7$ GeV are scaled down by a factor of 2.

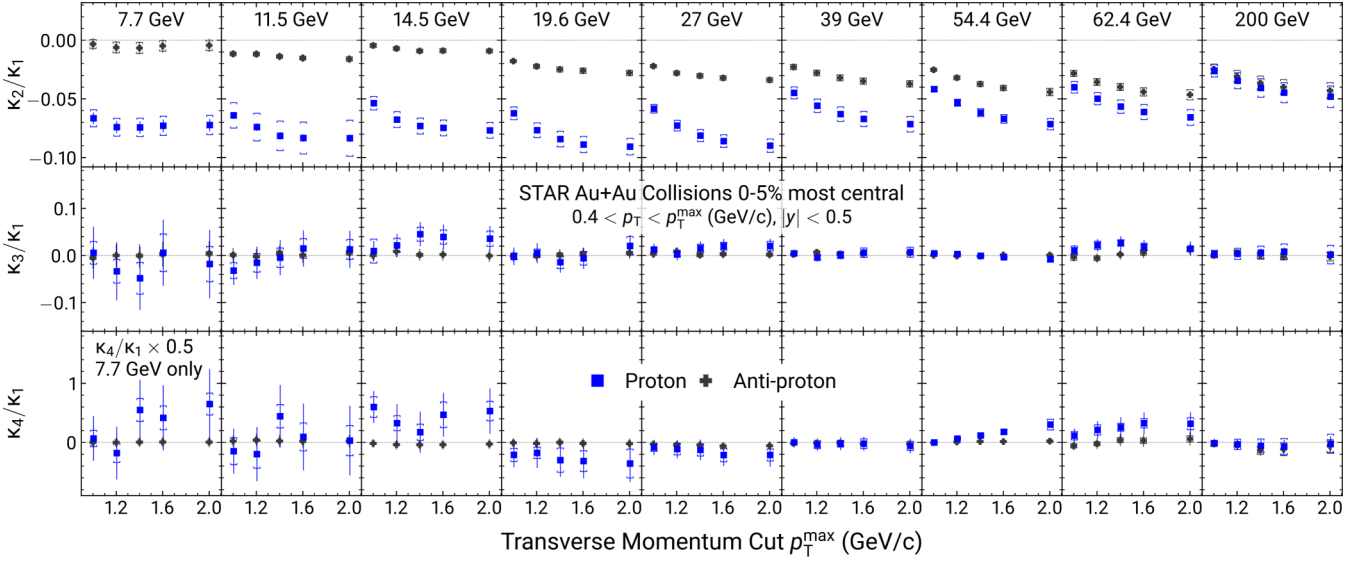


FIG. 19. The p_T -acceptance dependence of the normalized correlation functions up to fourth order (κ_n/κ_1 , $n = 2, 3, 4$) for proton and antiproton multiplicity distributions in 0–5% central Au+Au collisions at $\sqrt{s_{NN}} = 7.7, 11.5, 14.5, 19.6, 27, 39, 54.4, 62.4,$ and 200 GeV. The bars and caps represent statistical and systematic uncertainties, respectively. For clarity, the X-axis values for protons are shifted and the values of proton and antiproton κ_4/κ_1 at $\sqrt{s_{NN}} = 7.7$ GeV are scaled down by a factor of 2.

Figure 19 shows the variation of normalized correlation functions κ_n/κ_1 with p_T acceptance for protons and antiprotons at midrapidity ($|y| < 0.5$) in 0–5% central Au+Au collisions at $\sqrt{s_{NN}} = 7.7$ – 200 GeV. The κ_2/κ_1 values for protons and antiprotons are found to be negative and decrease with increasing p_T acceptance at higher $\sqrt{s_{NN}}$. The κ_2/κ_1 values for antiprotons approach zero when the beam energy is decreased, due to the small production rate of antiprotons at low energies. The negative values of κ_2/κ_1 for protons observed at low energies are mainly dominated by the baryon stopping.

Figure 20 shows the p_T acceptance dependence of C_2/C_1 , C_3/C_2 , and C_4/C_2 for proton, antiproton and net-proton distributions in 0–5% central Au+Au collisions at $\sqrt{s_{NN}} = 7.7$ – 200 GeV. In general, most of the ratios show a weak dependence on p_T acceptance for all of the $\sqrt{s_{NN}}$ studied. The C_4/C_2 ratios of proton and net-proton distributions are similar for all $\sqrt{s_{NN}}$ below 27 GeV. The C_3/C_2 ratios for protons and antiprotons are similar at higher beam energy. However, they differ from each other at the lower $\sqrt{s_{NN}}$. From the above differential measurements, it is found that the baryon number conservation strongly influences the cumulants and

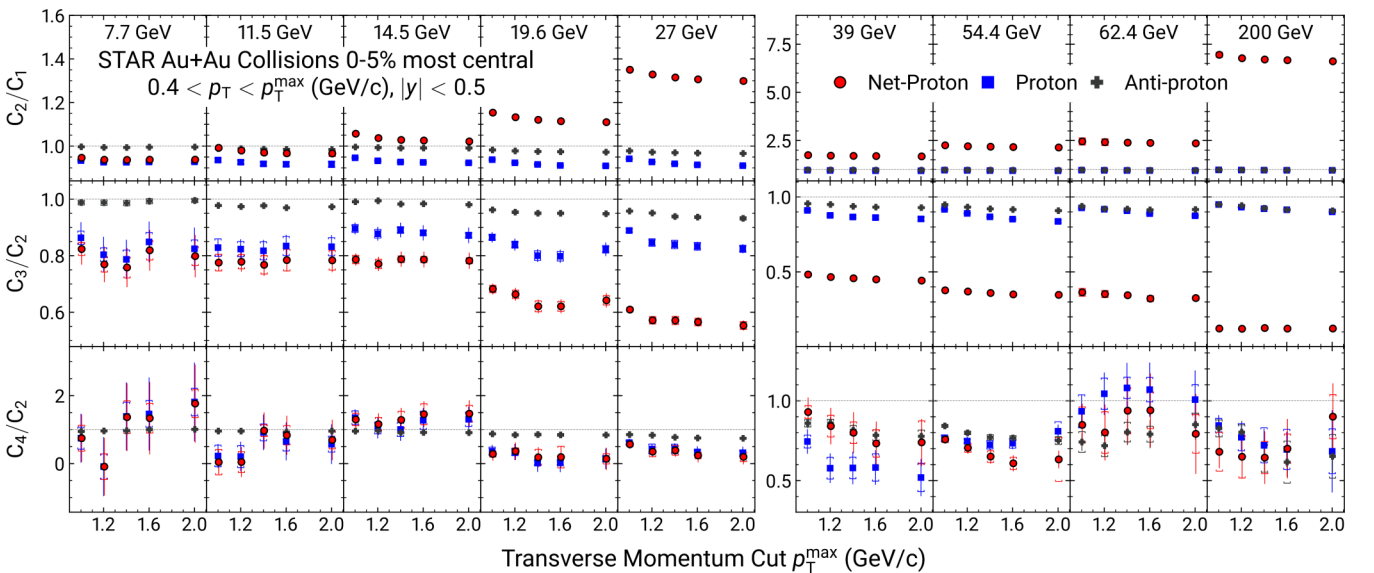


FIG. 20. p_T -acceptance dependence of cumulant ratios of proton, antiproton, and net-proton multiplicity distributions for 0–5% central Au+Au collisions at $\sqrt{s_{NN}} = 7.7, 11.5, 14.5, 19.6, 27, 39, 54.4, 62.4,$ and 200 GeV. The bars and caps represent statistical and systematic uncertainties, respectively. For clarity, the X-axis values for net protons are shifted.

correlation functions in heavy-ion collisions, especially at low energies. It could be the main reason for the negative two-particle correlation functions for protons and antiprotons [119].

C. Cumulants from models

Although our results can be compared to several models [118,130–141], we have chosen two models which do not have phase transition or critical point physics. They have contrasting physics processes to understand the following: (a) the effect of measuring net protons instead of net baryons [79,142], (b) the role of resonance decay for net-proton measurements [143–146], (c) the effect of finite p_T acceptance for the measurements [119,147], and (d) the effect of net-baryon number conservation [142,148,149]. Models without a critical point also provide an appropriate baseline for comparison to data.

1. Hadron resonance gas model

The hadron resonance gas model includes all the relevant degrees of freedom for the hadronic matter and also implicitly takes into account the interactions that are necessary for resonance formation [117,150]. Hadrons and resonances of masses up to 3 GeV/ c^2 are included. Considering a grand canonical ensemble picture, the logarithm of the partition function (Z) in the HRG model is given as

$$\ln Z(T, V, \mu) = \sum_B \ln Z_i(T, V, \mu_i) + \sum_M \ln Z_i(T, V, \mu_i), \quad (19)$$

where

$$\ln Z_i(T, V, \mu_i) = \pm \frac{V g_i}{2\pi^2} \int d^3p \ln \{1 \pm \exp[(\mu_i - E)/T]\}, \quad (20)$$

T is the temperature, V is the volume of the system, μ_i is the chemical potential, E is the energy, and g_i is the degeneracy factor of the i th particle. The total chemical potential $\mu_i = B_i\mu_B + Q_i\mu_Q + S_i\mu_S$, where B_i , Q_i , and S_i are the baryon, electric charge and strangeness number of the i th particle, with corresponding chemical potentials μ_B , μ_Q , and μ_S , respectively. The + and – signs in Eq. (20) are for baryons (B) and mesons (M), respectively. The n th-order generalized susceptibility for baryons can be expressed as [150]

$$\chi_{x,\text{baryon}}^{(n)} = \frac{x^n}{VT^3} \int d^3p \sum_{k=0}^{\infty} (-1)^k (k+1)^n \times \exp\left\{\frac{-(k+1)E}{T}\right\} \exp\left\{\frac{(k+1)\mu}{T}\right\}, \quad (21)$$

and for mesons

$$\chi_{x,\text{meson}}^{(n)} = \frac{x^n}{VT^3} \int d^3p \sum_{k=0}^{\infty} (k+1)^n \times \exp\left\{\frac{-(k+1)E}{T}\right\} \exp\left\{\frac{(k+1)\mu}{T}\right\}. \quad (22)$$

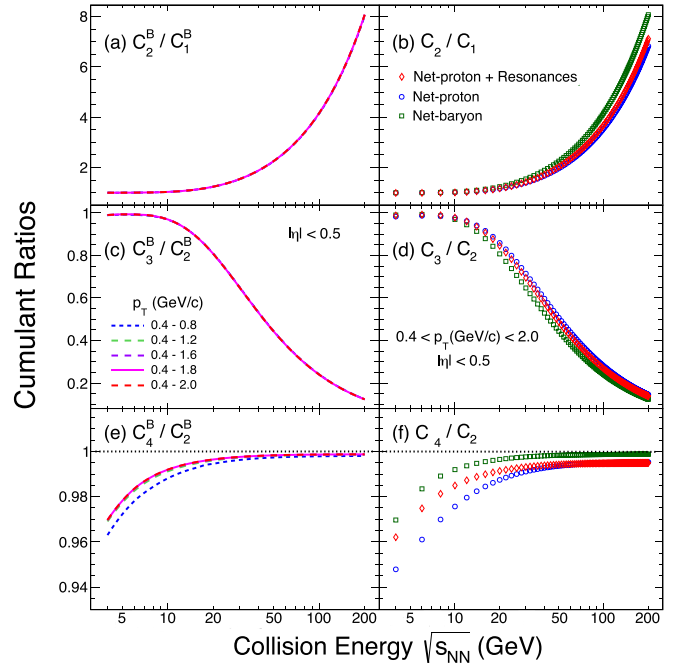


FIG. 21. Left panel: Collision energy dependence of C_2^B/C_1^B , C_3^B/C_2^B , and C_4^B/C_2^B for various p_T acceptances from the hadron resonance gas model. Right panel: The variation of net-proton and net-baryon C_2/C_1 , C_3/C_2 , and C_4/C_2 within the experimental acceptance [117]. Note: this simulation is done within a pseudorapidity window in order to make comparison between baryons of different mass.

The factor x represents either B , Q , or S of the i th particle, depending on whether the computed χ_x represents baryon, electric charge or strangeness susceptibility.

For a particle of mass m with p_T , η , and ϕ , the volume element (d^3p) and energy (E) can be written as $d^3p = p_T m_T \cosh(\eta) dp_T d\eta d\phi$ and $E = m_T \cosh \eta$, where $m_T = \sqrt{p_T^2 + m^2}$. The experimental acceptance can be incorporated by considering the appropriate integration ranges in η , p_T , ϕ , and charge states by considering the values of $|x|$. The total generalized susceptibilities will then be the sum of the contributions from baryons and mesons as in $\chi_x^{(n)} = \sum \chi_{x,\text{baryon}}^{(n)} + \sum \chi_{x,\text{meson}}^{(n)}$.

Figure 21 shows the variation of C_2^B/C_1^B , C_3^B/C_2^B , and C_4^B/C_2^B as functions of $\sqrt{s_{NN}}$ from a hadron resonance gas model [117]. The results are shown for different p_T acceptances. The differences due to acceptance are very small, and the maximum effect is at the level of 5% for $\sqrt{s_{NN}} = 7.7$ GeV for C_4^B/C_2^B . The HRG results also show that the net-proton results with resonance decays are smaller compared to net baryons and larger than net protons without the decay effect. Here also the effect is at the level of 5% for the lowest $\sqrt{s_{NN}}$ and smaller at higher energies in the case of C_4^B/C_2^B . The corresponding effect on C_3^B/C_2^B and C_2^B/C_1^B is larger at the higher energies and of the order of 17% for net protons without resonance decay and net baryons, while the effect is 10% for net protons with resonance decays and net baryons.

2. UrQMD Model

The UrQMD (ultrarelativistic quantum molecular dynamics) model [97,151] is a microscopic transport model where the phase space description of the reactions are considered. It treats the propagation of all hadrons as classical trajectories in combination with stochastic binary scattering, color string formation, and resonance decays. It incorporates baryon-baryon, meson-baryon, and meson-meson interactions. The collisional term includes more than 50 baryon species and 45 meson species. The model preserves the conservation of electric charge, baryon number, and strangeness number as expected for QCD matter. It also models the phenomenon of baryon stopping, an essential feature encountered in heavy-ion collisions at lower beam energies. In this model, the space-time evolution of the fireball is studied in terms of excitation and fragmentation of color strings and formation and decay of hadronic resonances. Since the model does not include the physics of the quark-hadron phase transition nor the QCD critical point, the comparison of the data to the results obtained from the UrQMD model will shed light on the contributions from the hadronic phase and its associated processes, baryon number conservation, and effect of measuring only net protons relative to net baryons.

In Fig. 22, the panels on the left present the energy dependence of C_n ratios of net-baryon distributions for various p_T acceptance. It is observed that the larger the p_T acceptance is, the smaller the cumulant ratios. Furthermore, with the same p_T acceptance, the values of net-baryon C_4/C_2 and C_2/C_1 ratios decrease with decreasing energies. Figure 22 right panels show the comparison of the cumulant ratios for net-baryon and net-proton distributions within the experimental acceptance for various $\sqrt{s_{NN}}$. The differences between results from different acceptance are larger for UrQMD compared to the HRG model calculations with grand canonical ensemble. In UrQMD the difference between net baryons and net protons is larger at the lower beam energies for a fixed p_T and y acceptance. The negative C_4/C_2 values of net-baryon distributions observed at low energies could be mainly due to the effect of baryon number conservation. The effects of resonance weak decay and hadronic rescattering on proton and net-proton number fluctuations in heavy-ion collisions have also been investigated in Ref. [146] within the JAM (jet AA microscopic transport) model. It is important to point out that in both the HRG model and UrQMD transport model calculations, a suppression in C_4/C_2 at low collision energy is observed, as is evident from the right plots of Fig. 21 and Fig. 22, respectively. In the case of the transport results, the suppression is attributed to the effect of baryon number conservation in strong interactions. However, the interpretation does not apply to the HRG calculation since for the grand canonical ensemble (GCE) the event-by-event conservation is absent, although, on average, the conservation law is preserved. In addition to the law of conservation, quantum effects and the change of temperature and baryon chemical potential could play a role here. It is worth noting that the energy dependence of the suppression in C_4/C_2 depends on the details of modeling, especially on proton (baryon) rapidity distributions as they directly reflect the local baryon density. This effect is

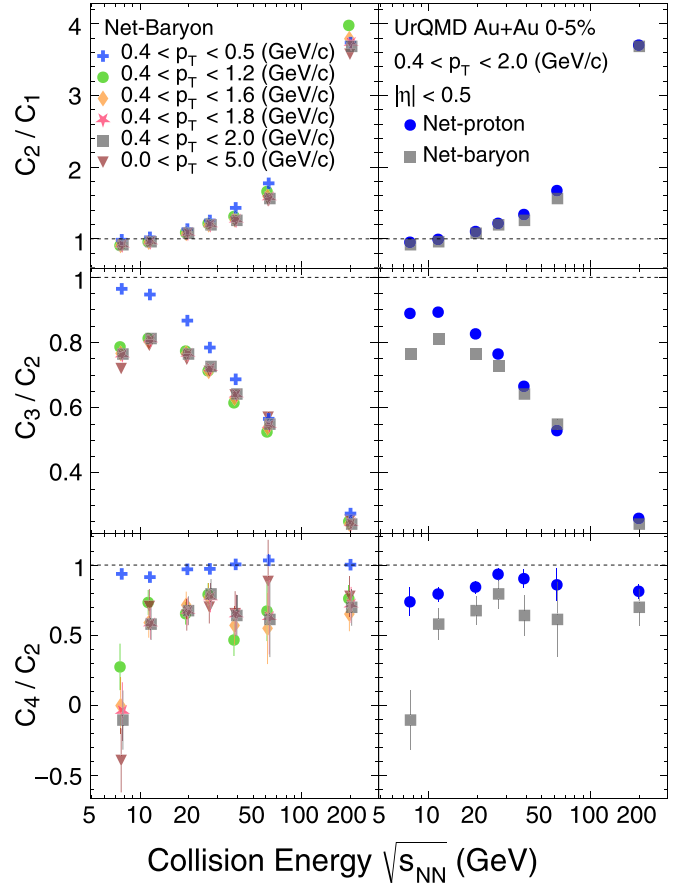


FIG. 22. Left panel: UrQMD results on p_T acceptance dependence of C_2/C_1 , C_3/C_2 , and C_4/C_2 ratios as a function of $\sqrt{s_{NN}}$ for net baryons. Right panel: Same ratios within the experimental acceptance for net protons and net baryons. Note: similar to Fig. 21, this simulation is done within a pseudorapidity window in order to make comparison between baryons of different mass.

particularly important at lower energy region due to strong stopping in such collisions. Recently, Mohs, Ryu, and Elfnr reported rather different rapidity distributions for protons in Pb+Pb collisions around SPS energies, compared to those of UrQMD calculations. This is achieved by retuning parameters in string excitation and decay in the hadronic transport model SMASH [152]. In order to establish a noncritical baseline for the critical point search, more systematic theoretical studies of the higher-order cumulant as a function of collision energy with the reliable dynamical models are called for.

3. Energy dependence

Figure 23 shows the collision-energy dependence of cumulant ratios (a) σ^2/M , (b) $S\sigma$, and (c) $\kappa\sigma^2$ of net-proton distributions for 0–5% central Au+Au collisions at $\sqrt{s_{NN}} = 7.7$ –62.4 GeV. As shown in Fig. 23, a polynomial of order 4 (5) well describes the plotted collision-energy dependence of $\kappa\sigma^2$ ($S\sigma$) of net-proton distributions for central Au+Au collisions with a $\chi^2/\text{ndf} = 1.3(0.72)$. The local derivative of the fitted polynomial function shown in the lower panel of Fig. 23 changes sign, demonstrating the nonmonotonic

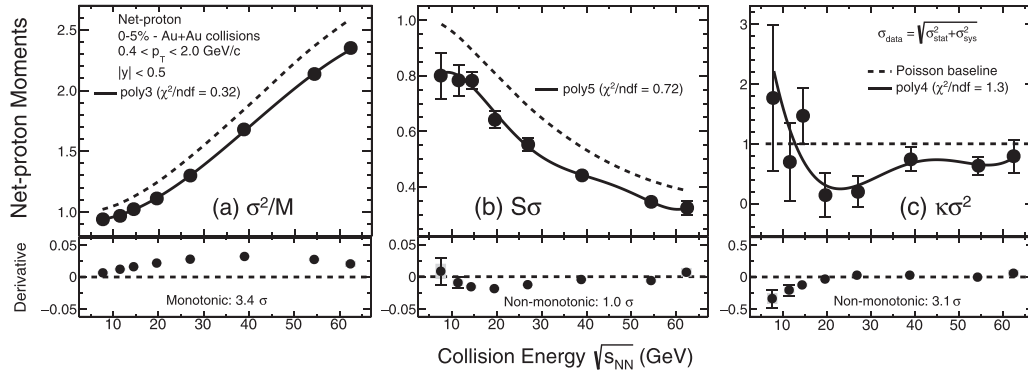


FIG. 23. Upper panel: (a) σ^2/M , (b) $S\sigma$, and (c) $\kappa\sigma^2$ of net-proton distributions for 0–5% central Au+Au collisions from $\sqrt{s_{NN}} = 7.7$ –62.4 GeV. The error bars on the data points are statistical and systematic uncertainties added in quadrature. The black solid lines are polynomial fit functions which well describe the cumulant ratios. The legends also specify the values of chi squared per degree of freedom for the respective fits. The black dashed lines are the Poisson baselines. Lower panel: Derivative of the fitted polynomial as a function of collision energy. The bar and the gold band on the derivatives represent the statistical and systematic uncertainties, respectively.

variation of the measurements with respect to collision energy. The statistical and systematic uncertainties on derivatives are obtained by randomly varying the data points at each energy within their statistical and systematic uncertainties.

The significance of the observed nonmonotonic dependence of $\kappa\sigma^2$ ($S\sigma$) on collision energy, in the energy range $\sqrt{s_{NN}} = 7.7$ –62.4 GeV, is obtained based on the fourth (fifth) order polynomial fitting procedure. This significance is evaluated by randomly varying the $\kappa\sigma^2$ and $S\sigma$ data points within their total Gaussian uncertainties (statistical and systematic uncertainties added in quadrature) at each corresponding energy. This procedure is repeated 10^6 times for $\kappa\sigma^2$ and for $S\sigma$. Out of 10^6 trials, there are 1143 cases for $\kappa\sigma^2$ and 158640 cases for $S\sigma$ where the signs of the derivative at all $\sqrt{s_{NN}}$ are found to be the same. Thus, the probability that at least one derivative at a given $\sqrt{s_{NN}}$ has a different sign from the derivatives at remaining energies among the 10^6 trials performed is 0.99886 (0.84136), which corresponds to a 3.1σ (1.0σ) effect for $\kappa\sigma^2$ ($S\sigma$). Similarly, based on the third-order polynomial fitting procedure, the cumulant ratio σ^2/M on the other hand ($\chi^2/\text{ndf} = 0.32$) exhibits a monotonic dependence on collision energy with a significance of 3.4σ . Thus we find that the cumulant ratios as a function of collision energy change from a monotonic variation to a nonmonotonic variation with $\sqrt{s_{NN}}$ as we go to higher orders. This is consistent with the QCD-based model expectation that, the higher the order of the moments is, the more sensitive it is to physics processes such as a critical point [46,75]. A test of the nonmonotonicity energy dependence with $\kappa\sigma^2$ is also carried out with the energy range $\sqrt{s_{NN}} = 7.7$ –200 GeV and the resulting significance is 3.0σ .

Figure 24 shows the collision-energy dependence of the cumulant ratios of net-proton multiplicity distributions for 0–5% central Au+Au collisions. The comparison has been made between experimental measurements and the corresponding results from the HRG and UrQMD models. We observe that both models, which do not have phase transition effects, show monotonic variations of the cumulant ratios with beam energy. However, the experimental mea-

surements of net-proton C_4/C_2 ratios show a nonmonotonic variation with $\sqrt{s_{NN}}$. On the other hand, the net-proton C_3/C_2 (C_2/C_1) in both model and data show a smooth decrease (increase) trend with increasing $\sqrt{s_{NN}}$. Although both models show a smooth energy dependence, the third-order ratios in the middle panel are larger for UrQMD than for (GCE) HRG at collision energies above 14.5 GeV. At lower energy, a suppression relative to the results of GCE HRG is observed. On the other hand, the canonical ensemble (CE) HRG, presents a consistent suppression in all three panels. In this approach, the baryon number conservation is the main source of the suppression [154,155]. It is interesting to point out that GCE models incorporating excluded volume effects (GCE E.V.) can also reproduce the suppression. The larger the repulsive volume, the stronger the suppression. Since the repulsive volume reflects the “baryon density,” the observed suppression GCE E.V. is due to the local density. For details, see Refs. [141,156,157]. To quantify the level of agreement between the experimental measurements and the model calculations, the widely used χ^2 test has been applied for two energy ranges ($\sqrt{s_{NN}} = 7.7$ –27 and 7.7–62.4 GeV). The χ^2 value is calculated as $\chi^2(R) = \sum_{\sqrt{s_{NN}}} \frac{|R_{\text{data}} - R_{\text{model}}|^2}{\text{error}^2}$, where R denotes the cumulant ratios (C_2/C_1 , C_3/C_2 , C_4/C_2) and the “error” represents the statistical and systematic uncertainties of the data and the statistical uncertainties of the model added in quadrature. In addition, the obtained χ^2 value can be converted to the corresponding right-tail p value, which is the probability of obtaining discrepancies at least as large as the results actually observed [153]. The resulting right-tail p values listed in Table VII are calculated via $p = \text{Pr}(\chi_n^2 > \chi^2)$, where χ_n^2 obeys the chi-square distribution with n independent energy data points and the χ^2 values are obtained in the chi-squared test. Usually, for the right tail p -value test, $p < 0.05$ is the commonly used standard to reject the null hypothesis and claim a significant deviation between the data and model results. It is found that the p values from the the χ^2 test are smaller than 0.05 for all of the different variants of HRG and the UrQMD model at $\sqrt{s_{NN}} = 7.7$ –27 GeV, which means the deviations between data and model results are significant

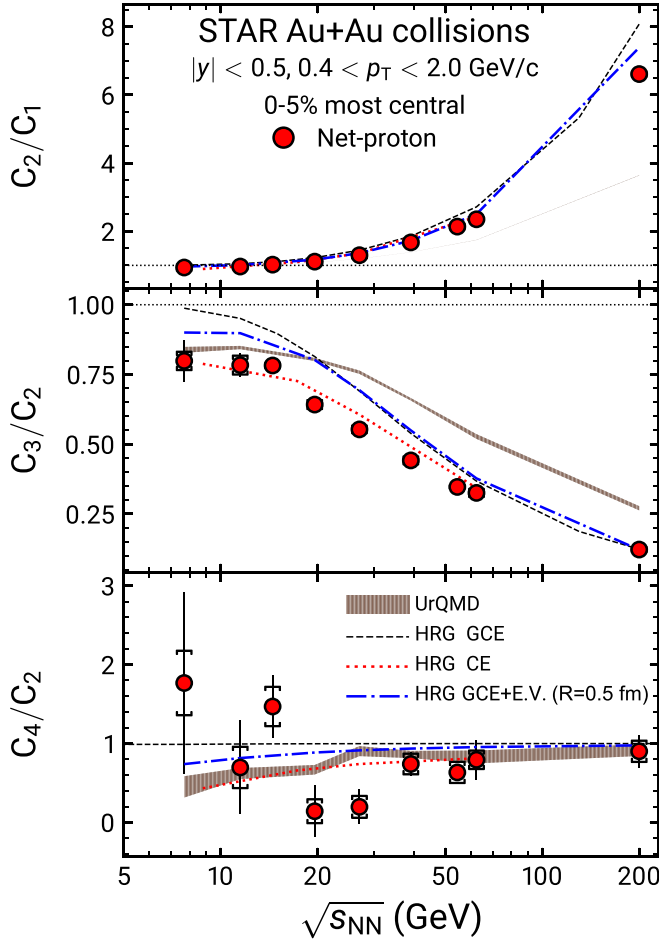


FIG. 24. Collision energy dependence of C_2/C_1 , C_3/C_2 , and C_4/C_2 for net-proton multiplicity distributions in 0–5% central Au+Au collisions. The experimental net-proton measurements are compared to corresponding values from UrQMD and HRG models within the experimental acceptances. The bars and caps represent the statistical and systematic uncertainties of the experimental data, respectively. The widths of the bands reflect the statistical uncertainties for the model calculations.

and cannot be explained by statistical fluctuations. But, for the range $\sqrt{s_{NN}} = 7.7$ –62.4 GeV, the p values of C_4/C_2 for the HRG CE and UrQMD model cases are 0.128 and 0.0577, respectively. Clearly as far as these tests are concerned, all of the above-mentioned models, showing monotonic energy dependences, do not fit the data in the most relevant energy

TABLE VII. The right-tail p values of a chi-squared test between experimental data and various models (shown in Fig. 24) for the energy dependence of the net-proton cumulant ratios in 0–5% central Au+Au collisions at two ranges of collision energy: $\sqrt{s_{NN}} = 7.7$ –27 and 7.7–62.4 GeV (the latter shown in the parentheses). Those p values denote the probability of obtaining discrepancies at least as large as the results actually observed [153]. The right-tail p values are calculated via $p = \Pr(\chi_n^2 > \chi^2)$, where χ_n^2 obeys the chi-square distribution with n independent energy data points and the χ^2 values are obtained in the chi-squared test.

Cumulant ratios	HRG GCE	HRG CE	HRG GCE+E.V. ($R = 0.5$ fm)	UrQMD
C_2/C_1	<0.001(<0.001)	<0.001(<0.001)	<0.001(<0.001)	<0.001(<0.001)
C_3/C_2	<0.001(<0.001)	0.0754 (<0.001)	<0.001(<0.001)	<0.001(<0.001)
C_4/C_2	0.00553 (0.00174)	0.0450 (0.128)	0.0145 (0.0107)	0.0221 (0.0577)

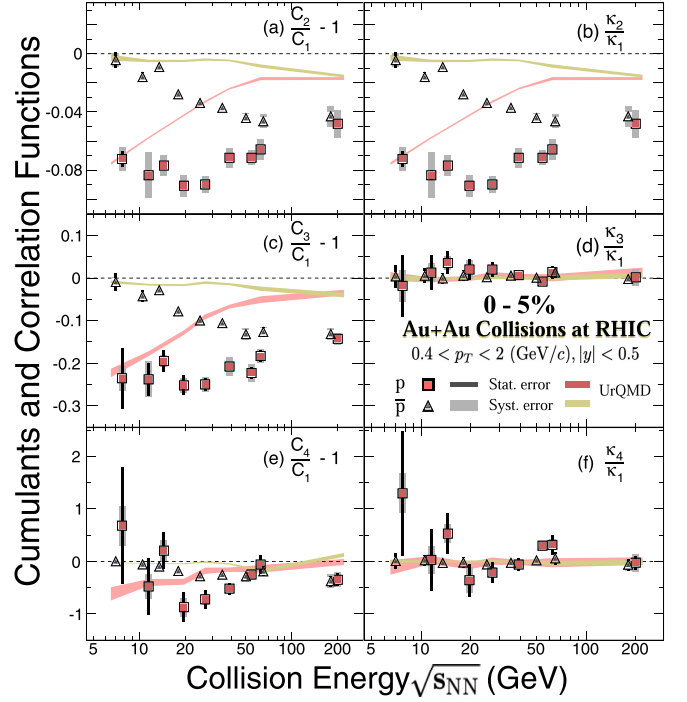


FIG. 25. Collision energy dependence of the scaled (anti)proton cumulants and correlation functions in 0–5% central Au+Au collisions at $\sqrt{s_{NN}} = 7.7, 11.5, 14.5, 19.6, 27, 39, 54.4, 62.4,$ and 200 GeV. The error bars and bands represent the statistical and systematic uncertainties, respectively. The results from UrQMD model calculation are also shown for comparison.

region, $\sqrt{s_{NN}} \leq 27$ GeV. This result will be further tested with the high-precision data from RHIC BES-II program.

Based on Eq. (7), the cumulants can be expressed in terms of the sum of various-order multiparticle correlation functions. In order to understand the contributions to the cumulants, one can present different orders of correlation functions separately. Figure 25 shows the energy dependence of the cumulants and correlation functions normalized by the mean numbers of protons and antiprotons in 0–5% central Au+Au collisions. By definition and as shown in Fig. 25, the values of $C_2/C_1 - 1$ are equal to κ_2/κ_1 . It is observed that the normalized second and third-order cumulants minus unity ($C_2/C_1 - 1$, $C_3/C_2 - 1$) are negative and show an increasing (decreasing) energy dependence in magnitude for protons (antiprotons) with decreasing collision energies. From the right panels in Fig. 25, the third-order normalized correlation

functions (κ_3/κ_1) of protons and antiprotons show flat energy dependence and are consistent with zero within uncertainties. Therefore, the energy dependence for C_3/C_1 is dominated by the negative two-particle normalized correlation functions (κ_2/κ_1), which is mainly due to the effects of baryon number conservation. The normalized four-particle correlation functions (κ_4/κ_1) of antiprotons show flat energy dependence and are consistent with zero within uncertainties. In panel (e) of Fig. 25, we observe a similar energy dependence trend for the normalized fourth-order cumulants (C_4/C_1) of protons as for the net-proton C_4/C_2 in 0–5% central Au+Au collisions shown in Fig. 24. For $\sqrt{s_{NN}} \geq 19.6$ GeV, the values of proton C_4/C_1 are dominated by the negative two-particle correlation function (κ_2) of protons (see panel (b) in Fig. 25). For $\sqrt{s_{NN}} < 19.6$ GeV, the four-particle correlation function (κ_4) of protons plays a role in determining the energy dependence of proton C_4/C_1 , which cannot be solely understood by the suppression effects due to negative values of κ_2 for protons. As discussed in Refs. [98,158], the observed large values of the four-particle correlation function of protons (κ_4) could be attributed to the formation of proton cluster and related to the signature of a critical point or a first order phase transition. Therefore, it is necessary to perform precise measurements of the κ_4/κ_1 of protons below 19.6 GeV with high statistics data taken in the second phase of the beam energy scan at RHIC. In addition, we compare the experimental data in Fig. 25 with UrQMD model calculations. The energy dependence of the second- and third-order normalized cumulants and correlation functions can be qualitatively described by the UrQMD model. However, the nonmonotonic energy dependence observed in the proton C_4/C_1 cannot be described by the UrQMD model. Furthermore, the three- and four-particle correlation functions (κ_3 and κ_4) for (anti)protons from UrQMD show flat energy dependence and are consistent with zero. This indicates that the higher-order (anti)proton correlation functions κ_3 and κ_4 are not sensitive to the effect of baryon number conservation within the current acceptance, and therefore can serve as good probes of critical fluctuations in heavy-ion collisions [119,146].

IV. SUMMARY AND OUTLOOK

In summary, we report a systematic study of the cumulants of the net-proton, proton, and antiproton multiplicity distributions from Au+Au collisions at $\sqrt{s_{NN}} = 7.7$ –200 GeV. The data have been collected with the STAR experiment in the first phase of the RHIC beam energy scan acquired over the period of 2010–2017. The energy, centrality, and acceptance dependence of the correlation functions of protons and antiprotons are presented in this paper. Both cumulants and correlation functions up to fourth order at midrapidity ($|\eta| < 0.5$) within $0.4 < p_T < 2.0$ GeV/c in Au+Au collisions are presented to search for the signatures of a critical point and/or a first-order phase transition over a broad region of baryon chemical potential.

The protons and antiprotons are identified with greater than 97% purity using the TPC and TOF detectors of STAR. The centrality selection is based on midrapidity pions and kaons only to avoid self-correlation effects. The maximum-allowed rapidity acceptance around midrapidity has been used for

centrality determination to minimize the effect of centrality resolution. The variation of the average number of protons and antiprotons in a given centrality bin has been accounted for by applying a centrality bin-width correction, which also minimizes volume fluctuation effects. The cumulants are corrected for the proton and antiproton reconstruction efficiencies using a binomial response function. Study of the unfolding technique for efficiency correction of cumulants has shown that, even in the 0–5% central Au+Au collisions at $\sqrt{s_{NN}} = 200$ GeV, the case with the highest multiplicity, the results are consistent with the commonly-used binomial approach within current statistical uncertainties. The statistical errors on the cumulants are based on the delta theorem method and are shown to be consistent with those obtained by the bootstrap method. A detailed estimate of the systematic uncertainties is also presented. Results on cumulant ratios from different variants of the HRG and the UrQMD models are presented to understand the effects of experimental acceptance, resonance decay, baryon number conservation, and net-proton versus net-baryon analysis. The cumulant ratios show a centrality and energy dependence, which are reproduced neither by purely hadronic-transport-based UrQMD model calculations nor by different variants of the hadron resonance gas model. Specifically, the net-proton C_4/C_2 ratio for 0–5% central Au+Au collisions shows a nonmonotonic variation with $\sqrt{s_{NN}}$, with a significance of 3.1σ . This is consistent with the expectations of critical fluctuations in a QCD-inspired model. A χ^2 test has been applied to quantify the level of agreement between experimental data and model calculations. The resulting p values suggest that the models fail to explain the 0–5% Au+Au collision data at $\sqrt{s_{NN}} \leq 27$ GeV. The y and p_T acceptance dependence of the cumulants and their ratios provide valuable data to understand the range of the correlations and their relation to the acceptance of the detector [98,125]. Furthermore, the systematic analysis presented here can be used to constrain the freeze-out conditions in high-energy heavy-ion collisions using QCD-based approaches, and to understand the nature of thermalization in such collisions [121–123]. From the analysis of multiparticle correlation functions, one observes significant negative values for κ_2 of protons and antiprotons, which are mainly due to the effects of baryon number conservation in heavy-ion collisions. The values of κ_3 of protons and antiprotons are consistent with zero for all of the collision energies studied. Further, the energy dependence trend of proton C_4/C_1 below 19.6 GeV cannot be solely understood by the negative values of κ_2 for protons, and the four-particle correlation function of protons (κ_4) is found to play a role, which needs to be confirmed with the high statistics data taken in RHIC BES-II, which began data-taking in 2018. Upgrades to the STAR detector system have significantly improved the quality of the measurements [2]. Primarily the goal of BES-II is to make high-statistics measurements, with extended kinematic range in rapidity and transverse momentum for the measurements discussed in this paper. The extended kinematic range in rapidity and transverse momentum are brought about by upgrading the inner TPC (iTPC) to extend the measurement coverage to $|\eta| < 1.5$, the p_T acceptance down to 100 MeV/c and improved dE/dx resolution. Particle identification capability will be extended to $-1.6 < \eta < 1.0$ with the addition of

TABLE VIII. Total number of collected/expected events in BES Phase II for various collision energies ($\sqrt{s_{NN}}$) [2].

$\sqrt{s_{NN}}$ (GeV)	Year	No. of events ($\times 10^6$)
27	2018	500
19.6	2019	400
17.3	2021	250
14.5	2019	300
11.5	2020	230
9.2	2020	160
7.7	2021	100

an endcap TOF (eTOF) detector. The collected event statistics to date, along with the goal for 2021, are listed in Table VIII.

At the same time, STAR will take data in fixed-target mode to extend $\sqrt{s_{NN}}$ to 3 GeV. With these upgrades, and with the benefits of extended kinematic coverage and the use of sensitive observables, the RHIC BES Phase-II program will allow measurements of unprecedented precision for exploring the QCD phase structure within $200 < \mu_B < 720$ MeV.

ACKNOWLEDGMENTS

We thank H. Elfner, S. Gupta, F. Karsch, M. Kitazawa, V. Koch, D. Mishra, J. M. Pawłowski, K. Rajagopal, K. Redlich, and M. Stephanov for stimulating discussions related to this work. We thank the RHIC Operations Group and RCF at BNL, the NERSC Center at LBNL, and the Open Science Grid consortium for providing resources and support. This

work was supported in part by the Office of Nuclear Physics within the U.S. DOE Office of Science, the U.S. National Science Foundation, the Ministry of Education and Science of the Russian Federation, National Natural Science Foundation of China, Chinese Academy of Science, the Ministry of Science and Technology of China and the Chinese Ministry of Education, the Higher Education Sprout Project by Ministry of Education at NCKU, the National Research Foundation of Korea, Czech Science Foundation and Ministry of Education, Youth and Sports of the Czech Republic, Hungarian National Research, Development and Innovation Office, New National Excellency Programme of the Hungarian Ministry of Human Capacities, Department of Atomic Energy and Department of Science and Technology of the Government of India, the National Science Centre of Poland, the Ministry of Science, Education and Sports of the Republic of Croatia, RosAtom of Russia, German Bundesministerium für Bildung, Wissenschaft, Forschung und Technologie (BMBF), Helmholtz Association, Ministry of Education, Culture, Sports, Science, and Technology (MEXT), and Japan Society for the Promotion of Science (JSPS).

APPENDIX A: EFFICIENCY CORRECTION

In order to correct the C_n for efficiency effects, one has to invoke a model assumption for the response of the detector. The detector response is assumed to follow a binomial probability distribution function. The probability distribution function of measured proton number n_p and antiproton number $n_{\bar{p}}$ can be expressed as [80,104]

$$p(n_p, n_{\bar{p}}) = \sum_{N_p=n_p}^{\infty} \sum_{N_{\bar{p}}=n_{\bar{p}}}^{\infty} P(N_p, N_{\bar{p}}) \times \frac{N_p!}{n_p!(N_p - n_p)!} (\varepsilon_p)^{n_p} (1 - \varepsilon_p)^{N_p - n_p} \frac{N_{\bar{p}}!}{n_{\bar{p}}!(N_{\bar{p}} - n_{\bar{p}})!} (\varepsilon_{\bar{p}})^{n_{\bar{p}}} (1 - \varepsilon_{\bar{p}})^{N_{\bar{p}} - n_{\bar{p}}}, \quad (\text{A1})$$

where the $P(N_p, N_{\bar{p}})$ is the original joint probability distribution of numbers of protons (N_p) and antiprotons ($N_{\bar{p}}$), and $\varepsilon_p, \varepsilon_{\bar{p}}$ are the efficiency of reconstructing the protons and antiprotons, respectively. In order to arrive at an expression for efficiency-corrected cumulants or moments, the bivariate factorial moments are first defined as

$$F_{i,k}(N_p, N_{\bar{p}}) = \left\langle \frac{N_p!}{(N_p - i)!} \frac{N_{\bar{p}}!}{(N_{\bar{p}} - k)!} \right\rangle = \sum_{N_p=i}^{\infty} \sum_{N_{\bar{p}}=k}^{\infty} P(N_p, N_{\bar{p}}) \frac{N_p!}{(N_p - i)!} \frac{N_{\bar{p}}!}{(N_{\bar{p}} - k)!}, \quad (\text{A2})$$

$$f_{i,k}(n_p, n_{\bar{p}}) = \left\langle \frac{n_p!}{(n_p - i)!} \frac{n_{\bar{p}}!}{(n_{\bar{p}} - k)!} \right\rangle = \sum_{n_p=i}^{\infty} \sum_{n_{\bar{p}}=k}^{\infty} p(n_p, n_{\bar{p}}) \frac{n_p!}{(n_p - i)!} \frac{n_{\bar{p}}!}{(n_{\bar{p}} - k)!}. \quad (\text{A3})$$

The efficiency-corrected factorial moments are then given as

$$F_{i,k}(N_p, N_{\bar{p}}) = \frac{f_{i,k}(n_p, n_{\bar{p}})}{(\varepsilon_p)^i (\varepsilon_{\bar{p}})^k}. \quad (\text{A4})$$

Then the n th-order efficiency-corrected moments of net-proton distributions are related to the efficiency-corrected factorial moments as

$$\begin{aligned} m_n(N_p - N_{\bar{p}}) &= \langle (N_p - N_{\bar{p}})^n \rangle = \sum_{i=0}^n (-1)^i \binom{n}{i} \langle N_p^{n-i} N_{\bar{p}}^i \rangle \\ &= \sum_{i=0}^n (-1)^i \binom{n}{i} \left[\sum_{r_1=0}^{n-i} \sum_{r_2=0}^i s_2(n-i, r_1) s_2(i, r_2) F_{r_1, r_2}(N_p, N_{\bar{p}}) \right] \\ &= \sum_{i=0}^n \sum_{r_1=0}^{n-i} \sum_{r_2=0}^i (-1)^i \binom{n}{i} s_2(n-i, r_1) s_2(i, r_2) F_{r_1, r_2}(N_p, N_{\bar{p}}). \end{aligned} \quad (\text{A5})$$

The Stirling numbers of the first $[s_1(n, i)]$ and second kind $[s_2(n, i)]$ are defined as

$$\frac{N!}{(N-n)!} = \sum_{i=0}^n s_1(n, i) N^i, \quad (\text{A6})$$

$$N^n = \sum_{i=0}^n s_2(n, i) \frac{N!}{(N-i)!}, \quad (\text{A7})$$

where N , n , and i are non-negative integer numbers. The efficiency-corrected cumulants of net-proton distributions can be obtained from the efficiency-corrected moments by using the recursion relation

$$C_r(N_p - N_{\bar{p}}) = m_r(N_p - N_{\bar{p}}) - \sum_{s=1}^{r-1} \binom{r-1}{s-1} C_s(N_p - N_{\bar{p}}) m_{r-s}(N_p - N_{\bar{p}}), \quad (\text{A8})$$

where the C_r denotes the r th-order cumulants of net-proton distributions.

If the protons and antiprotons have the same efficiency, $\varepsilon_p = \varepsilon_{\bar{p}} = \varepsilon$, the expressions for the first four efficiency-corrected cumulants can be explicitly written as

$$\begin{aligned} C_1^{X-Y} &= \frac{\langle X \rangle - \langle Y \rangle}{\varepsilon}, \\ C_2^{X-Y} &= \frac{C_2^{X-Y} + (\varepsilon - 1)(\langle X \rangle + \langle Y \rangle)}{\varepsilon^2}, \\ C_3^{X-Y} &= \frac{C_3^{X-Y} + 3(\varepsilon - 1)(C_2^X - C_2^Y) + (\varepsilon - 1)(\varepsilon - 2)(\langle X \rangle - \langle Y \rangle)}{\varepsilon^3}, \\ C_4^{X-Y} &= \frac{C_4^{X-Y} - 2(\varepsilon - 1)C_3^{X+Y} + 8(\varepsilon - 1)(C_3^X + C_3^Y) + (5 - \varepsilon)(\varepsilon - 1)C_2^{X+Y}}{\varepsilon^4} \\ &\quad + \frac{8(\varepsilon - 1)(\varepsilon - 2)(C_2^X + C_2^Y) + (\varepsilon^2 - 6\varepsilon + 6)(\varepsilon - 1)(\langle X \rangle + \langle Y \rangle)}{\varepsilon^4}, \end{aligned} \quad (\text{A9})$$

where the (X, Y) and (x, y) are the numbers of (p, \bar{p}) produced and measured, respectively. The efficiency-corrected cumulants are sensitive to the efficiency and depend on the lower order measured cumulants.

In the current analysis, the proton and antiproton p_T range is from 0.4 to 2 GeV/ c . This has been possible by using particle identification information for the TPC in the p_T range 0.4 to 0.8 GeV/ c and the TPC+TOF in the momentum range 0.8 to 2 GeV/ c . This results in two different efficiencies for proton reconstruction and two different values for antiprotons.

Hence the above formulation which holds for one single value of efficiency and $\varepsilon = \varepsilon_p = \varepsilon_{\bar{p}}$ has to be modified to take care of four different efficiency values, two each for the proton and antiproton corresponding to different p_T ranges. Let $\varepsilon_{p_1}, \varepsilon_{p_2}$ and $\varepsilon_{\bar{p}_1}, \varepsilon_{\bar{p}_2}$ denote the efficiency for protons and antiprotons in the two subphase spaces, and denote the corresponding numbers of protons and antiprotons in the two subphase spaces by N_{p_1}, N_{p_2} and $N_{\bar{p}_1}, N_{\bar{p}_2}$, respectively. Using analogous formulations as above, the bivariate factorial moments of protons and antiprotons distributions are given as

$$\begin{aligned} F_{r_1, r_2}(N_p, N_{\bar{p}}) &= F_{r_1, r_2}(N_{p_1} + N_{p_2}, N_{\bar{p}_1} + N_{\bar{p}_2}) = \sum_{i_1=0}^{r_1} \sum_{i_2=0}^{r_2} s_1(r_1, i_1) s_1(r_2, i_2) \langle (N_{p_1} + N_{p_2})^{i_1} (N_{\bar{p}_1} + N_{\bar{p}_2})^{i_2} \rangle \\ &= \sum_{i_1=0}^{r_1} \sum_{i_2=0}^{r_2} s_1(r_1, i_1) s_1(r_2, i_2) \left\langle \sum_{s=0}^{i_1} \binom{i_1}{s} N_{p_1}^{i_1-s} N_{p_2}^s \sum_{t=0}^{i_2} \binom{i_2}{t} N_{\bar{p}_1}^{i_2-t} N_{\bar{p}_2}^t \right\rangle \\ &= \sum_{i_1=0}^{r_1} \sum_{i_2=0}^{r_2} \sum_{s=0}^{i_1} \sum_{t=0}^{i_2} s_1(r_1, i_1) s_1(r_2, i_2) \binom{i_1}{s} \binom{i_2}{t} \langle N_{p_1}^{i_1-s} N_{p_2}^s N_{\bar{p}_1}^{i_2-t} N_{\bar{p}_2}^t \rangle \\ &= \sum_{i_1=0}^{r_1} \sum_{i_2=0}^{r_2} \sum_{s=0}^{i_1} \sum_{t=0}^{i_2} \sum_{u=0}^{i_1-s} \sum_{v=0}^s \sum_{j=0}^{i_2-t} \sum_{k=0}^t s_1(r_1, i_1) s_1(r_2, i_2) \binom{i_1}{s} \binom{i_2}{t} \\ &\quad \times s_2(i_1 - s, u) s_2(s, v) s_2(i_2 - t, j) s_2(t, k) \times F_{u, v, j, k}(N_{p_1}, N_{p_2}, N_{\bar{p}_1}, N_{\bar{p}_2}). \end{aligned} \quad (\text{A10})$$

Similarly to Eq. (A4) for the multivariate case, the efficiency-corrected multivariate factorial moments of proton and antiproton distributions in the current case are given as

$$F_{u,v,j,k}(N_{p_1}, N_{p_2}, N_{\bar{p}_1}, N_{\bar{p}_2}) = \frac{f_{u,v,j,k}(n_{p_1}, n_{p_2}, n_{\bar{p}_1}, n_{\bar{p}_2})}{(\varepsilon_{p_1})^u (\varepsilon_{p_2})^v (\varepsilon_{\bar{p}_1})^j (\varepsilon_{\bar{p}_2})^k}, \quad (\text{A11})$$

where $f_{u,v,j,k}(N_{p_1}, N_{p_2}, N_{\bar{p}_1}, N_{\bar{p}_2})$ are the measured multivariate factorial moments of proton and antiproton distributions. By using Eqs. (A5), (A8), (A10), and (A11), one can obtain the efficiency-corrected moments and cumulants of net-proton distributions for the case where the protons (antiprotons) have different efficiencies in two subphase spaces. Through simulations as discussed in Refs. [104,159], it has been shown that this formulation works consistently. Another binomial-model-based efficiency correction

method using track-by-track efficiency is discussed in Ref. [106].

APPENDIX B: STATISTICAL UNCERTAINTIES ESTIMATION

According to Eqs. (A5), (A8), and (A10), the efficiency-corrected moments are expressed in terms of the factorial moments, and thereby the factorial moments are the random variable X_i in Eq. (15). The covariance of the multivariate moments can be written as

$$\text{Cov}(m_{r,s}, m_{u,v}) = \frac{1}{n} (m_{r+u,s+v} - m_{r,s} m_{u,v}) \quad (\text{B1})$$

where n is the number of events, $m_{r,s} = \langle X_1^r X_2^s \rangle$ and $m_{u,v} = \langle X_1^u X_2^v \rangle$ are the multivariate moments, and the X_1 and X_2 are random variables. In this paper, X_1 and X_2 represent proton and antiproton numbers, respectively. Based on Eq. (B1), one can obtain the covariance for the multivariate factorial moments as

$$\begin{aligned} \text{Cov}(f_{r,s}, f_{u,v}) &= \text{Cov} \left(\sum_{i=0}^r \sum_{j=0}^s s_1(r, i) s_1(s, j) m_{i,j}, \sum_{k=0}^u \sum_{h=0}^v s_1(u, k) s_1(v, h) m_{k,h} \right) \\ &= \sum_{i=0}^r \sum_{j=0}^s \sum_{k=0}^u \sum_{h=0}^v s_1(r, i) s_1(s, j) s_1(u, k) s_1(v, h) \times \text{Cov}(m_{i,j}, m_{k,h}) \\ &= \frac{1}{n} \sum_{i=0}^r \sum_{j=0}^s \sum_{k=0}^u \sum_{h=0}^v s_1(r, i) s_1(s, j) s_1(u, k) s_1(v, h) \times (m_{i+k, j+h} - m_{i,j} m_{k,h}) \\ &= \frac{1}{n} (f_{(r,u),(s,v)} - f_{r,s} f_{u,v}), \end{aligned} \quad (\text{B2})$$

where the $f_{(r,u),(s,v)}$ is defined as

$$\begin{aligned} f_{(r,u),(s,v)} &= \left\langle \frac{X_1!}{(X_1 - r)!} \frac{X_1!}{(X_1 - u)!} \frac{X_2!}{(X_2 - s)!} \frac{X_2!}{(X_2 - v)!} \right\rangle \\ &= \sum_{i=0}^r \sum_{j=0}^s \sum_{k=0}^u \sum_{h=0}^v \sum_{\alpha=0}^{i+k} \sum_{\beta=0}^{j+h} s_1(r, i) s_1(s, j) s_1(u, k) s_1(v, h) s_2(i+k, \alpha) s_2(j+h, \beta) f_{\alpha, \beta}. \end{aligned} \quad (\text{B3})$$

The definition of the bivariate factorial moments $f_{r,s}$, $f_{u,v}$, and $f_{\alpha, \beta}$ can be found in Eq. (A3). Equation (B2) can be used in the standard error propagation formula, Eq. (15), to obtain the statistical uncertainties of the efficiency-corrected cumulants. The detailed derivation of the analytical formulae for statistical uncertainties on cumulants and moments exists in the literature [104,113]. If we put $\varepsilon_p = \varepsilon_{\bar{p}} = 1$, the statistical uncertainties on the cumulants and cumulant ratios up to the eighth order expressed in terms of central moments (μ_n) are given below, where the uncertainties are the square roots of the variances:

$$\text{Var}(C_1) = \mu_2/n,$$

$$\text{Var}(C_2) = (-\mu_2^2 + \mu_4)/n,$$

$$\text{Var}(C_3) = (9\mu_2^3 - 6\mu_2\mu_4 - \mu_3^2 + \mu_6)/n,$$

$$\text{Var}(C_4) = (-36\mu_2^4 + 48\mu_2^2\mu_4 + 64\mu_2\mu_3^2 - 12\mu_2\mu_6 - 8\mu_3\mu_5 - \mu_4^2 + \mu_8)/n,$$

$$\begin{aligned} \text{Var}(C_5) &= (\mu_{10} + 900\mu_2^5 - 900\mu_2^3\mu_4 - 1000\mu_2^2\mu_3^2 + 160\mu_2^2\mu_6 + 240\mu_2\mu_3\mu_5 \\ &\quad + 125\mu_2\mu_4^2 - 20\mu_2\mu_8 + 200\mu_3^2\mu_4 - 20\mu_3\mu_7 - 10\mu_4\mu_6 - \mu_5^2)/n, \end{aligned}$$

$$\begin{aligned} \text{Var}(C_6) &= (-30\mu_{10}\mu_2 + \mu_{12} - 8100\mu_2^6 + 13500\mu_2^4\mu_4 + 39600\mu_2^3\mu_3^2 - 2880\mu_2^3\mu_6 \\ &\quad - 9720\mu_2^2\mu_3\mu_5 - 3600\mu_2^2\mu_4^2 + 405\mu_2^2\mu_8 - 9600\mu_2\mu_3^2\mu_4 + 840\mu_2\mu_3\mu_7 - 400\mu_4^4) \end{aligned}$$

$$+ 216\mu_2\mu_5^2 + 510\mu_2\mu_4\mu_6 + 440\mu_3^2\mu_6 + 1020\mu_3\mu_4\mu_5 - 40\mu_3\mu_9 + 225\mu_4^3 \\ - 30\mu_4\mu_8 - 12\mu_5\mu_7 - \mu_6^2)/n,$$

$$\text{Var}(C_7) = (861\mu_{10}\mu_2^2 - 70\mu_{10}\mu_4 - 70\mu_{11}\mu_3 - 42\mu_{12}\mu_2 + \mu_{14} + 396900\mu_2^7 - 529200\mu_2^5\mu_4 \\ - 1102500\mu_2^4\mu_3^2 + 79380\mu_2^4\mu_6 + 299880\mu_2^3\mu_3\mu_5 + 176400\mu_2^3\mu_4^2 - 10080\mu_2^3\mu_8 + 558600\mu_2^2\mu_3\mu_4 \\ - 33600\mu_2^2\mu_3\mu_7 - 29400\mu_2^2\mu_4\mu_6 - 10584\mu_2^2\mu_5^2 + 137200\mu_2\mu_3^4 - 43120\mu_2\mu_3^2\mu_6 \\ - 76440\mu_2\mu_3\mu_4\mu_5 + 2310\mu_2\mu_3\mu_9 - 14700\mu_2\mu_4^3 + 1890\mu_2\mu_4\mu_8 \\ + 966\mu_2\mu_5\mu_7 + 343\mu_2\mu_6^2 - 15680\mu_3^3\mu_5 - 14700\mu_3^2\mu_4^2 + 1505\mu_3^2\mu_8 + 2590\mu_3\mu_4\mu_7 \\ + 2254\mu_3\mu_5\mu_6 + 1715\mu_4^2\mu_6 + 1911\mu_4\mu_5^2 - 42\mu_5\mu_9 - 14\mu_6\mu_8 - \mu_7^2)/n,$$

$$\text{Var}(C_8) = (-28560\mu_{10}\mu_2^3 + 5600\mu_{10}\mu_2\mu_4 + 4256\mu_{10}\mu_3^2 - 56\mu_{10}\mu_6 + 5376\mu_{11}\mu_2\mu_3 - 112\mu_{11}\mu_5 \\ + 1624\mu_{12}\mu_2^2 - 140\mu_{12}\mu_4 - 112\mu_{13}\mu_3 - 56\mu_{14}\mu_2 + \mu_{16} - 6350400\mu_2^8 + 12700800\mu_2^6\mu_4 \\ + 59270400\mu_2^5\mu_3^2 - 2399040\mu_2^5\mu_6 - 15523200\mu_2^4\mu_3\mu_5 - 6174000\mu_2^4\mu_4^2 + 322560\mu_2^4\mu_8 \\ - 35280000\mu_2^3\mu_3^2\mu_4 + 1626240\mu_2^3\mu_3\mu_7 + 1340640\mu_2^3\mu_4\mu_6 + 677376\mu_2^3\mu_5^2 - 8467200\mu_2^2\mu_3^4 \\ + 2759680\mu_2^2\mu_3^2\mu_6 + 5597760\mu_2^2\mu_3\mu_4\mu_5 - 119840\mu_2^2\mu_3\mu_9 + 882000\mu_2^2\mu_4^3 - 108360\mu_2^2\mu_4\mu_8 \\ - 77952\mu_2^2\mu_5\mu_7 - 26656\mu_2^2\mu_6^2 + 2007040\mu_2\mu_3^3\mu_5 + 3684800\mu_2\mu_3^2\mu_4^2 - 160160\mu_2\mu_3^2\mu_8 \\ - 322560\mu_2\mu_3\mu_4\mu_7 - 257152\mu_2\mu_3\mu_5\mu_6 - 172480\mu_2\mu_4^2\mu_6 - 178752\mu_2\mu_4\mu_5^2 + 3808\mu_2\mu_5\mu_9 \\ + 1680\mu_2\mu_6\mu_8 + 512\mu_2\mu_7^2 + 940800\mu_3^4\mu_4 - 71680\mu_3^3\mu_7 - 203840\mu_3^2\mu_4\mu_6 - 75264\mu_3^2\mu_5^2 \\ - 156800\mu_3\mu_4^2\mu_5 + 8960\mu_3\mu_4\mu_9 + 6496\mu_3\mu_5\mu_8 + 4480\mu_3\mu_6\mu_7 - 4900\mu_4^4 + 5040\mu_4^2\mu_8 \\ + 9856\mu_4\mu_5\mu_7 + 4704\mu_4\mu_6^2 + 6272\mu_5^2\mu_6 - 16\mu_7\mu_9 - \mu_8^2)/n,$$

$$\text{Var}\left(\frac{C_2}{C_1}\right) = \left(-\frac{\mu_2^2}{\langle N \rangle^2} + \frac{\mu_4}{\langle N \rangle^2} - \frac{2\mu_2\mu_3}{\langle N \rangle^3} + \frac{\mu_2^3}{\langle N \rangle^4}\right) / n,$$

$$\text{Var}\left(\frac{C_3}{C_2}\right) = \left(9\mu_2 - \frac{6\mu_4}{\mu_2} + \frac{6\mu_3^2}{\mu_2^2} + \frac{\mu_6}{\mu_2^2} - \frac{2\mu_3\mu_5}{\mu_2^3} + \frac{\mu_2^2\mu_4}{\mu_2^4}\right) / n,$$

$$\text{Var}\left(\frac{C_4}{C_2}\right) = \left(-9\mu_2^2 + 9\mu_4 + \frac{40\mu_3^2}{\mu_2} - \frac{6\mu_6}{\mu_2} - \frac{8\mu_3\mu_5}{\mu_2^2} + \frac{6\mu_4^2}{\mu_2^2} + \frac{\mu_8}{\mu_2^2} + \frac{8\mu_3^2\mu_4}{\mu_2^3} - \frac{2\mu_4\mu_6}{\mu_2^3} + \frac{\mu_4^3}{\mu_2^4}\right) / n,$$

$$\text{Var}\left(\frac{C_5}{C_1}\right) = \left(\frac{\mu_{10}}{\langle N \rangle^2} + \frac{900\mu_2^5}{\langle N \rangle^2} - \frac{900\mu_2^3\mu_4}{\langle N \rangle^2} - \frac{1000\mu_2^2\mu_3^2}{\langle N \rangle^2} + \frac{160\mu_2^2\mu_6}{\langle N \rangle^2} + \frac{240\mu_2\mu_3\mu_5}{\langle N \rangle^2} + \frac{125\mu_2\mu_4^2}{\langle N \rangle^2} \right. \\ \left. - \frac{20\mu_2\mu_8}{\langle N \rangle^2} + \frac{200\mu_3^2\mu_4}{\langle N \rangle^2} - \frac{20\mu_3\mu_7}{\langle N \rangle^2} - \frac{10\mu_4\mu_6}{\langle N \rangle^2} - \frac{\mu_5^2}{\langle N \rangle^2} + \frac{600\mu_2^4\mu_3}{\langle N \rangle^3} - \frac{60\mu_2^3\mu_5}{\langle N \rangle^3} - \frac{300\mu_2^2\mu_3\mu_4}{\langle N \rangle^3} \right. \\ \left. - \frac{200\mu_2\mu_3^3}{\langle N \rangle^3} + \frac{20\mu_2\mu_3\mu_6}{\langle N \rangle^3} + \frac{30\mu_2\mu_4\mu_5}{\langle N \rangle^3} + \frac{20\mu_3^2\mu_5}{\langle N \rangle^3} - \frac{2\mu_5\mu_6}{\langle N \rangle^3} + \frac{100\mu_2^3\mu_3^2}{\langle N \rangle^4} - \frac{20\mu_2^2\mu_3\mu_5}{\langle N \rangle^4} + \frac{\mu_2\mu_5^2}{\langle N \rangle^4}\right) / n,$$

$$\text{Var}\left(\frac{C_6}{C_2}\right) = \left(-\frac{30\mu_{10}}{\mu_2} + \frac{\mu_{12}}{\mu_2^2} - 3600\mu_2^4 + 5400\mu_2^2\mu_4 + 30000\mu_2\mu_3^2 - 1800\mu_2\mu_6 - 8160\mu_3\mu_5 - 225\mu_4^2 \right. \\ \left. + 345\mu_8 - \frac{3900\mu_3^2\mu_4}{\mu_2} + \frac{840\mu_3\mu_7}{\mu_2} - \frac{120\mu_4\mu_6}{\mu_2} + \frac{216\mu_5^2}{\mu_2} + \frac{2300\mu_3^4}{\mu_2^2} - \frac{140\mu_3^2\mu_6}{\mu_2^2} + \frac{240\mu_3\mu_4\mu_5}{\mu_2^2} \right. \\ \left. - \frac{40\mu_3\mu_9}{\mu_2^2} - \frac{12\mu_5\mu_7}{\mu_2^2} + \frac{30\mu_6^2}{\mu_2^2} - \frac{520\mu_3^3\mu_5}{\mu_2^3} + \frac{20\mu_3^2\mu_8}{\mu_2^3} + \frac{52\mu_3\mu_5\mu_6}{\mu_2^3} - \frac{2\mu_6\mu_8}{\mu_2^3} + \frac{100\mu_3^4\mu_4}{\mu_2^4} \right. \\ \left. - \frac{20\mu_3^2\mu_4\mu_6}{\mu_2^4} + \frac{\mu_4\mu_6^2}{\mu_2^4}\right) / n,$$

$$\text{Var}\left(\frac{C_7}{C_1}\right) = \left(\frac{861\mu_{10}\mu_2^2}{\langle N \rangle^2} - \frac{70\mu_{10}\mu_4}{\langle N \rangle^2} - \frac{70\mu_{11}\mu_3}{\langle N \rangle^2} - \frac{42\mu_{12}\mu_2}{\langle N \rangle^2} + \frac{\mu_{14}}{\langle N \rangle^2} + \frac{396900\mu_2^7}{\langle N \rangle^2} - \frac{529200\mu_2^5\mu_4}{\langle N \rangle^2} \right.$$

$$\begin{aligned}
 & - \frac{1102500\mu_2^4\mu_3^2}{\langle N \rangle^2} + \frac{79380\mu_2^4\mu_6}{\langle N \rangle^2} + \frac{299880\mu_2^3\mu_3\mu_5}{\langle N \rangle^2} + \frac{176400\mu_2^3\mu_4^2}{\langle N \rangle^2} - \frac{10080\mu_2^3\mu_8}{\langle N \rangle^2} \\
 & + \frac{558600\mu_2^2\mu_3^2\mu_4}{\langle N \rangle^2} - \frac{33600\mu_2^2\mu_3\mu_7}{\langle N \rangle^2} - \frac{29400\mu_2^2\mu_4\mu_6}{\langle N \rangle^2} - \frac{10584\mu_2^2\mu_5^2}{\langle N \rangle^2} + \frac{137200\mu_2\mu_4^3}{\langle N \rangle^2} \\
 & - \frac{43120\mu_2\mu_3^2\mu_6}{\langle N \rangle^2} - \frac{76440\mu_2\mu_3\mu_4\mu_5}{\langle N \rangle^2} + \frac{2310\mu_2\mu_3\mu_9}{\langle N \rangle^2} - \frac{14700\mu_2\mu_4^3}{\langle N \rangle^2} + \frac{1890\mu_2\mu_4\mu_8}{\langle N \rangle^2} \\
 & + \frac{966\mu_2\mu_5\mu_7}{\langle N \rangle^2} + \frac{343\mu_2\mu_6^2}{\langle N \rangle^2} - \frac{15680\mu_3^3\mu_5}{\langle N \rangle^2} - \frac{14700\mu_3^2\mu_4^2}{\langle N \rangle^2} + \frac{1505\mu_3^2\mu_8}{\langle N \rangle^2} + \frac{2590\mu_3\mu_4\mu_7}{\langle N \rangle^2} \\
 & + \frac{2254\mu_3\mu_5\mu_6}{\langle N \rangle^2} + \frac{1715\mu_4^2\mu_6}{\langle N \rangle^2} + \frac{1911\mu_4\mu_5^2}{\langle N \rangle^2} - \frac{42\mu_5\mu_9}{\langle N \rangle^2} - \frac{14\mu_6\mu_8}{\langle N \rangle^2} - \frac{\mu_7^2}{\langle N \rangle^2} + \frac{264600\mu_2^6\mu_3}{\langle N \rangle^3} \\
 & - \frac{26460\mu_2^5\mu_5}{\langle N \rangle^3} - \frac{220500\mu_2^4\mu_3\mu_4}{\langle N \rangle^3} + \frac{1260\mu_2^4\mu_7}{\langle N \rangle^3} - \frac{235200\mu_2^3\mu_3^3}{\langle N \rangle^3} + \frac{11760\mu_2^3\mu_3\mu_6}{\langle N \rangle^3} \\
 & + \frac{17640\mu_2^3\mu_4\mu_5}{\langle N \rangle^3} + \frac{47040\mu_2^2\mu_3^2\mu_5}{\langle N \rangle^3} + \frac{44100\mu_2^2\mu_3\mu_4^2}{\langle N \rangle^3} - \frac{420\mu_2^2\mu_3\mu_8}{\langle N \rangle^3} - \frac{840\mu_2^2\mu_4\mu_7}{\langle N \rangle^3} \\
 & - \frac{1176\mu_2^2\mu_5\mu_6}{\langle N \rangle^3} + \frac{39200\mu_2\mu_3^3\mu_4}{\langle N \rangle^3} - \frac{1120\mu_2\mu_3^2\mu_7}{\langle N \rangle^3} - \frac{1960\mu_2\mu_3\mu_4\mu_6}{\langle N \rangle^3} - \frac{2352\mu_2\mu_3\mu_5^2}{\langle N \rangle^3} \\
 & - \frac{1470\mu_2\mu_4^2\mu_5}{\langle N \rangle^3} + \frac{42\mu_2\mu_5\mu_8}{\langle N \rangle^3} + \frac{56\mu_2\mu_6\mu_7}{\langle N \rangle^3} - \frac{3920\mu_3^2\mu_4\mu_5}{\langle N \rangle^3} - \frac{2450\mu_3\mu_4^3}{\langle N \rangle^3} + \frac{70\mu_3\mu_4\mu_8}{\langle N \rangle^3} \\
 & + \frac{112\mu_3\mu_5\mu_7}{\langle N \rangle^3} + \frac{70\mu_4^2\mu_7}{\langle N \rangle^3} - \frac{2\mu_7\mu_8}{\langle N \rangle^3} + \frac{44100\mu_2^5\mu_3^2}{\langle N \rangle^4} - \frac{8820\mu_2^4\mu_3\mu_5}{\langle N \rangle^4} - \frac{14700\mu_2^3\mu_3^2\mu_4}{\langle N \rangle^4} \\
 & + \frac{420\mu_2^3\mu_3\mu_7}{\langle N \rangle^4} + \frac{441\mu_2^3\mu_5^2}{\langle N \rangle^4} + \frac{1470\mu_2^2\mu_3\mu_4\mu_5}{\langle N \rangle^4} \\
 & - \frac{42\mu_2^2\mu_5\mu_7}{\langle N \rangle^4} + \frac{1225\mu_2\mu_3^2\mu_4^2}{\langle N \rangle^4} - \frac{70\mu_2\mu_3\mu_4\mu_7}{\langle N \rangle^4} + \frac{\mu_2\mu_7^2}{\langle N \rangle^4} \Big) / n,
 \end{aligned}$$

$$\begin{aligned}
 \text{Var}\left(\frac{C_8}{C_2}\right) = & \left(-27300\mu_{10}\mu_2 + \frac{4760\mu_{10}\mu_4}{\mu_2} + \frac{3136\mu_{10}\mu_3^2}{\mu_2^2} + \frac{112\mu_{10}\mu_3\mu_5}{\mu_2^3} + \frac{70\mu_{10}\mu_4^2}{\mu_2^3} - \frac{2\mu_{10}\mu_8}{\mu_2^3} \right. \\
 & + \frac{5376\mu_{11}\mu_3}{\mu_2} - \frac{112\mu_{11}\mu_5}{\mu_2^2} + 1624\mu_{12} - \frac{140\mu_{12}\mu_4}{\mu_2^2} - \frac{112\mu_{13}\mu_3}{\mu_2^2} - \frac{56\mu_{14}}{\mu_2} + \frac{\mu_{16}}{\mu_2^2} \\
 & - 3572100\mu_2^6 + 6747300\mu_2^4\mu_4 + 48686400\mu_2^3\mu_3^2 - 1693440\mu_2^3\mu_6 - 13335840\mu_2^2\mu_3\mu_5 \\
 & - 2425500\mu_2^2\mu_4^2 + 282240\mu_2^2\mu_8 - 25166400\mu_2\mu_3^2\mu_4 + 1545600\mu_2\mu_3\mu_7 + 664440\mu_2\mu_4\mu_6 \\
 & + 606816\mu_2\mu_5^2 - 1254400\mu_3^4 + 1881600\mu_3^2\mu_6 + 3974880\mu_3\mu_4\mu_5 - 119840\mu_3\mu_9 + 102900\mu_4^3 \\
 & - 78540\mu_4\mu_8 - 77952\mu_5\mu_7 - 784\mu_6^2 - \frac{439040\mu_3^3\mu_5}{\mu_2} + \frac{1764000\mu_3^2\mu_4^2}{\mu_2} - \frac{115360\mu_3^2\mu_8}{\mu_2} \\
 & - \frac{268800\mu_3\mu_4\mu_7}{\mu_2} - \frac{119168\mu_3\mu_5\mu_6}{\mu_2} - \frac{31360\mu_4^2\mu_6}{\mu_2} - \frac{131712\mu_4\mu_5^2}{\mu_2} + \frac{3808\mu_5\mu_9}{\mu_2} \\
 & - \frac{840\mu_6\mu_8}{\mu_2} + \frac{512\mu_7^2}{\mu_2} - \frac{62720\mu_3^2\mu_4\mu_6}{\mu_2^2} + \frac{159936\mu_3^2\mu_5^2}{\mu_2^2} + \frac{3920\mu_3\mu_4^2\mu_5}{\mu_2^2} + \frac{8960\mu_3\mu_4\mu_9}{\mu_2^2} \\
 & + \frac{224\mu_3\mu_5\mu_8}{\mu_2^2} + \frac{896\mu_3\mu_6\mu_7}{\mu_2^2} + \frac{28175\mu_4^4}{\mu_2^2} + \frac{2100\mu_4^2\mu_8}{\mu_2^2} + \frac{9856\mu_4\mu_5\mu_7}{\mu_2^2} + \frac{3136\mu_5^2\mu_6}{\mu_2^2} \\
 & - \frac{16\mu_7\mu_9}{\mu_2^2} + \frac{56\mu_8^2}{\mu_2^2} + \frac{62720\mu_3^3\mu_4\mu_5}{\mu_2^3} + \frac{39200\mu_3^2\mu_4^3}{\mu_2^3} - \frac{1120\mu_3^2\mu_4\mu_8}{\mu_2^3} - \frac{7168\mu_3^2\mu_5\mu_7}{\mu_2^3} \\
 & \left. - \frac{4480\mu_3\mu_4^2\mu_7}{\mu_2^3} - \frac{7840\mu_3\mu_4\mu_5\mu_6}{\mu_2^3} - \frac{6272\mu_3\mu_5^3}{\mu_2^3} + \frac{128\mu_3\mu_7\mu_8}{\mu_2^3} - \frac{4900\mu_4^3\mu_6}{\mu_2^3} - \frac{3920\mu_4^2\mu_5^2}{\mu_2^3} \right)
 \end{aligned}$$

$$\begin{aligned}
& + \frac{140\mu_4\mu_6\mu_8}{\mu_2^3} + \frac{112\mu_5^2\mu_8}{\mu_2^3} + \frac{3136\mu_3^2\mu_4\mu_5^2}{\mu_2^4} + \frac{3920\mu_3\mu_4^3\mu_5}{\mu_2^4} \\
& - \frac{112\mu_3\mu_4\mu_5\mu_8}{\mu_2^4} + \frac{1225\mu_4^5}{\mu_2^4} - \frac{70\mu_4^3\mu_8}{\mu_2^4} + \frac{\mu_4\mu_8^2}{\mu_2^4} \Big) / n.
\end{aligned}$$

-
- [1] M. M. Aggarwal *et al.* (STAR Collaboration), [arXiv:1007.2613](https://arxiv.org/abs/1007.2613).
- [2] BES-II White Paper (STAR Note), <https://drupal.star.bnl.gov/STAR/starnotes/public/sn0598>.
- [3] Y. Aoki, G. Endrodi, Z. Fodor, S. D. Katz, and K. K. Szabo, *Nature (London)* **443**, 675 (2006).
- [4] I. Arsene *et al.* (BRAHMS Collaboration), *Nucl. Phys. A* **757**, 1 (2005).
- [5] B. Back *et al.* (PHOBOS Collaboration), *Nucl. Phys. A* **757**, 28 (2005).
- [6] K. Adcox *et al.* (PHENIX Collaboration), *Nucl. Phys. A* **757**, 184 (2005).
- [7] J. Adams *et al.* (STAR Collaboration), *Nucl. Phys. A* **757**, 102 (2005).
- [8] L. Adamczyk *et al.* (STAR Collaboration), *Phys. Rev. C* **96**, 044904 (2017).
- [9] S. Borsanyi, Z. Fodor, C. Hoelbling, S. D. Katz, S. Krieg, C. Ratti, and K. K. Szabo (Wuppertal-Budapest Collaboration), *J. High Energy Phys.* **09** (2010) 073.
- [10] A. Bazavov *et al.* (HotQCD Collaboration), *Phys. Lett. B* **795**, 15 (2019).
- [11] L. Adamczyk *et al.* (STAR Collaboration), *Phys. Rev. Lett.* **110**, 142301 (2013).
- [12] L. Adamczyk *et al.* (STAR Collaboration), *Phys. Rev. Lett.* **112**, 162301 (2014).
- [13] L. Adamczyk *et al.* (STAR Collaboration), *Phys. Rev. Lett.* **121**, 032301 (2018).
- [14] L. Adamczyk *et al.* (STAR Collaboration), *Phys. Rev. Lett.* **113**, 052302 (2014).
- [15] C. S. Fischer, J. Luecker, and C. A. Welzbacher, *Phys. Rev. D* **90**, 034022 (2014).
- [16] C. Shi, Y.-L. Wang, Y. Jiang, Z.-F. Cui, and H.-S. Zong, *J. High Energy Phys.* **07** (2014) 014.
- [17] F. Gao and Y.-x. Liu, *Phys. Rev. D* **94**, 076009 (2016).
- [18] C. S. Fischer, *Prog. Part. Nucl. Phys.* **105**, 1 (2019).
- [19] F. Gao and J. M. Pawlowski, *Phys. Rev. D* **102**, 034027 (2020).
- [20] W.-J. Fu, J. M. Pawlowski, and F. Rennecke, *Phys. Rev. D* **101**, 054032 (2020).
- [21] M. Buballa, *Phys. Rep.* **407**, 205 (2005).
- [22] W.-J. Fu, Z. Zhang, and Y.-x. Liu, *Phys. Rev. D* **77**, 014006 (2008).
- [23] T. K. Herbst, J. M. Pawlowski, and B.-J. Schaefer, *Phys. Lett. B* **696**, 58 (2011).
- [24] Z. Li, K. Xu, X. Wang, and M. Huang, *Eur. Phys. J. C* **79**, 245 (2019).
- [25] K. Fukushima and T. Hatsuda, *Rep. Prog. Phys.* **74**, 014001 (2011).
- [26] K. Fukushima and C. Sasaki, *Prog. Part. Nucl. Phys.* **72**, 99 (2013).
- [27] M. A. Stephanov, K. Rajagopal, and E. V. Shuryak, *Phys. Rev. D* **60**, 114028 (1999).
- [28] M. A. Stephanov, *Prog. Theor. Phys. Suppl.* **153**, 139 (2004).
- [29] Z. Fodor and S. D. Katz, *J. High Energy Phys.* **04** (2004) 050.
- [30] M. A. Stephanov, PoS **LAT2006**, 024 (2006).
- [31] R. V. Gavai and S. Gupta, *Phys. Rev. D* **78**, 114503 (2008).
- [32] S. Gupta, PoS **CPOD2009**, 025 (2009).
- [33] S. Ejiri, *Phys. Rev. D* **78**, 074507 (2008).
- [34] E. S. Bowman and J. I. Kapusta, *Phys. Rev. C* **79**, 015202 (2009).
- [35] M. M. Aggarwal *et al.* (STAR Collaboration), *Phys. Rev. Lett.* **105**, 022302 (2010).
- [36] A. Bazavov *et al.*, *Phys. Rev. D* **95**, 054504 (2017).
- [37] B. I. Abelev *et al.* (STAR Collaboration), *Phys. Rev. C* **81**, 024911 (2010).
- [38] M. S. Abdallah *et al.* (STAR Collaboration), *Phys. Rev. C* **103**, 034908 (2021).
- [39] X. Luo and N. Xu, *Nucl. Sci. Tech.* **28**, 112 (2017).
- [40] A. Bzdak, S. Esumi, V. Koch, J. Liao, M. Stephanov, and N. Xu, *Phys. Rep.* **853**, 1 (2020).
- [41] M. Asakawa, U. W. Heinz, and B. Muller, *Phys. Rev. Lett.* **85**, 2072 (2000).
- [42] Y. Hatta and T. Ikeda, *Phys. Rev. D* **67**, 014028 (2003).
- [43] Y. Hatta and M. A. Stephanov, *Phys. Rev. Lett.* **91**, 102003 (2003); **91**, 129901(E) (2003).
- [44] S. Ejiri, F. Karsch, and K. Redlich, *Phys. Lett. B* **633**, 275 (2006).
- [45] V. Koch, A. Majumder, and J. Randrup, *Phys. Rev. Lett.* **95**, 182301 (2005).
- [46] M. A. Stephanov, *Phys. Rev. Lett.* **102**, 032301 (2009).
- [47] M. Asakawa, S. Ejiri, and M. Kitazawa, *Phys. Rev. Lett.* **103**, 262301 (2009).
- [48] C. Athanasiou, K. Rajagopal, and M. Stephanov, *Phys. Rev. D* **82**, 074008 (2010).
- [49] B. Friman, F. Karsch, K. Redlich, and V. Skokov, *Eur. Phys. J. C* **71**, 1694 (2011).
- [50] S. Gupta, X. Luo, B. Mohanty, H. G. Ritter, and N. Xu, *Science* **332**, 1525 (2011).
- [51] H.-T. Ding, F. Karsch, and S. Mukherjee, *Int. J. Mod. Phys. E* **24**, 1530007 (2015).
- [52] B. J. Schaefer and M. Wagner, *Phys. Rev. D* **85**, 034027 (2012).
- [53] J.-W. Chen, J. Deng, and L. Labun, *Phys. Rev. D* **92**, 054019 (2015).
- [54] Y. Lu, Y.-L. Du, Z.-F. Cui, and H.-S. Zong, *Eur. Phys. J. C* **75**, 495 (2015).
- [55] J.-W. Chen, J. Deng, H. Kohyama, and L. Labun, *Phys. Rev. D* **93**, 034037 (2016).
- [56] V. Vovchenko, D. V. Anchishkin, M. I. Gorenstein, and R. V. Poberezhnyuk, *Phys. Rev. C* **92**, 054901 (2015).

- [57] L. Jiang, P. Li, and H. Song, *Phys. Rev. C* **94**, 024918 (2016).
- [58] A. Mukherjee, J. Steinheimer, and S. Schramm, *Phys. Rev. C* **96**, 025205 (2017).
- [59] C. Herold, M. Nahrgang, Y. Yan, and C. Kobdaj, *Phys. Rev. C* **93**, 021902 (2016).
- [60] W. Fan, X. Luo, and H. Zong, *Chin. Phys. C* **43**, 033103 (2019).
- [61] H. Zhang, D. Hou, T. Kojo, and B. Qin, *Phys. Rev. D* **96**, 114029 (2017).
- [62] G.-y. Shao, Z.-d. Tang, X.-y. Gao, and W.-b. He, *Eur. Phys. J. C* **78**, 138 (2018).
- [63] P. Isserstedt, M. Buballa, C. S. Fischer, and P. J. Gunkel, *Phys. Rev. D* **100**, 074011 (2019).
- [64] D. Mroczek, A. R. Nava Acuna, J. Noronha-Hostler, P. Parotto, C. Ratti, and M. A. Stephanov, *Phys. Rev. C* **103**, 034901 (2021).
- [65] W.-j. Fu, X. Luo, J. M. Pawlowski, F. Rennecke, R. Wen, and S. Yin, [arXiv:2101.06035](https://arxiv.org/abs/2101.06035).
- [66] L. F. Palhares, E. S. Fraga, and T. Kodama, *J. Phys. G* **37**, 094031 (2010).
- [67] Z. Pan, Z.-F. Cui, C.-H. Chang, and H.-S. Zong, *Int. J. Mod. Phys. A* **32**, 1750067 (2017).
- [68] B. Berdnikov and K. Rajagopal, *Phys. Rev. D* **61**, 105017 (2000).
- [69] S. Mukherjee, R. Venugopalan, and Y. Yin, *Phys. Rev. Lett.* **117**, 222301 (2016).
- [70] M. Stephanov and Y. Yin, *Phys. Rev. D* **98**, 036006 (2018).
- [71] S. Wu, Z. Wu, and H. Song, *Phys. Rev. C* **99**, 064902 (2019).
- [72] K. Rajagopal, G. Ridgway, R. Weller, and Y. Yin, *Phys. Rev. D* **102**, 094025 (2020).
- [73] X. An, G. Başar, M. Stephanov, and H.-U. Yee, *Phys. Rev. C* **102**, 034901 (2020).
- [74] M. A. Stephanov, *Phys. Rev. D* **81**, 054012 (2010).
- [75] M. A. Stephanov, *Phys. Rev. Lett.* **107**, 052301 (2011).
- [76] M. Cheng *et al.*, *Phys. Rev. D* **79**, 074505 (2009).
- [77] B. Stokic, B. Friman, and K. Redlich, *Phys. Lett. B* **673**, 192 (2009).
- [78] R. V. Gavai and S. Gupta, *Phys. Lett. B* **696**, 459 (2011).
- [79] M. Kitazawa and M. Asakawa, *Phys. Rev. C* **86**, 024904 (2012); **86**, 069902(E) (2012).
- [80] A. Bzdak and V. Koch, *Phys. Rev. C* **86**, 044904 (2012).
- [81] K. H. Ackermann *et al.* (STAR Collaboration), *Nucl. Instrum. Methods A* **499**, 624 (2003).
- [82] M. Anderson *et al.*, *Nucl. Instrum. Methods A* **499**, 659 (2003).
- [83] L. Adamczyk *et al.* (STAR Collaboration), *Phys. Rev. Lett.* **112**, 032302 (2014).
- [84] J. Adam *et al.* (STAR Collaboration), *Phys. Rev. Lett.* **126**, 092301 (2021).
- [85] W. J. Llope (STAR Collaboration), *Nucl. Instrum. Methods A* **661**, S110 (2012).
- [86] C. Adler, A. Denisov, E. Garcia, M. J. Murray, H. Strobele, and S. N. White, *Nucl. Instrum. Methods A* **470**, 488 (2001).
- [87] W. J. Llope *et al.*, *Nucl. Instrum. Methods A* **522**, 252 (2004).
- [88] F. S. Bieser *et al.*, *Nucl. Instrum. Methods A* **499**, 766 (2003).
- [89] M. L. Miller, K. Reygers, S. J. Sanders, and P. Steinberg, *Annu. Rev. Nucl. Part. Sci.* **57**, 205 (2007).
- [90] H. Bichsel, *Nucl. Instrum. Methods A* **562**, 154 (2006).
- [91] X. Luo, J. Xu, B. Mohanty, and N. Xu, *J. Phys. G* **40**, 105104 (2013).
- [92] A. Chatterjee, Y. Zhang, J. Zeng, N. R. Sahoo, and X. Luo, *Phys. Rev. C* **101**, 034902 (2020).
- [93] M. Zhou and J. Jia, *Phys. Rev. C* **98**, 044903 (2018).
- [94] T. Sugiura, T. Nonaka, and S. Esumi, *Phys. Rev. C* **100**, 044904 (2019).
- [95] A. Chatterjee, Y. Zhang, H. Liu, R. Wang, S. He, and X. Luo, *Chin. Phys. C* **45**, 064003 (2021).
- [96] M. Gyulassy and X.-N. Wang, *Comput. Phys. Commun.* **83**, 307 (1994).
- [97] S. A. Bass *et al.*, *Prog. Part. Nucl. Phys.* **41**, 255 (1998).
- [98] B. Ling and M. A. Stephanov, *Phys. Rev. C* **93**, 034915 (2016).
- [99] A. Bzdak, V. Koch, and N. Strodthoff, *Phys. Rev. C* **95**, 054906 (2017).
- [100] M. Kitazawa and X. Luo, *Phys. Rev. C* **96**, 024910 (2017).
- [101] S. He and X. Luo, *Chin. Phys. C* **42**, 104001 (2018).
- [102] V. Skokov, B. Friman, and K. Redlich, *Phys. Rev. C* **88**, 034911 (2013).
- [103] P. Braun-Munzinger, A. Rustamov, and J. Stachel, *Nucl. Phys. A* **960**, 114 (2017).
- [104] X. Luo, *Phys. Rev. C* **91**, 034907 (2015).
- [105] T. Nonaka, M. Kitazawa, and S. Esumi, *Phys. Rev. C* **95**, 064912 (2017).
- [106] X. Luo and T. Nonaka, *Phys. Rev. C* **99**, 044917 (2019).
- [107] P. Garg, D. K. Mishra, P. K. Netrakanti, A. K. Mohanty, and B. Mohanty, *J. Phys. G* **40**, 055103 (2013).
- [108] S. Esumi, K. Nakagawa, and T. Nonaka, *Nucl. Instrum. Methods A* **987**, 164802 (2021).
- [109] V. Fine and P. Nevski, in Proceedings CHEP 2000 [Comput Phys Commun. 140, 143 (2000)].
- [110] A. Bzdak, R. Holzmann, and V. Koch, *Phys. Rev. C* **94**, 064907 (2016).
- [111] T. Nonaka, M. Kitazawa, and S. Esumi, *Nucl. Instrum. Methods A* **906**, 10 (2018).
- [112] L. Adamczyk *et al.* (STAR Collaboration), *Phys. Lett. B* **785**, 551 (2018).
- [113] X. Luo, *J. Phys. G* **39**, 025008 (2012).
- [114] A. Pandav, D. Mallick, and B. Mohanty, *Nucl. Phys. A* **991**, 121608 (2019).
- [115] B. Efron, *Ann. Stat.* **7**, 1 (1979).
- [116] B. Efron, *Computers and the Theory of Statistics: Thinking the Unthinkable* (Society for Industrial and Applied Mathematics, Philadelphia, 1979).
- [117] P. Garg, D. K. Mishra, P. K. Netrakanti, B. Mohanty, A. K. Mohanty, B. K. Singh, and N. Xu, *Phys. Lett. B* **726**, 691 (2013).
- [118] J. Xu, S. Yu, F. Liu, and X. Luo, *Phys. Rev. C* **94**, 024901 (2016).
- [119] S. He and X. Luo, *Phys. Lett. B* **774**, 623 (2017).
- [120] B. I. Abelev *et al.* (STAR Collaboration), *Phys. Rev. C* **79**, 034909 (2009).
- [121] A. Bazavov *et al.*, *Phys. Rev. Lett.* **109**, 192302 (2012).
- [122] S. Borsanyi, Z. Fodor, S. D. Katz, S. Krieg, C. Ratti, and K. K. Szabo, *Phys. Rev. Lett.* **111**, 062005 (2013).
- [123] S. Gupta, D. Mallick, D. K. Mishra, B. Mohanty, and N. Xu, [arXiv:2004.04681](https://arxiv.org/abs/2004.04681).
- [124] A. Bzdak and V. Koch, *Phys. Rev. C* **96**, 054905 (2017).
- [125] J. Brewer, S. Mukherjee, K. Rajagopal, and Y. Yin, *Phys. Rev. C* **98**, 061901 (2018).
- [126] M. Asakawa, M. Kitazawa, and B. Müller, *Phys. Rev. C* **101**, 034913 (2020).

- [127] Y. Ohnishi, M. Kitazawa, and M. Asakawa, *Phys. Rev. C* **94**, 044905 (2016).
- [128] M. Sakaida, M. Asakawa, H. Fujii, and M. Kitazawa, *Phys. Rev. C* **95**, 064905 (2017).
- [129] M. Nahrgang, M. Bluhm, T. Schaefer, and S. A. Bass, *Phys. Rev. D* **99**, 116015 (2019).
- [130] J. Li, H.-j. Xu, and H. Song, *Phys. Rev. C* **97**, 014902 (2018).
- [131] Y. Lin, L. Chen, and Z. Li, *Phys. Rev. C* **96**, 044906 (2017).
- [132] G. A. Almasi, B. Friman, and K. Redlich, *Phys. Rev. D* **96**, 014027 (2017).
- [133] Z. Yang, X. Luo, and B. Mohanty, *Phys. Rev. C* **95**, 014914 (2017).
- [134] C. Zhou, J. Xu, X. Luo, and F. Liu, *Phys. Rev. C* **96**, 014909 (2017).
- [135] A. Zhao, X. Luo, and H. Zong, *Eur. Phys. J. C* **77**, 207 (2017).
- [136] V. Vovchenko, L. Jiang, M. I. Gorenstein, and H. Stoecker, *Phys. Rev. C* **98**, 024910 (2018).
- [137] M. Albright, J. Kapusta, and C. Young, *Phys. Rev. C* **92**, 044904 (2015).
- [138] K. Fukushima, *Phys. Rev. C* **91**, 044910 (2015).
- [139] P. K. Netrakanti, X. F. Luo, D. K. Mishra, B. Mohanty, A. Mohanty, and N. Xu, *Nucl. Phys. A* **947**, 248 (2016).
- [140] K. Morita, B. Friman, and K. Redlich, *Phys. Lett. B* **741**, 178 (2015).
- [141] S. Samanta and B. Mohanty, [arXiv:1905.09311](https://arxiv.org/abs/1905.09311).
- [142] S. He, X. Luo, Y. Nara, S. Esumi, and N. Xu, *Phys. Lett. B* **762**, 296 (2016).
- [143] M. Nahrgang, M. Bluhm, P. Alba, R. Bellwied, and C. Ratti, *Eur. Phys. J. C* **75**, 573 (2015).
- [144] D. K. Mishra, P. Garg, P. K. Netrakanti, and A. K. Mohanty, *Phys. Rev. C* **94**, 014905 (2016).
- [145] M. Bluhm, M. Nahrgang, S. A. Bass, and T. Schaefer, *Eur. Phys. J. C* **77**, 210 (2017).
- [146] Y. Zhang, S. He, H. Liu, Z. Yang, and X. Luo, *Phys. Rev. C* **101**, 034909 (2020).
- [147] F. Karsch, K. Morita, and K. Redlich, *Phys. Rev. C* **93**, 034907 (2016).
- [148] A. Bzdak, V. Koch, and V. Skokov, *Phys. Rev. C* **87**, 014901 (2013).
- [149] P. Braun-Munzinger, A. Rustamov, and J. Stachel, [arXiv:1907.03032](https://arxiv.org/abs/1907.03032).
- [150] F. Karsch and K. Redlich, *Phys. Lett. B* **695**, 136 (2011).
- [151] M. Bleicher *et al.*, *J. Phys. G* **25**, 1859 (1999).
- [152] J. Mohs, S. Ryu, and H. Elfner, *J. Phys. G* **47**, 065101 (2020).
- [153] R. L. Wasserstein and N. A. Lazar, *Am. Stat.* **70**, 129 (2016).
- [154] J.-H. Fu, *Phys. Rev. C* **96**, 034905 (2017).
- [155] P. Braun-Munzinger, B. Friman, K. Redlich, A. Rustamov, and J. Stachel, *Nucl. Phys. A* **1008**, 122141 (2021).
- [156] J. Fu, *Phys. Lett. B* **722**, 144 (2013).
- [157] A. Bhattacharyya, S. Das, S. K. Ghosh, R. Ray, and S. Samanta, *Phys. Rev. C* **90**, 034909 (2014).
- [158] A. Bzdak, V. Koch, and V. Skokov, *Eur. Phys. J. C* **77**, 288 (2017).
- [159] T. Nonaka, T. Sugiura, S. Esumi, H. Masui, and X. Luo, *Phys. Rev. C* **94**, 034909 (2016).